University of Strathclyde Engineering

Molecular Dynamics Simulations of Chitosan Oligomer Interactions at Surfaces and Lipid Bilayers

Magdalena Hudek

Department of Chemical and Process Engineering

Thesis submitted to the University of Strathclyde for the degree of Doctor of Philosophy

2024

This thesis is the result of the author's original research. It has been composed by the author and has not been previously submitted for examination which has led to the award of a degree.

Signed:

Date:

Abstract

Chitin and chitosan (de-acetylated chitin) biopolymers, derived mainly from langoustine shell waste, are excellent candidates for novel antimicrobial applications. Despite the large body of literature concerning chitosan, there is a need for further characterisation of chitosan dynamics at aqueous interfaces to aid the design of novel composite materials.

In this thesis, fully atomistic molecular dynamics simulations have been developed to study chitin and chitosan oligomer interactions with α-chitin and silica surfaces using umbrella sampling. The free energy curves yield binding energies of -2.1 and -0.33 kcal mol^{-1} per monomer for chitin and uncharged chitosan oligomers on chitin, and -0.6 kcal mol^{-1} per monomer for a charged chitosan oligomer on silica at pH 5. This means that the adsorbed chitosan oligomers are mobile on both surfaces. It is found that chitin and chitosan binding to the chitin surface is driven by hydrogen bonding, where the strength for chitosan is reduced by its lack of the acetyl group. In contrast, charged chitosan binding to silica is dominated by electrostatics, with the loading capacity of 0.094 mg m^{-2} reflecting charge compensation. This can be controlled by the choice of ionic solution, which has technological implications. Lastly, the interaction of chitosan with a complex model gram negative bacterial membrane was studied to further understanding of chitosan's antimicrobial activity. It was found that chitosan only weakly interacts with the lipopolysaccharides that form the outermost layer of the *E. coli* cell envelope, while readily adsorbing to the inner membrane. This is a novel finding, as most of the current research focuses on chitosan interaction with the inner membrane, neglecting to explain chitosan diffusion through the outer membrane.

The findings presented in this thesis can be used to guide the experimental de-

sign of chitosan-coated silica nanoparticles and chitosan-chitin composite materials for applications such as drug delivery or additives for biopolymer food packaging.

Contents

List of Figures

List of Tables

Abbreviations

α-chNC α-chitin Nano-Crystal

AFM Atomic Force Microscopy

COM Centre of Mass

DA Degree of deacetylation

EM Energy Minimisation

FEC Free Energy Curve

FF Force Field

G-IM Gram Negative Inner Membrane

G-OM Gram Negative Outer Membrane

HPC High Performance Computer

LJ Lennard Jones

MD Molecular Dynamics

NAMD Nanoscale Molecular Dynamics

NP Nonoparticle

PBC Periodic Boundary Conditions

Abbreviations

PME Particle Mesh Ewald

SD Steepest Descent

SiNP Silica nanoparticle

SMD Steered Molecular Dynamics

US Umbrella Sampling

WHAM Weighted Histogram Analysis Method

Physical Constants

h Planck's constant

k_b Boltzman constant

Symbols

$\boldsymbol{r}$ atom position

ρ Density

E Energy

G Gibbs Free Energy

T Temperature

t time

V Volume/Potential Energy

M_w Molecular Weight

Publications

Parts of this thesis have been previously published in peer-reviewed journals. The following chapters are based on these publications:

- **Chapter 4:** Magdalena Hudek, Karina Kubiak-Ossowska, Karen Johnston, Valerie A. Ferro, and Paul A. Mulheran, Chitin and Chitosan Binding to the α-Chitin Crystal: A Molecular Dynamics Study, ACS Omega 2023 8 (3), 3470-3477, DOI: 10.1021/acsomega.2c07495
- **Chapter 5:** Magdalena Hudek, Karina Kubiak-Ossowska, Karen Johnston, Valerie A. Ferro, and Paul A. Mulheran, Molecular Dynamics Study of Chitosan Adsorption at a Silica Surface, The Journal of Physical Chemistry C, DOI: 10.1021/acs.jpcc.4c05821

Conference presentations

- **Contributed talk at Physical Aspects of Polymer Science, 2022 London**; *Chitin and Chitosan Binding to the α-Chitin Crystal: A Molecular Dynamics Study*
- **Contributed talk at Material Research Society Fall Meeting 2023, Boston**; *Design of novel chitosan nanoparticles for antimicrobial use*
- **Contributed talk at 85th PPM: Polymers for Sustainable Future, 2024 Prague**; *Design of novel chitosan nanoparticles for antimicrobial use*
- **Poster at Industrial Biotechnology and Inovation Centre Annual Conference 2022, Glasgow**; *Computational Studies of Chitin and Chitosan*

Acknowledgements

This thesis wouldn't have been possible without the support of others.

Firstly, I would like to thank my supervisors, Dr Paul Mulheran, Dr Valerie Ferro, and Dr Karen Johnston. Thank you for your continued support and guidance during my entire PhD journey and all its challenges.

I owe a massive debt of gratitude to my funder, BBSRC, who provided me with a very generous grant to support my research project. Thanks also go to IBioIC, who administered my PhD, and all the staff there. Your guidance was pivotal for my growth as a researcher and really broadened my horizons beyond the scope of my own research project. I would also like to acknowledge the Archie-West HPC team, especially Karina, without whose support and facilities my simulations wouldn't have happened.

To my fellow PhD students, Niki and Ben, thank you for all the support and memes. Ben, thank you for being my on-call microbiologist.

To my dear friends Amelia, Beni, and Dominik, thank you for being there for me. It truly means the world to me. I will always treasure all our Highlands adventures.

To my second family, the Passionist community, you have welcomed me and given me a second home in Glasgow, for which I am deeply grateful.

I am especially thankful to my family, whose unwavering support and encouragement have carried me through this journey. Your belief in me has been a constant source of strength.

Lastly, thank you to anyone and everyone not mentioned here who gave me encouragement and support throughout the past four years. I deeply appreciate every word of kindness received.

Chapter 0. Acknowledgements

Chapter 1

Introduction and Background

1.1 Introduction

Chitosan is a biodegradable and biocompatible polymer obtained from chitin. Chitin is the second most abundant polymer found in nature, after cellulose[3]. It is the building block of the exoskeletons of crustaceans and insects. Despite being a renewable and readily available biopolymer, the main drawback of chitin is its insolubility in aqueous solvents, thus making it difficult to process using green chemistry. On the other hand, chitosan, which is derived from chitin via deacetylation is soluble in weak aqueous acids.

Chitosan has many desirable properties such as antimicrobial activity[4], biodegradability[5] and biocompatibility[6], which has led to great interest in using chitosan for many applications ranging from biomedical[7] to food packaging[8]. Despite this great interest in chitosan evidenced by a large body of literature on chitosan published to date, there remains a need for fundamental characterisation of chitosan and its interaction at the interface with other materials to enable the rational design of novel chitosan composite materials. Rational design of new materials refers to the approach where the design process is informed by the knowledge of the fundamental material properties to predict new material properties before they are experimentally created, thus reducing the need for the trial and error-based approach. Chitosan composites can improve the mechanical and barrier properties of materials and impart functionality such as decreased cytotoxicity for targeted drug delivery or imparting antimicrobial

properties[9].

1.2 Thesis aims

This thesis aims to model the chitosan interaction with chitin nanocrystal and silica nanoparticle (SiNP) surfaces to aid the rational design of chitosan composite materials for antimicrobial applications using molecular dynamics (MD) simulations. To further study chitosan's antimicrobial properties, its interaction with different model bacterial membranes has also been investigated. The objectives are:

- To provide a comprehensive understanding of the current state of the literature regarding chitosan and its composites, with emphasis on the current gaps in the fundamental research.
- To provide the theoretical background on MD simulations and a detailed methodology.
- To study aqueous chitosan interfaces with an α-chitin nanocrystal (α-chNC) and a silica surface, including adsorption processes and free energies of adsorption, which can be used for the rational design of new chitosan composite materials.
- To investigate chitosan interactions with a realistic bacterial membrane model to study the mechanism of chitosan's antimicrobial activity, which is still an open question within the literature.

To address these objectives, this chapter will first address the history of chitosan research to frame the current state of the study within the historical context and explain the current challenges the field faces. Next, the physicochemical properties of chitin and chitosan will be described in detail. Lastly, a comprehensive overview of the available chitosan-based nanoparticles and materials will be given with particular emphasis on the chitosan composite materials and their advantages. This will reveal the need for a better fundamental understanding of chitosan's behaviour at the interfaces and the role this fundamental understanding has in the rational design of new materials.

The rational design of materials is especially important in today's age of transition to more sustainable practices. Computational simulations can reduce the number of experiments necessary for the design of new materials and they can be used to optimise the ratios and amounts of compounds used to prevent wastage.

1.3 Historical Background

Research into chitin and chitosan dates back more than 200 years, so it is important to briefly introduce the historical context to gain a wider perspective on the state of research today.

The first mention of chitin in crustaceans dates to 1799 when English chemist Charles Hatchett reported "material particularly resistant to usual chemical" in the cuticle. However, the discovery of chitin is attributed to Braconnot in 1811 who found chitin in funghi[10]. The discovery of chitosan, the derivative of chitin dates to 1859 and the work of Charles Rouget, the name chitosan however, was introduced by Felix Hoppe-Seyler in 1894[11].

During the initial period of chitin research (1894-1930) the main focus was on the occurrence of chitin in living organisms. During this time, the lack of systematic nomenclature for polysaccharides and lack of certainty of structure led to often contradictory results[12]. By the 1950s X-Ray analysis became more reliable for differentiating between different polysaccharide structures. Chitosan films and fibres were first patented in 1937. During this time, natural fibre industries were developing and the first uses of chitin and chitosan in textile[13], paper making[14], photography[15] and adhesive[16] industries were reported. Despite this progress in research, there was little use of chitin and chitosan until the 1970s when interest in these materials was renewed[17] based on the need to better manage seafood waste. During this time, regulations that restricted the disposal of untreated shellfish waste into the sea were introduced, which prompted manufacturers to consider producing chitin and chitosan. Chitosan was first industrially produced in Japan in 1971[18]. This enabled various products and patents to be developed and many scientific journals and books to be published.

1.4 Physiochemical properties

Chitosan is a copolymer of linear 1–4 linked β-deoxy-glucosamine and β-acetyl-deoxy-glucosamine monomers. The polymer consisting of mainly 1–4 linked acetyl-glucosamine monomers is called chitin. The degree of deacetylation (DA) is often used to describe the amount of beta-glucosamine monomers in chitosan. DA is defined as a ratio of beta-glucosamine monomers to the total number of monomers. In general, a copolymer with the DA <50 % can be classified as chitin, while a polymer with DA >50 % is classified as chitosan. From this, we can see that the term chitosan describes a wide range of possible polymers so some authors use the term chitosans instead of singular chitosan.

Figure 1.1 shows the chemical structure of chitin and chitosan monomers. The monomers are similar to cellulose with the only difference being the presence of acetyl-amino (chitin) or amino (chitosan) functional groups at the C2 atom. The chitin monomers have neutral charge, while the amino group of the chitosan monomers can be protonated. Thus depending on the pH of the solution each chitosan monomer can have either neutral or +1 charge.

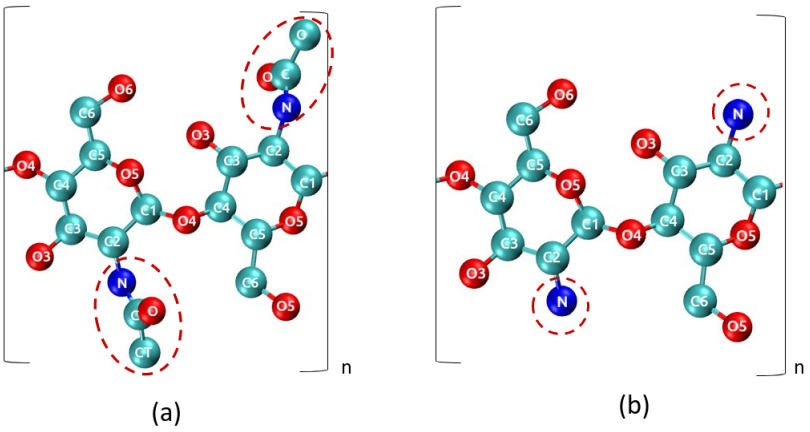

Figure 1.1: The molecular structure of chitin (a) and chitosan (b) polymers. The red circles indicate acetyl-amino (in a) and amino (b) functional groups. Hydrogens are omitted for clarity.

Chitin and chitosan chains have a helical structure along the fibre axis (along the

chain, which is characteristic of 1–4 linked polysaccharides. The rotation along the chain is characterised by dihedral angles ψ(O5-C1-O4-C4') and ϕ(C1-O4'-C4'-C3') dihedral angles, where ' denotes atom in the subsequent monomer. Chitin and anhydrous chitosan chains form a 2-fold helix with a $P2_1$ symmetry along the fibre axis.

Hydrated chitosan can adopt multiple helical structures: relaxed 2-fold, 4/1 and 5/3 helix. The most common is relaxed 2-fold helix that, despite the similar name to the 2-fold helix, looks very different. In a relaxed 2-fold helix the repeating unit is 4-monomers long, while in the 2-fold helix, the repeating unit is two.

Due to its neutral charge and strong intra- and inter-molecular hydrogen bonding, chitin is insoluble in aqueous solvents. On the other hand, chitosan, which has an intrinsic pKa around 6.5[19], becomes soluble in an aqueous acidic medium with pH <6.4 when the average DA is 50 % or higher. The most commonly used acid for the dissolution of chitosan is acetic acid, but hydrochloric and lactic acids are also used. The behaviour of chitosan in solution depends on the molecular weight (M_W) and distribution of acetyl groups along the chain. Block acetyl distribution can lead to aggregation, due to the hydrophobicity of the acetyl group.

Glucosamine monomers in solution will be in both protonated and de-protonated states. The pH can be determined by considering the extended Henderson-Hasselbalch equation:

$$pH = pK_{1/2} - n \log \frac{\beta_c}{1 - \beta_c} \tag{1.1}$$

where $pK_{1/2}$ is the apparent dissociation constant evaluated when 50% of the amino groups in the sample are ionised, n the empirically determined parameter related to the random movement of macromolecule and the free energy change. β_C is defined as $\beta_c = [NH_3^+]/([NH_3^+] + [NH_{2P1}])$. $[NH_3^+]$ and $[NH_{2P1}]$ are the concentrations of ionised and potentially ionisable amino groups respectively.

The ionic strength of the solution is known to affect the ability of chitosan and chitin to form nanoparticles and gels in solution. Chitosan gels obtained under a higher concentration of KCl have been found to possess weaker mechanical properties, i.e. reduced shear modulus, reduced persistence length and decreased solubility[20].

1.5 Chitin in nature

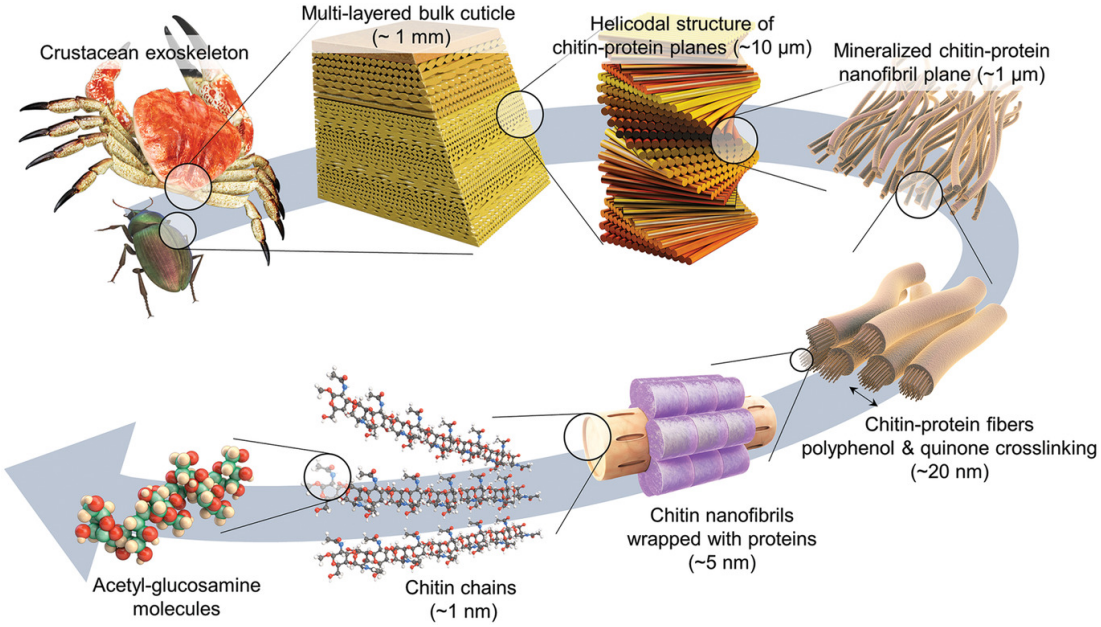

Figure 1.2: Multiscale structures of chitin in nature. Obtained from [1] under CC BY-NC 4.0 licence.

The main source of chitin are exoskeletons of various land and marine crustaceans, mainly crab and shrimp. These shells consist of a complex network of chitin and proteins with calcium carbonate deposits, which form the rigid shell. Chitin can also be found in the cell walls of certain fungi. Typically, chitin content in the cuticles of crustaceans is higher than that of land insects. In cuticles, chitin forms long fibres consisting of crystalline and amorphous regions. Proteins wrap around the fibres, and these protein-chitin fibres form larger fibre structures with minerals. These structures form fibre sheets which exhibit further internal twist, as illustrated in Fig. 1.2.

Chitin has three native crystalline polymorphs: α, β and γ[3], which are shown in Fig. 1.3. The difference between the three forms is in the chain direction. Neighbouring monomers are linked by the chiral glycosidic bond from Carbon C1 to Carbon C4, which gives a distinct direction to the chain. α-chitin chains are arranged antiparallel, while they are parallel in β-chitin. γ-chitin has similar properties to α-chitin and has two chains in parallel, and then one antiparallel chain alternating, as can be seen in Figure

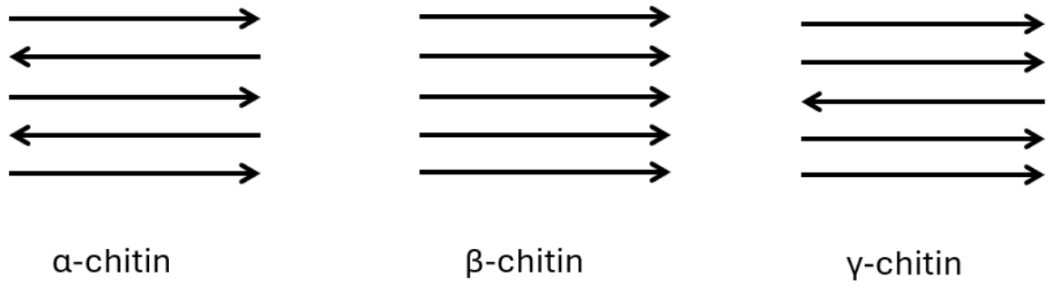

Figure 1.3: Chitin crystal exists in 3 polymorphs: α, β and γ, which are ilustrated here.

1.3. The most abundant and stable form of chitin is α chitin, with β- and γ- chitin convertible into α-chitin.

α-chitin is found in the cell walls of yeast and fungi, in crab tendons, and krill, lobster and shrimp shells. The α-chitin crystal is shown in Fig. 1.4. It is anisotropic and has $P2_12_12_1$ space group, with crystal lattice parameteres a=0.474 nm, b=1.88 nm, c(fibre axis)=1.032 nm[21]. The crystal structure is extended along the fibre axis (along the chain) and held together with hydrogen bonds in a structure that is layered.

Chitosan can also exist in crystalline α and β forms, analogous to chitin α and β polymorphs. However, β-chitosan is very rare, so only α polymorph is further described. The chitosan chains are arranged in the antiparallel fashion and can be found in hydrous and anhydrous forms [22, 23]. The orthorhombic unit cell of hydrated chitosan consists of 4 chains and 8 water molecules. The unit cell dimensions are a=8.95 Å, b=16.97 Å, and the fibre axis c=10.34 Å. In the anhydrous form, chitosan also has an orthorhombic unit cell with dimensions: a=8.28 Å, b=8.62 Å, and fibre axis c=10.43 Å. One unit cell consists of four glucosamine residues[24]. Chitosan forms different crystalline structures if ions are present[25].

Chitin and chitosan are often found in aqueous environments and they are most commonly cast from aqueous solutions for technological applications, thus knowledge of the properties of these polymers in aqueous environments is crucial for the development of new applications.

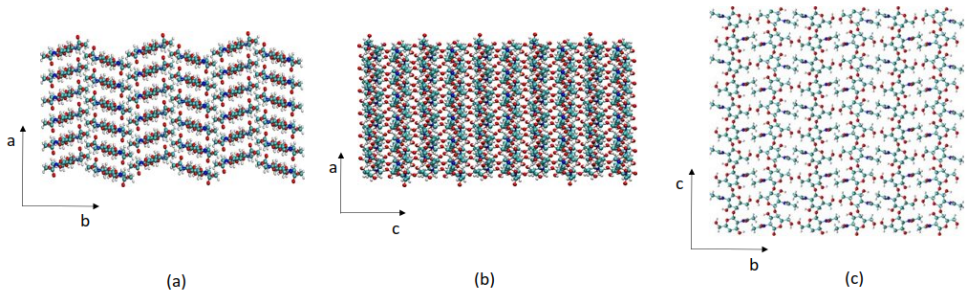

Figure 1.4: The crystal lattice of α-chitin crystal.

1.6 Chitin and chitosan production

Typically, chitin is produced from fishery waste consisting of crustacean shells. Chitin extraction requires the removal of protein (deproteinisation) and calcium carbonate (demineralisation). These steps usually also remove the lipids and pigments that are present in small amounts. Deproteination and demineralisation can be carried out either enzymatically or chemically. Another method is to use microbial fermentation which carries out both processes simultaneously.

There are a wide variety of approaches to chemical deproteination, however, most commonly NaOH is used. Demineralisation is commonly carried out using dilute hydrochloric acid. There are several drawbacks to using chemical extraction methods. This process changes the DA of the chitin, and reduces its molecular weight (M_w), which negatively influences the properties of the pure chitin. Furthermore, the byproducts are harmful and this process is expensive.

Biological methods of extraction preserve chitin properties better than chemical ones. The most common biological method is to use proteolytic enzymes for simultaneous deproteination and demineralisation. The enzymatic methods are less efficient than chemical ones, so additional NaOH treatment may be used to improve chitin purity. Rinaudo provides a detailed description of the described processes and lists the reported procedures[26].

Chitin can be converted to chitosan using chemical or enzymatic methods. Deacetylation can be carried out using either alkalis or acids, but the alkali method is more prevalent as the glycosidic bond is more susceptible to the acids. The process of deacety-

lation is usually carried out using NaOH. Depending on the exact procedure, it is possible to obtain chitosan with various DA levels. Different procedures will also result in varied distributions of acetyl groups along the chains.

The disadvantages of the chemical deacetylation process are high energy consumption and environmental pollution. Alternatively, enzymatic processes can be used. Chitin deacetylase is an enzyme reported in certain fungi and insect species. Chitin deacetylases vary depending on the species and produce various levels of DA and M_w. Thus, they can be used in creating well-defined chitosan, by using the optimal enzyme[27].

1.7 Antimicrobial properties

One of chitosan's most desirable properties is its antimicrobial activity. The exact mechanism behind the antimicrobial activity is still unclear[3]. Fig. 1.5 illustrates the proposed mechanisms of chitosan's antimicrobial activity.

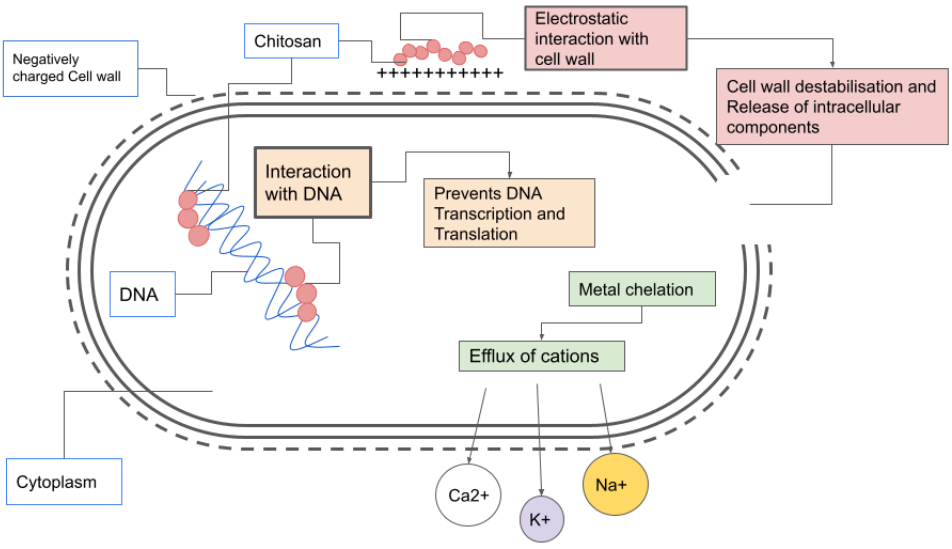

Figure 1.5: The proposed mechanisms of chitosan's antimicrobial action.

Chitosan oligomers may enter bacteria and disrupt DNA from functioning, as DNA is negatively charged, while chitosan is positively charged[28]. Larger chitosan chains

may bind to the negatively charged cell membrane, and cause leakage of intracellular components[29], or an alternative suggestion is that chitosan's chelation properties essentially starve the cells to death. Chelation is a process of molecular bonding to metal ions. In this case, the chitosan is proposed to bond to calcium, potassium and other essential micronutrients that bacteria require to function[30].

There are several factors that affect chitosan's antimicrobial activity. Different M_w chitosan chains exhibit different antimicrobial activity, but there are conflicting studies in this area. Some studies report high M_w chitosan displays better antimicrobial activity than low M_w chitosan[31], while another study found better antimicrobial activity for low M_w chitosans[32]. One study also reported antimicrobial activity for high M_w chitosan, but found low M_w chitosan promotes bacterial growth[33].

Positive charge density increases chitosan's antimicrobial activity, especially against *Staphylococcus aureus*. All the proposed mechanisms of chitosan's antimicrobial activity are based on the fact that it is a polycationic molecule, while the cell wall, DNA and other cell components are negatively charged, and thus will bind to chitosan. The charge density is mainly dependent on the DA and the pH of the solution. A higher level of DA means more amino groups available for protonation[34], while a lower pH level means more of the amino groups will be protonated. While it is expected that chitosan will have better antimicrobial properties at lower pH, there have been conflicting studies in this area as well. Sudarshan *et al.*[35] found that chitosan loses its antimicrobial properties at pH 7, while a more recent study showed chitosan microspheres can exhibit antimicrobial properties at neutral pH[36].

A limiting factor in chitosan's antimicrobial activity is its poor water solubility[37]. The antimicrobial compound usually needs water activity, as dry samples cannot easily bind to bacteria cells. Thus, improving chitosan's solubility is expected to lead to improvement in its antimicrobial activity and here there is potential for chitosan to be chemically modified to increase its solubility.

The ionic strength of a solution and ion species also has an effect on chitosan's antimicrobial activity. The presence of bicationic ions (Zn^{2+} and Ca^{2+})[36] in the solution decreases antibacterial activity. The proposed explanation for this is that

these bications interact competitively against chitosan when interacting with the cell wall.

Other relevant factors include the conformational properties of the chitosan's chain, and the form of chitosan in the application, mainly due to the available surface area. The higher the surface area available for binding to the bacterial cell wall, the higher the antimicrobial activity[38].

1.8 Chitosan applications

There are many proposed applications for chitosan, such as in wound dressings due to its hemostatic abilities, food packaging and antibacterial tooth pastes. However, there are not many applications on the market at the moment. The proposed applications of chitosan depend on the different desirable properties for the particular use. Rinaudo[39] provides a good overview of the potential applications of chitosan. In biomedical applications, these include surgical sutures, dental implants, artificial skin, bone scaffolding, corneal contact lenses, slow drug release materials, and adjuvants for vaccines. Desirable characteristics of chitosan associated with these are that they are biocompatible, biodegradable, renewable, film-forming, non-toxic, antimicrobial, antiviral and antifungal. In agriculture, potential applications include controlled time release of fertilisers, seed coating and defensive mechanism for plants. In water treatment, chitosan is proposed to be used for the removal of metal ions, removal of odours and as a flocculent to clarify water.

In food science, chitosan can be used as a dietary fibre, as it is not digestible by humans, and is a lipid binder. Chitosan has even been proposed as a weight loss supplement. A review from 2018 concluded that the use of chitosan tablets as a dietary supplement for up to 52 weeks led to mild body weight loss (on average -1.01 kg)[40], which makes it a fairly inefficient weight loss supplement.

There are various potential uses for chitosan in dentistry[41]. These vary in range from chitosan-based toothpastes and mouthwashes to drug delivery for the treatment of infections and periodontitis. Hemostatic wound dressings are designed to actively stop wounds from bleeding by accelerating the clotting process. They are mainly used

by the military and emergency responders.

Another proposed application for chitosan use is in food packaging. Ideal food packaging should be biodegradable, made from renewable sources and possess key structural, chemical and functional properties. The chemical and structural requirements for the material are that it is a barrier for small molecules, in particular oxygen, and that it has good water transfer control.

Chitosan films have low oxygen permeability when dry, but under humid conditions, they absorb water and become more oxygen permeable[42]. The mechanism of oxygen transfer was studied at low and high humidity by McDonell *et al.*[43] using MD simulations. To overcome such difficulties, chitosan can be used as a part of a composite material. The advantage of using composite material is that it preserves chitosan's functionality (bio-compatibility and antimicrobial action) while having enhanced mechanical properties. Chitosan-coated nanoparticles have many potential applications, including targeted drug delivery or providing antimicrobial properties to the bulk material where they are used as additives. Additional antimicrobial agents can be added, which usually act synergistically with chitosan.

In this thesis, the focus will be on two chitosan composites: a chitosan-chitin nanocrystal composite and chitosan coated silica nanoparticles, which will be further discussed in the following two sections.

1.9 Chitin nanocrystals

Chitin nanoparticles, also known as chitin nanowhiskers or chitin nanocrystals (chNCs) have a highly anisotropic nanorod shape. Unlike many other nanoparticles, chNCs are produced in a top-down fashion, meaning they are obtained by cleaving amorphous regions of chitin nanofibers. Consequently, this leads to a wide range of particle size. The width of the chNC can be in the range of 2-20 nm, while the length varies more significantly from 250-500 nm. The particle size depends on the source of chitin and the method of preparation. The most common crystalline polymorph is α-chitin. Yurtsever *et al.*[2] studied chNC using atomic force microscopy (AFM) and MD simulations to study the chNC at the water interface. They focused on the characterisation of the 3D

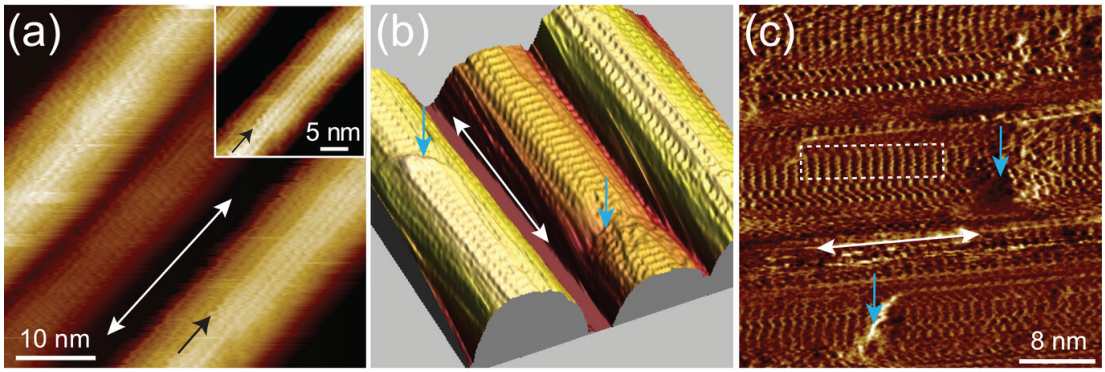

Figure 1.6: Atomic force microscope (AFM) images of α-chitin nanocrystal structure (a), 3D render if the same surface region and (c) corresponding dissipation data image. Adapted from Yurtsever *et al.* [2] (CC-BY-NC)

local hydration structure, but did not characterise the structure of the chNCs themselves. Figure 1.6 shows the obtained AFM images of chNCs. ChNCs are insoluble in water due to their strong intramolecular hydrogen bonding. MD calculations [44] shows the binding energy of 8 $kcal\ mol^{-1}$ per dimer. This is a slightly higher value than for cellulose crystals[45].

ChNCs have a variety of proposed applications in various fields and is most commonly reported as part of a composite system. In proposed biomedical applications, chNCs can be used as a part of a targeted drug delivery system[46, 47, 48], as a scaffold for tissue engineering[49, 50, 51] and in wound dressings[52, 53, 54, 55]. In water treatment, chNCs are used as adsorbents for heavy metals and dyes, often in combination with chitosan[56, 57] and as additives in filtration membranes[58, 59, 60]. In the food industry, chNCs are used as an additive to films for packaging applications, where they can improve the gas barrier and mechanical properties of the films[61], and as a spray coating[62]. Furthermore, chNCs can be used as stabilising agents in Pickering solutions[63, 64]. The use of Pickering solutions provides greater stability than traditional emulsions and reduces the need for chemical surfactants, which have many potential applications in cosmetic and pharmaceutical formulations. Despite a wide range of proposed applications, chNCs remain a commercially underutilised material, with a scope for further improvement. In particular chNCs in combination with chitosan can provide highly useful materials with improved solubility and antimicrobial

properties.

1.10 Silica nanoparticles (SiNP)

Silica nanoparticles (SiNP) are widely used due to their excellent properties such as high mechanical strength, ease of modification and large surface area. They are commonly reported as an excellent delivery mechanism for targeted drug delivery[65]. Medicine, such as the potent chemotherapy drug, doxycycline (dox), can be effectively loaded into mesoporous SiNP. This in turn decreases the often very harsh side effects of drugs such as dox. However, SiNPs can be cytotoxic[66]. Coating the nanoparticles with biopolymers such as chitosan has been found to decrease their cytotoxicity[67]. Furthermore, chitosan is pH-responsive, so it can be used as part of targeted drug delivery[68]. Cancers often change their microenvironments within the body, thus if a pH-responsive material such as chitosan is used, the drug can be released in the cancer region and prevent systemic side effects for the patient.

Chitosan-coated SiNPs can, similar to ChNCs, be used as additives for food packaging or in coatings to impart functionality to materials[69]. The added functionality includes UV protection, enhanced durability and antimicrobial action.

Despite a large number of publications on the synthesis of chitosan silica composite nanomaterials, there are very few publications which characterise the mechanism of adsorption and the strength of chitosan interaction with the silica surface.

1.11 Use of computational studies in material design

Computational simulations are powerful tools for novel material design. They offer several advantages over experimental methods. Simulations, such as those employed in this thesis, provide a molecular level of detail and enable the study of interactions at the atom-to-atom level. This level of detail is difficult to achieve using experimental techniques.

MD has been employed to study various properties of chitosan, such as dependence of chitosan flexibility on its DA and the ionic strength of solution[70, 71], the molecular

kinetics of chitosan crystal dissolution at various pH levels[72, 73], chitosan swelling in water[74], and the mechanical strength of chitosan using steered MD[75].

1.12 Summary and perspective

Chitin and chitosan are hugely underused biopolymers with a plethora of applications. Despite the numerous proposed applications, challenges remain in bringing chitin and chitosan products to market. Due to the variability of chitin feedstocks, it is difficult to standardise chitin and chitosan polymers; the composition and biochemical properties might vary from batch to batch. This leads to difficulty in developing commercial products.

Despite a large number of available publications, there has been relatively little literature written on the fundamental behaviour of chitosan at the aqueous interfaces with surfaces. Understanding the material interactions at the atomic scale can aid in rational material design. Computational simulations are particularly suited for use in this research due to the ability to study materials at the atomic scale. In simulations, the exact composition of the system and conditions are known, so there are no issues with impurities or varying material compositions as can be the case when carrying out experiments. That said, computational studies always need to be compared to available experimental data and are best used in synergy with experiments.

1.13 Thesis overview

The thesis si organised as follows. **Chapter 2** describes the theory and force fields used in MD simulations relevant to this work, including steered MD (SMD) and umbrella sampling. The description and rationale for the general methodology are given, laying the groundwork for the rest of the thesis.

Chapter 3 establishes the methodology and validates the force field to be used in subsequent chapters. In this chapter simple simulations of systems containing chitin and chitosan are conducted to ensure the model accuracy and reproducibility of the key physical properties.

In **Chapter 4**, the interaction of chitin and chitosan oligomers with α-chNCs are studied in an aqueous environment. The free energy of adsorption is calculated using US.

In **Chapter 5** the interaction of chitosan with silica surface in an aqueous enviroment is studied. The free energy of adsorption is calculated as well as the chitosan adsorption density, which is compared to available experimental literature.

The results presented in **Chapters 4** and **5** can be used to guide the rational design of novel chitosan coated nanoparticles for various uses described within this chapter.

In **Chapter 6** a model of *E. Coli* membrane with realistic lipid composition is constructed and its interaction with chitosan oligomers is studied to help elucidate mechanism of chitosan's antimicrobial action.

Chapter 7 provides the summary of the results, discusses the impacts of the research presented in this thesis and gives perspective for future research.

Chapter 2

Molecular Dynamics

Computational simulations are a powerful tool for bridging the gap between theory and experiments. In computational simulation, the initial state of the system is well-defined and the system evolution is governed by the underlying theory. Due to the ever-growing computational power of modern high-performance computers (HPCs), the complexity and the size of the systems which can be simulated is growing. While simulations should be used synergetically with experiments, they are cheaper, safer and offer greater parameter control than experiments.

Computational simulation methods vary depending on the scale of the system and the required level of detail and accuracy. All computational methods are based on numerical methods and over time, more complex algorithms have been developed. The most precise methods are based on quantum mechanical calculations, which have very high computational costs. Such systems are limited to around a thousand atoms in terms of size. Examples of such methods are density functional theory (DFT) and Car-Parinello dynamics. On the other side of the spectrum are techniques such as the finite element method (FEM) which simulates macroscopic objects, while completely ignoring the atomistic nature of matter.

Atomistic molecular dynamics (MD) enables us to study systems containing tens of thousands of atoms (up to several million in some cases), which are typically simulated from tens of nanoseconds to microsecond time scale. The simulated systems can contain complex structures such as crystals and polymers. MD enables us to study the evolution

of the systems, such as the adsorption of a polymer to a surface.

In practice, MD simulations are performed using software packages such as LAMMPS, Gromacs[76] or NAMD[77]. These codes are open-source, actively developed and maintained, and each code has been optimised for a particular use. NAMD and GROMACS are the most suited for biomolecular simulations and have been used to perform the work presented in this thesis. This chapter presents an overview of the MD theory and the algorithms used in this work.

Chapter aims:

- To provide the basic theoretical framework underpinning MD
- To provide a practical guide to the most common MD simulations workflows
- To discuss the limitations, and appropriate use of MD simulations

2.1 Atomic and molecular representation

MD simulations aim to simulate dynamics of matter at the atomic scale. Since MD is a classical method, the quantum-mechanical nature of atoms is ignored and the position of every atom is represented by a single vector $\boldsymbol{r}_i$ as a point in space:

$$\boldsymbol{r}_i = (x_i, y_i, z_i) \tag{2.1}$$

where i denotes the number of the atom in the system. This approach to MD is called all-atom, as every atom is represented as one point particle in space. Each particles is assigned its atom type and mass (m_i). The atoms are further described by application of system specific potential functions.

Note on nomenclature: In MD language, the word atom is used loosely, as one chemical atom species can have many MD atom types. Instead, the word element is used for the chemical species of the atom.

2.2 Potentials

The components of the potential functions in the MD simulations can be divided into three categories: force field (FF), restraints and applied potentials. The applied potentials are only used in enhanced sampling methods and are thus given in the context of each method.

2.2.1 Force Field

FF describes system-specific interactions in the system. The parametrisation of a force field is a task not to be underestimated. The parameters for smaller model molecule parameters are obtained from experimental data, such as electron diffraction or crystallographic x-ray data, or quantum mechanical calculations. The initial parameters are then iteratively optimised. Larger molecules often use parameters derived for smaller, chemically similar model compounds for which the parameters are known. This is then further optimised. Each FF has a specific protocol for optimisation, which ensures the parameters are self-consistent.

The choice of the FF is the crucial step in conducting MD simulations, as it contains all the parameters necessary for calculations of the potential forces in the system. Every FF has two components: the potential functions (set of equations) which generate the potentials, and the parameters used in the those potential functions. Parameters describe the properties of different atomic species and their interactions with other atoms. This includes a description of all chemical bonds and all interactions between non-bonded atoms.

The parameters are developed with specific potential functions in mind, and cannot be used with a different force field. Some of the things that need to be considered when choosing the force field are accuracy, performance and availability of different residues (parts of a large molecule).

In this work all the simulations were performed using CHARMM36 FF. The CHARMM FF[78] is an empirical class I (additive) FF consisting of a family of compatible FFs. These include protein, lipid, carbohydrate[79, 80, 81] and general (cgenff)[82] FFs. This

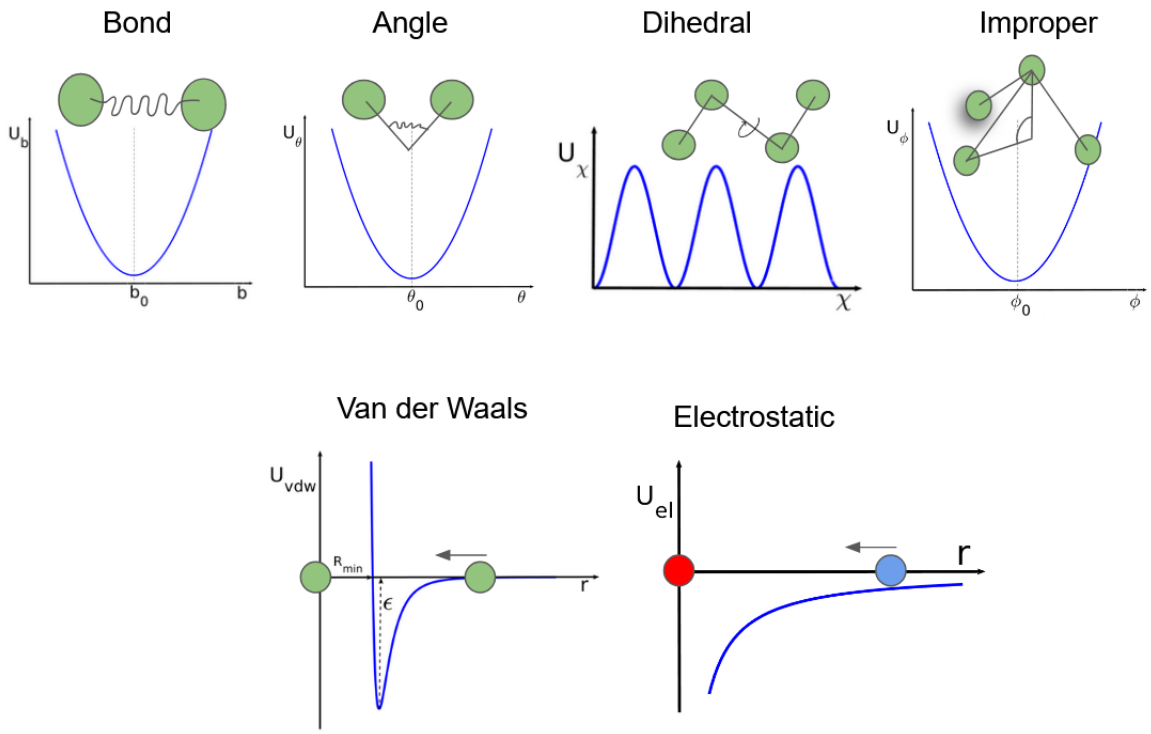

Figure 2.1: Illustration of the CHARMM additive force field with associated potentials.

FF can be used in both NAMD and Gromacs[83]. CHARMM36 FF has been validated for use with polysaccharides by comparison with experiments for properties such as crystal cell parameters, aqueous densities, aqueous NMR coupling constants and intramolecular geometries[79]. In addition to the CHARMM36 FF, the INTERFACE FF[84] has been used to model a fully mobile silica slab. This FF has been developed for MD simulations of inorganic surfaces and is consistent with CHARMM.

Note on nomenclature: The CHARMM FF files consist of parameters (par) and topology (top) files. Par files contain the previously described FF parameters, except the partial charges which are stated in the top files. Top files list the residues. Residues are small molecules, which can often be combined with patches which enable the construction of more complex molecules. For example, to construct chitin polymer, acetylglucosamine monomers are connected with the β glycosidic linkage patch.

The potential functions of the CHARMM additive FF are illustrated in Fig. 2.1 with the full potential formally given below:

$$
\begin{aligned}
U(\boldsymbol{r}) = & \sum_{bonds} K_b(b-b_0)^2 + \sum_{angles} K_\theta(\theta-\theta_0)^2 \\
& + \sum_{dihedrals} K_\chi(1+\cos(n\chi-\delta)) + \sum_{impropers} K_{imp}(\phi-\phi_0)^2 \\
& + \sum_{non-bonded} \epsilon_{ij}\left(\left(\frac{R_{min,ij}}{r_{ij}}\right)^{12} - 2\left(\frac{R_{min,ij}}{r_{ij}}\right)^{6}\right) + \frac{q_i q_j}{4\pi\epsilon_0 r_{ij}}
\end{aligned}
\tag{2.2}
$$

Bond, angles, dihedrals and improper terms describe interactions between bonded atoms. The terms K_b, K_θ, K_χ and K_{imp} are scaled[1] force constants for bond, angle, dihedral angle and improper dihedral angle potentials respectively. b, θ, χ and ϕ are the bond length, angle, dihedral angle and improper angle respectively, with 0 subscripts being the equilibrium value. Additionally, the dihedral potential is described by the multiplicity, n and the phase shift terms, δ.

The last two terms describe interactions between non-bonded atoms[2] using Van der Waals and electrostatic interactions. ϵ_0 is the dielectric constant in the vacuum. ϵ_{ij} is the depth of the Lennard-Jones (LJ) well between i and j atom pairs. Similarly, $R_{min,ij}$ and r_{ij} are the distance at the LJ energy minimum and the distance between i and j atom pairs respectively. q_i and q_j are the partial atomic charges of the atoms i and j. LJ parameters are determined by applying Lorentz [85]-Berthelot [86] rules which are given by:

$$R_{min,ij} = \frac{R_{min,i} + R_{min,j}}{2} \tag{2.3}$$

$$\epsilon_{ij} = \sqrt{\epsilon_i \epsilon_j} \tag{2.4}$$

Particular care needs to be taken when calculating non-bonded interactions. In principle, these potentials extend to infinity. In practice, they decay very closely to zero at a certain distance. Van der Waals interactions decay faster than electrostatics, so a cut-off scheme is used in this case. This means that the potential is evaluated up until a certain distance called switching distance, after which the potential is smoothed

[1] The usual $\frac{1}{2}$ constant is incorporated into the K values.

[2] excluding calculation for the nearest 4 atoms which are bonded, i.e. the non-bonded terms will not be evaluated for atoms where one of the bonded (bond, angle, dihedral) calculations exists

to zero value at the cut-off distance. The same can be done for electrostatic interactions, but due to their longer range, more accurate methods have been developed which will be discussed in section 2.4.

On the water models

Most biological processes occur in an aqueous environment, thus it is essential to include a model for the water molecules in MD simulations. There are several water models available, which offer different levels of detail. As is always the case in simulations, higher precision comes with a higher computational cost, thus balance between level of detail and speed is essential. CHARMM36 FF has been developed for use with the mTIP3P water model. This is a modified version of the original TIP3P (transferable intermolecular potential with 3 points) water model developed by Jorgensen in 1983[87]. The TIP3P model, as the name suggests, models water with three points in space, which correspond to two hydrogen atoms and one oxygen atom, with a fixed 104.5° H-O-H angle. The only difference between the original TIP3P and mTIP3P is the addition of Lennard-Jones interactions for the hydrogen atoms, which are set to zero in the original TIP3P model.

2.2.2 Restraint potentials

The restraint potentials are not part of the FF and thus the parameter values are not as important. These restraints are normally used to include knowledge from experimental data, or to avoid deviations for experimentally determined structures. It is common to apply position restraints to non-solvent atoms during the initial stages of simulation before the equilibrium is reached. This is done to prevent unphysical deformation of non-solvent species (e.g. protein, lipid bilayer) by the large solvent forces which can occur due to the initial solvent placement before equilibration. Another use for the position restraints is when simulating surfaces which should remain stationary. In Gromacs, the simple harmonic potential is used: $U(r_i) = 1/2k|r_i - R_i|^2$, where k is the strength of the potential, and R_i is the fixed reference position. In NAMD, it is common to completely freeze the atoms, i.e. not update the positions during

the simulation, instead of using the restraint potentials, which allow some motion to occur. The energy calculations are still done for the frozen atoms so that non-bonded interactions are preserved.

2.3 Periodic Boundary Conditions

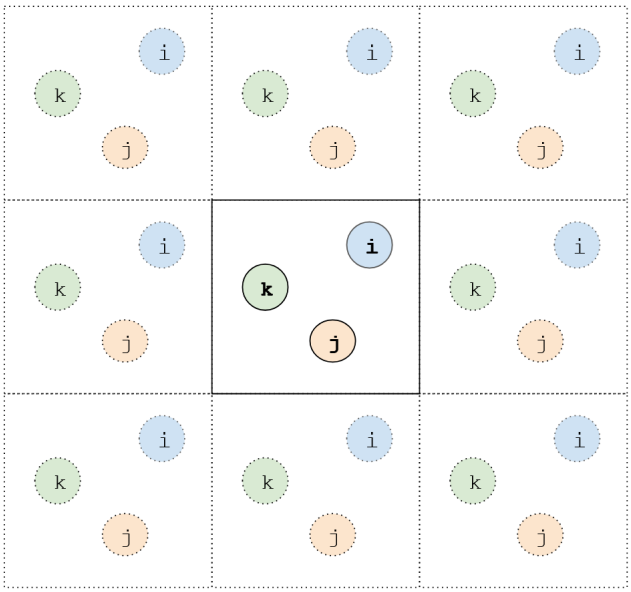

Figure 2.2: Illustration of the PBC in 2D.

When simulating molecules in an aqueous environment, we want to simulate bulk conditions to avoid finite size effects. This is achieved through imposing periodic boundary conditions (PBC), which means that the particle positions are translated by the size of the box, as shown in Fig. 2.2. In one dimension this is described by mapping $x + n_x L \rightarrow x$, where x is the position of the atom, L is the length of the box and n is an integer which determines which periodic box the particle occupies. For certain systems, it might be desirable to apply periodicity in only two dimensions, but most commonly PBC is used in all three dimensions. Furthermore, the use of PBC enables the use of more advanced and accurate electrostatic calculations described in the next section.

2.4 Electrostatic calculations

As previously stated, the electrostatic interactions decay slowly with distance so that particular care needs to be taken. In MD this is done using the Ewald summation. Ewald summation splits the potential calculation into two parts: short range and long range. Short range interactions involve those between charges within the primary simulation box, while the long-range calculations involve interactions between charges in the periodic image boxes. The short range term is summed directly, while the long-range interaction term is further expanded to include correction terms and is calculated using a Fourier transform. There are two correction terms: self-energy and surface energy. The self-energy is a trivial constant term, which subtracts the energy of the particle interacting with itself in the primary simulation box. The surface energy is neglected by assuming the tin-foil boundary condition[88]. This type of summation is conditionally convergent[3]. The Ewald summation is computationally very expensive ($O(N^{3/2})$), so the more efficient Smooth Particle Mesh Ewald (SPME) method is often used instead. This is a fast numerical method for computing the Ewald sum, with the calculation time proportional $O(N \log N)$. SPME makes an approximation by assigning the charges to the grid points of the mesh, but nevertheless is a more accurate method than the cut-off scheme as it accounts for all the interactions. It is also the most popular method for calculating electrostatics.

2.5 Energy minimisation

The initial atomic positions used for MD simulations can be obtained in various ways. Most commonly solute conformations are taken from crystallographic data or guessed based on stereo-chemistry. Thereafter, water and other solvent molecules are added semi-randomly into the simulation box. This means that the initial potential energy of the system will be high, which will lead to unphysical behaviour and the simulation blowing-up [4]. For this reason, before performing MD, the potential energy of the system

[3]The order of summation needs to be well defined

[4]Blowing-up is term used in the MD community to describe a simulation that crashes due to highly unphysical behaviour, such as particles having too large velocities. Such a system, when visualised,

is reduced using energy minimisation (EM).

EM is the procedure based on molecular mechanics, in which the system is driven into local energy minima. From a physical point of view, the resulting structure is equivalent to the classical state of the system at absolute zero temperature. There are several algorithms for EM that can be used, which will produce largely similar results. The standard EM method in NAMD is Conjugate Gradient, while GROMACS uses Steepest Descent.

2.5.1 Steepest Descent

Steepest Descent (SD)[89] is not the most efficient algorithm, but it is robust. The forces and the potential energy are calculated first, and then the new positions are calculated by:

$$\boldsymbol{r}_{n+1} = \boldsymbol{r}_n + \frac{\boldsymbol{F}_n}{max(|\boldsymbol{F}_n|)} h_n \tag{2.5}$$

where h_n is the maximum displacement and $\boldsymbol{F}_n$ is the force. $max(|\boldsymbol{F}_n|)$ is the maximum scalar force on any atom in the system. The forces and energy are again evaluated for the new positions. If the potential $V_{n+1} < V_n$, the new positions are accepted and $h_{n+1} = 1.2h_n$, if $V_{n+1} > V_n$, the new positions are rejected and $h_{n+1} = 0.2h_n$.

The algorithm is repeated until the absolute magnitude of the maximum force is less than the user-specified value or the algorithm reaches a user-specified maximum number of iterations.

2.5.2 Conjugate Gradient

Conjugate Gradient (CG) uses the same parameters and stop criteria as the SD algorithm. It is slower during the initial stages but becomes more efficient than SD as the energy minimum is approached. During each iteration step, the new direction of minimisation is orthogonal to the previous step, which accelerates convergence compared

might appear to be exploding.

to the SD method. Furthermore, the CG algorithm will place the system closer to the energy minima than the SD algorithm, but this is relevant only in highly specific cases. Further advantages of the CG method compared to SD are lower memory requirements as CG does not need to store the entire Hessian matrix, the convergence in less iterative steps and a more direct path to convergence, which avoid the possibility of oscillatory paths and partial undoing of progress. For most applications, the choice of the energy minimisation algorithm is not crucial, as the difference in energies given by different algorithms is small relative to the value of k_BT at 300 K.

2.6 Equations of motion and time integration

MD employs Newton-like equations of motion, which means classical equations of motion are solved (as opposed to quantum equations of motion[5]). Newton's equations of motion are given by:

$$\boldsymbol{F}_i(t) = m_i \frac{d^2\boldsymbol{r}_i}{dt^2} = -\nabla_r U(\boldsymbol{r}) \tag{2.6}$$

for a system of N particles, where m_i is the mass and $\boldsymbol{r_i}$ is the position, with the subscript denoting the i^{th} particle. $\boldsymbol{r}$ denotes complete position of the system in 3N dimensions (the positions of all N particles in the system). U is the total potential energy which depends on the position of all the particles in the system.

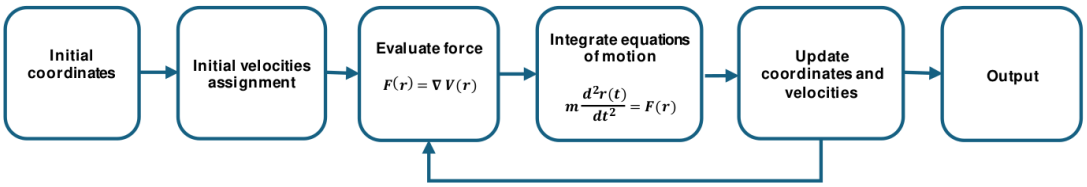

Figure 2.3: Simplified flowchart of the MD calculation protocol

Figure 2.3 shows a simplified flowchart of the MD calculation algorithm. The specifics of each step will be explained in the following sections.

To obtain system dynamics, Newton-like equations of motion need to be integrated

[5]quantum mechanical information about the system is included in the force field parameters

using a numerical integration algorithm. There are several numerical integration methods, however they all need to satisfy certain requirements:

- not violate laws of physics
- obey conservation of energy and momentum laws
- be time-reversible
- be fast and stable

The exact equations of motion that are used will depend on the FF type, the thermostat and the barostat used. The algorithms are iterative, with the initial velocities assigned based on the Boltzmann distribution at the desired temperature.

Most of the methods implemented (and recommended) in modern MD are based on the Leap-frog algorithms. The two variations of the algorithm are given below.

2.6.1 Leap-frog algorithm

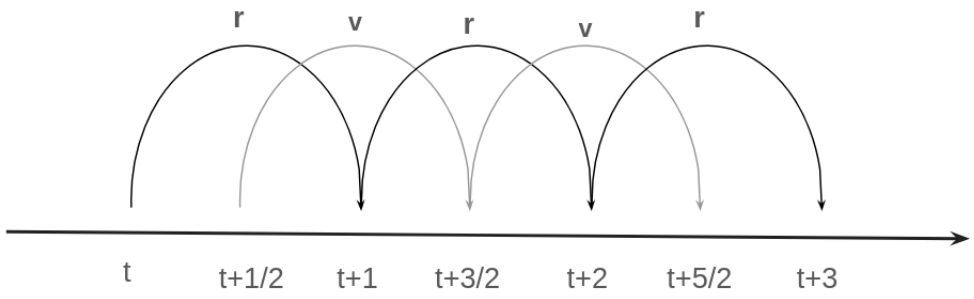

Figure 2.4: The illustration of the leap-frog algorithm, the velocity and position calculations are leaping over each other 'like frogs'.

The Leap-Frog[90] is one of the most common time integration algorithms used for MD simulations. It uses the positions $\boldsymbol{r}$ at time t and velocities $\boldsymbol{v}$ at time $t + \frac{1}{2}\Delta t$, as illustrated in Fig. 2.4. This algorithm is time reversible and is a default time integration method implemented in Gromacs with other algorithms available. The relevant equations of motion are:

$$\boldsymbol{v}\left(t+\frac{1}{2}\Delta t\right)=\boldsymbol{v}\left(t-\frac{1}{2}\Delta t\right)+\frac{\Delta t}{m}\boldsymbol{F}(t) \tag{2.7}$$

$$\boldsymbol{r}(t+\Delta t)=\boldsymbol{r}(t)+\Delta t\ \boldsymbol{v}\left(t+\frac{1}{2}\Delta t\right) \tag{2.8}$$

The symbols are used as previously described above. The error for this method is proportional to Δt^3.

2.6.2 Brunger-Brooks-Karplus method

NAMD uses the Brunger-Brooks-Karplus (BBK) numerical integration method[91], which is extension of the leapfrog velocity-Verlet time integration and it is method used for the integration of the Langevin equation (see section 2.7). The position recurrence relation is given by:

$$\mathbf{r}_{n+1}=\mathbf{r}_n+\frac{1-\gamma\ \Delta t/2}{1+\gamma\ \Delta t/2}(\mathbf{r}_n-\mathbf{r}_{n-1})+\frac{1}{1+\gamma\ \Delta t/2}\Delta t^2\left(M^{-1}\mathbf{F}(\mathbf{r}_n)+\sqrt{\frac{2\gamma k_bT}{\Delta M}}\mathbf{Z}_n\right) \tag{2.9}$$

where n it the current timestep, M is the mass, $\mathbf{F}$ is the force, $\mathbf{Z}_n$ is the set of random Gaussian variables of zero mean and variance one, and γ is the friction coefficient. Other symbols have the usual meanings. The steady-state distribution generated by this method has a local error at the order of Δt^2.

2.7 Temperature coupling

In an N-particle system, the kinetic energy, E_k is related to the absolute temperature, T:

$$E_k=\frac{1}{2}\sum_{i=1}^{N}m_iv_i^2=\frac{1}{2}N_{df}k_BT \tag{2.10}$$

where N_{df} is the number of degrees of freedom[6]. Therefore, if the energy of the

[6] $N_{df}=3N-N_{constraints}-N_{COM}$, In MD N_{COM}=3

system is constant, as is the case in microcanonical ensemble (NVE), we can passively measure the temperature of the system.

Sometimes unrealistic and guessed initial conditions of MD simulations can lead to high initial energies in the system in the NVE ensemble, which can lead to the unphysical behaviour of the system. In particular, the guessed solvent positions can lead to high energies. This is especially significant for biomolecule simulations, where high energies may lead to irreversible reactions, such as protein denaturation. Furthermore, in laboratory experiments, the temperature is controlled, so we want to control the temperature during the simulation to best replicate experimental conditions. To obtain canonical ensemble (NVT) in MD simulations, the system can be coupled to a virtual heat bath using a thermostat algorithm. Thermostats modify the calculation of velocities to achieve the desired temperature. There are several different types of thermostats which are implemented in both NAMD and Gromacs. The thermostats used in the work presented in this thesis are described here, using minimal equations to represent their principles, without full derivation. It should be noted that when applying a thermostat (and/or pressure) coupling, the total energy of the system will no longer be conserved.

2.7.1 Berendsen Thermostat

The Berendsen thermostat[92] is one of the simplest and oldest thermostats. It uses first-order kinetics to mimic weak coupling to a heat bath which has a target temperature T_0.

$$\frac{dT}{dt} = \frac{T_0 - T}{\tau} \tag{2.11}$$

Particle velocities are scaled by a factor so that the kinetic energy is modified by:

$$\Delta E_k = (\lambda - 1)^2 E_k \tag{2.12}$$

where λ is a time-dependent factor. In practice, there is a limitation on the range of λ, $0.8 <= \lambda <= 1.25$, in normal use the value is close to 1.0.[7]

[7]This is to avoid nonphysical phenomena such as "the flying ice cube" [93], where the internal translations and rotations of the system are suppressed, while the majority of the energy of the system

When using Berendsen thermostat coupling, the temperature decays exponentially with the time constant τ. The Berednsen thermostat does not produce a real canonical ensemble with the error scaling with 1/N. This thermostat is appropriate for the initial equilibration of the system only, as it is very robust and exponentially approaches the target temperature.

2.7.2 Nose-Hoover Thermostat

The Nose-Hoover thermostat[94] is very accurate and can be used for simulations of the equilibrated system. Unlike the Berendsen thermostat, which employs an imaginary heat bath, the Nose-Hoover thermostat couples to a virtual particle, which has its own momentum, p_ξ and equation of motion that represents the heath bath. When using this thermostat the equations of motion are such that:

$$\frac{d^2\boldsymbol{r}_i}{dt^2} = \frac{\boldsymbol{F}_i}{m_i} - \frac{p_\xi}{Q}\frac{d\boldsymbol{r}_i}{dt} \tag{2.13}$$

where the heat bath parameter ξ is described by:

$$\frac{dp_\xi}{dt} = (T - T_0)\ N_{df}\ k_B \tag{2.14}$$

where T_0 is the reference temperature and T is the instantaneous temperature, Q is the mass parameter of the coupling, which determines the strength of the coupling. The Nose-Hoover thermostat produces oscillatory relaxation in contrast to the exponential relaxation of the weak coupling (Berendsen). The relaxation time for the Nose-Hoover thermostat is therefore 4-5 times longer than for a weak-coupling thermostat (such as Berendsen). This thermostat correctly reproduces a canonical ensemble.

2.7.3 Langevin Thermostat

The Langevin thermostat[91] is a stochastic method that models a system coupled with a virtual implicit solvent. This implicit solvent replicates fluctuations due to friction forces between the solvent molecules and occasional high velocity collisions, which are

is expressed as the net COM motion of the system, violating the equipartition theorem.

modelled using a random force term. With this method, the Newtonian equations are replaced with the Langevin equation:

$$m\frac{d^2\boldsymbol{r}_i}{dt^2} = \boldsymbol{F}(\boldsymbol{r}) - \gamma\ \boldsymbol{v}_i(t) + \sqrt{\frac{2\gamma k_b T}{m}}\boldsymbol{R}(t) \tag{2.15}$$

where γ is the friction coefficient and $\boldsymbol{R}(t)$ is a univariate Gaussian random process. Eq. 2.15 is composed of three terms. The first term is the force dependent on the position of particles, the same as in standard Newton's equations of motion. The second term is the deterministic friction force term, while the third term is the stochastic fluctuating term. Langevin dynamics and Nose-Hoover are both widely reported in the literature for data-producing simulations.

2.8 Pressure coupling

As with temperature, the pressure in the simulation should be controlled as the typical bench experiment will be conducted at constant temperature and pressure. Here, instead of kinetic energy scaling, we have simulation box volume scaling. In both algorithms below, the pressure coupling is represented by a tensor, which enables the anisotropic pressure coupling with different compressibility along the x,y and z directions. This means that the box volume and shape can change, which is especially important when simulating systems with different compressibilities in different directions. For example, in the lipid bilayer simulations, the lipids are far more compressible than water (which is essentially incompressible). Thus, it is appropriate to set different compressibility along the directions of the bilayer plane compared to the orthogonal direction.

The pressure coupling in GROMACS simulations is performed by Parinello-Rahman coupling, while NAMD uses a modified version of the Nose-Hoover constant pressure method.

2.8.1 Parinello-Rahman pressure coupling

The Parinello-Rahman barostat is similar to the Nose-Hoover thermostat and in theory, should give the correct NPT ensemble.

$$\frac{d^2\boldsymbol{r}_i}{dt^2} = \frac{\boldsymbol{F}_i}{m_i} - \boldsymbol{W}\frac{d\boldsymbol{r}_i}{dt} \tag{2.16}$$

where the extra term, W is a mass parameter matrix that determines the strength of the coupling. Despite having appearance of mass this terms is fictitious and result of how the Parinello-Rahman barostat is defined [95].

2.8.2 Nose-Hoover Langevin pistol pressure control

NAMD uses the Nose-Hoover thermostat modified with a "Langevin piston method". Quigley and Probert[96] show that this method produces an NPT ensemble that correctly samples extended phase space. In this approach, an additional Hoover-style pressure term is added to the Langevin equation (eq.2.15). This represents coupling to a fictitious piston, introducing volume as a dynamic variable.

2.9 Constraint algorithms

Constraint algorithms in MD are used for several reasons, some physical and some practical. MD describes the motions of the atoms in a classical way (using Newtonian equations), which is reasonable for heavy atoms at room temperatures. On the other hand, hydrogen can exhibit purely quantum mechanical behaviour, such as proton quantum tunnelling during hydrogen bond proton transfer. Another example is high-frequency bond oscillations, much higher than $\frac{k_b T}{h}$, which cannot be properly described by a classic harmonic oscillator. For this reason, constraint algorithms are used to remove high-frequency oscillations. In practice, this allows for the algorithm to use a larger timestep, and reduces the cost of the simulations. Without restraint algorithms, the simulation timestep required is 0.25 fs, however with restraints the typical timestep is 2 fs.

The LINCS algorithm is an algorithm that resets bond length after the unconstrained update. This is a so-called soft restraint as it doesn't reset the bond length to a specific value, but instead calculates the projection of the length to correct for overstretching due to rotational lengthening.

The SETTLE algorithm is a special constraint algorithm for water. Water often contributes to more than 80 % of the molecules in the system, so the speed up for constrained water can be significant.

2.10 Enhanced Sampling Methods

When performing the MD simulation, the goal is to explore the whole of the space-phase landscape. According to the ergodic assumption, the system will explore all the available states if given enough time. However, the length of the simulation may not be sufficient to explore all the possible configurations, especially in the simulations with complex energy landscapes with multiple local energy minima present. Furthermore, some processes occur on the timescale that is not practical to achieve using standard MD, which can lead to poor sampling. Therefore, it is difficult, and often impossible, to calculate free energy from the standard MD simulations.

The free energy is defined through the canonical partition function, Q

$$Q(r) = \int e^{-\beta E(r)} d^N r \tag{2.17}$$

where $\beta = \frac{1}{k_b T}$. With commonly used FFs, E is independent of the momentum. The Helmholtz free energy A is defined as $A = -1/(\beta\ ln\ Q)$ in the NVT ensemble and the Gibbs free energy is defined as $G = -1/(\beta\ ln\ Q)$ in the NPT ensemble. In the condensed phase, there is a minimal difference between ΔA and ΔG. Usually, we are interested in the difference in the free energy between the two thermodynamic states, which can be defined by some order parameter. This order parameter is commonly known as the reaction coordinate and is denoted by ξ. Then Q can be written as a

function of the reaction coordinate:

$$Q(\xi) = \frac{\int \delta[\xi(r) - \xi] e^{-\beta E} d^N r}{\int e^{-\beta E} d^N r} \tag{2.18}$$

In simulations, 2.18 is impossible to evaluate, however for an ergodic system Q is equal to:

$$P(\xi) = \lim_{t \to \infty} \frac{1}{t} \int_0^t \rho[\xi(t')] dt' \tag{2.19}$$

where ρ is the probability distribution density for ξ. So in principle, it is possible to obtain free energy from MD simulation, however, simulations can only be run for a finite amount of time. Furthermore, the configuration space around the energy minima is typically sampled well, while the higher energy regions are poorly sampled. The configuration space separated by an energy barrier much higher than $k_B T$ might never be sampled.

Enhanced sampling methods are designed to overcome such potential energy barriers by providing an additional potential. This can be achieved by adding Gaussians, parabolic or other potentials to the system. Additional energy can also be achieved by heating the system, however this can be a bad idea in systems sensitive to high temperatures, for example lipid bilayer structure could be destroyed at a higher temperature.

2.10.1 Steered MD

Steered MD (SMD) is used to study non-spontaneous or rare events such as the stretching of DNA or the desorption of a molecule from a surface. This method can also be used as a computational analogue to atomic force microscopy (AFM) single-molecule experiments. The potential, V is added to that of the system, and is calculated using its position $\boldsymbol{R}$, which can be described as virtual atom. The initial position, $\boldsymbol{R_0}$ is placed on top of the atom or centre of mass (COM) of the group of atoms which are pulled. The potential is given by:

$$V(\boldsymbol{r}, t) = \frac{1}{2} k(vt - (\boldsymbol{R}(t) - \boldsymbol{R_0}) \cdot \boldsymbol{n})^2 \tag{2.20}$$

where v is the constant velocity with which the atom is pulled, $\boldsymbol{n}$ is the direction of pulling and k is the force constant. Other symbols have the usual meaning. The results can be used to calculate work done during the pulling by integrating the area under the force-displacement curve, and thus calculate the difference in free-energy between the two states. This can be done even for non-reversible pulling by using the Jarzynski equation[97] and averaging over many simulations.

2.10.2 Umbrella Sampling

Umbrella sampling (US) is based on a series of parallel MD simulations where the system is restrained with a harmonic potential so that it can only explore a small part of phase space[98]. Each simulation is called an umbrella or a window. The windows are evenly spaced across a reaction coordinate, which is referred to as a collective variable in the context of MD. Provided that the umbrellas overlap appropriately, this enables the system to explore all the states along the reaction coordinate.

The potential energy of the biased system is given by:

$$V^b(r) = V^u(r) + \omega_j(\xi) \tag{2.21}$$

where superscripts 'b' and 'u' indicate biased and unbiased quantities respectively. ω_j denotes the biasing potential were subscript j denotes the window number. The most commonly used potential is the simple harmonic given by: $\omega_j(\xi) = \frac{k_j}{2}(\xi - \xi_0)^2$. The strength of the potential, k, can be in principle different for every window, but in practice, it is common to use the same value for all the windows. The MD simulations are used to obtain the biased probability distribution along the reaction coordinate, $P_j^b(\xi)$. The free energy can then be shown to be equal to:

$$G_i(\xi) = -\frac{1}{\beta} \ln P_j^b(\xi) - \omega_j(\xi) + F_j \tag{2.22}$$

where

$$F_j = -(1/\beta) \ln \langle \exp \beta \ \omega_j(\xi)) \rangle \tag{2.23}$$

To calculate G_i from eq. 2.22, F_j needs to be evaluated. There are two mainstream methods to do this, umbrella integration and weighted histogram analysis method (WHAM). In this thesis, WHAM is used, as it is widely accepted and implemented in Gromacs and is also available as a standalone code[99].

2.11 Limitations of MD

Despite being an excellent method to study various systems at the nanometre scale, which enables us to access information about the system not available from experiments, MD has limitations. As previously noted, MD uses classical Newton's equations to describe motion of atoms and neglects their quantum mechanical nature. This inherently leads to approximations. Thus, it is always necessary to be aware of the limitations of MD and do checks with known experimental values.

Furthermore, the chemical bonds cannot be created or broken during the simulations described here, due to the nature of the harmonic potential between permanently bonded atoms. This can be overcome by using the Morse potential, (instead of the harmonic potential) which has a more accurate shape or a mixed quantum mechanical/classical methods can be used, where a part of the system is simulated as quantum mechanical, while the rest of the system remains classical. This comes with additional computational cost.

As mentioned in section 2.9, bond vibrations which are higher frequency than $\frac{k_b T}{h}$ exceed the classical limit, so they cannot be simulated using a classical harmonic oscillator. This includes most bond stretching and some bond-angle vibrations. To overcome this problem, corrections can be applied to the total internal energy and specific heat capacity. Another way to deal with this is to apply constraint algorithms.

The form of the FF itself imposes restrictions on the simulations. Polarization of atoms is not possible with classic FFs described here. Polarizable FFs are under active development, but the number of available residue types is still limited.

PBCs are unnatural. When simulating liquids, we want to avoid boundaries with a vacuum to simulate a bulk system. PBC enables us to avoid dealing with phase boundaries, but since the system is not truly periodic it is not entirely physical. For

larger systems the error is negligible, but for small systems, internal correlations can be increased due to PBC.

MD simulations are very computationally intense and the number of the computations required scales with the size of the system. The specific scaling depends on the chosen simulation settings as some algorithms are faster than others. For the simulations presented in this thesis, which range from tens of thousands of atoms to hundred and fifty thousands atoms, use of a High Performance Computer (HPC) cluster is required.

2.12 Practical approach to MD simulations

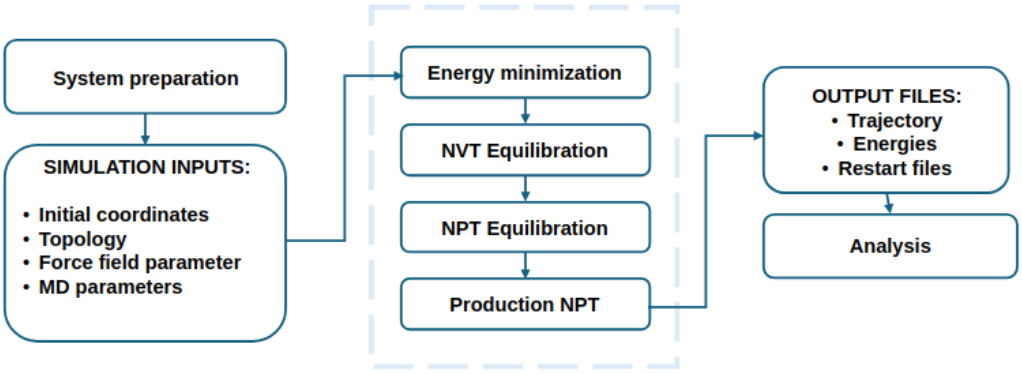

Figure 2.5: Typical flowchart for MD simulation

In this section, some practical aspects of conducting MD simulations will be discussed. A typical MD simulation workflow is provided in Fig. 2.5. As can be seen from this figure, the the first step to the simulations is the prepare the system to obtain the input files for MD software.

2.12.1 System preparation

The coordinates of the main structures [8] to be studied can be obtained in several ways. For the work presented in this thesis these are:

[8] Atoms and molecules that are not solvent.

- A Python script that produces chitin/chitosan oligomers and crystal structure from XRD obtained coordinates.
- The web server CHARMM-GUI that can create various bio-molecular and inorganic structures.

The coordinate file formats are typically .pdb (protein data bank, NAMD compatible) and .gro (Gromacs compatible) The topology file is complementary to the coordinate file and describes all the bonded interactions in the system. CHARMM-GUI creates topology files alongside the coordinate files. NAMD and Gromacs software packages come with code (psfgen and gmx gromp) that can create topology files when provided with coordinate files and residue topology found in the FF. The topology file formats are .psf (NAMD) and .top (Gromacs). Lastly, MD parameters are written in a separate file and describe the specifics of the algorithms to be used. For example, which integrator will be used with what timestep, and what temperature and pressure coupling will be used.

2.12.2 EM and Equilibration

The MD simulations are typically conducted in stages. The first stage is energy minimization (discussed in Section 2.5). Once the system is close to the energy minima it needs to be carefully equilibrated to avoid unphysically large forces. Typically, this is done in several stages. First, only solvent is allowed to equilibrate at room temperature, while the non-solvent molecules are frozen or restrained. This typically requires only a short simulation. Next, the whole system will be equilibrated by applying a series of short NPT (sometimes NVT is required before NPT) simulations where the restraints on the non-solvent molecules are progressively reduced and eventually removed. The production (main) run is then initiated, typically using an NPT ensemble.

2.12.3 Production run and analysis

The Production runs described in this thesis are performed at room temperature (300 K) and atmospheric pressure (1 bar). The reasoning for this is two-fold: the analogous

experiments would be conducted at similar conditions and the CHARMM36 FF has been optimised for this range of temperature and pressures. The length of the production run is dependent on how fast equilibrium is reached and the characteristic times during the equilibrium simulation.

The simulation should be long enough that it represents a good sampling of the equilibrium space-phase landscape. When the simulation is completed, the resultant trajectory is analysed. Analysis can be done in multiple ways, using software such as VMD and its in-built functions, or using custom scripts written in languages such as TCL and Python. In this thesis, a goal orientated approach to analysis has been used, so in each case the method which yields the most computationally efficient result has been used, regardless of code required. The details of analysis will be given in the each results chapter as they differ from system to system.

2.13 Chapter summary

Gromacs and NAMD are open-code engines, which implement MD simulation algorithms that accurately calculate time evolution of the biomolecular system in an aqueous solution, enabling temperature and pressure control of the system, while balancing speed and accuracy. CHARMM FF is able to model a variety of biomolecules and is compatible with INTERFACE FF for non-organic minerals and metals, making it particularly suited for the work presented here. Standard MD simulations are used to study spontaneous processes such as adsorption of a biopolymer from solution to a surface, or the behaviour of a polymer in solution. Non-equilibrium methods such as SMD and US can be used to study hydrogen-bond breaking and calculating free-energy of adsorption along a reaction coordinate. MD enables us to study system properties which are inaccessible to experiment, while being able to provide good agreement with those properties that are experimentally measured.

Chapter 3

Model Validation

3.1 Introduction

FF validation is a crucial initial step for conducting research which relies on computational simulations. It ensures the physical accuracy of the model and thus provides confidence in predictions made using the model. In this chapter, various systems containing chitin and chitosan oligomers are constructed, with increasing size and complexity. The conformational states of chitin and chitosan are calculated and compared to the literature. The silica model is chosen and validated against available literature. The simulation setup established here lays the groundwork for the novel results presented in the later chapters of this thesis.

Chapter aims:

- To develop a Python script which assembles chitin and chitosan monomers into oligomers, and to create a model crystal from chitin polymer, which will be used in subsequent chapters.
- To construct simple chitosan oligomers to test the model for correct reproduction of physical properties, such as glycosidic linkage conformation.
- To choose an appropriate silica model which will enable the study of the silica chitosan adsorption process.

3.2 Methods

3.2.1 Chitin and Chitosan

Initial coordinates

A Python script was developed to construct chitin and chitosan oligomer and crystal structures. It reads the input file containing the monomer sequence and outputs the coordinates file (.pdb) with the desired oligomer sequence. This coordinate file can be used as input for the psfgen code, which produces a topology file (.psf). The initial coordinates for chitin (acetyl-β-glucosamine) and chitosan (β-glucosamine) monomers were obtained from[72] in Gromacs coordinates format (.gro).

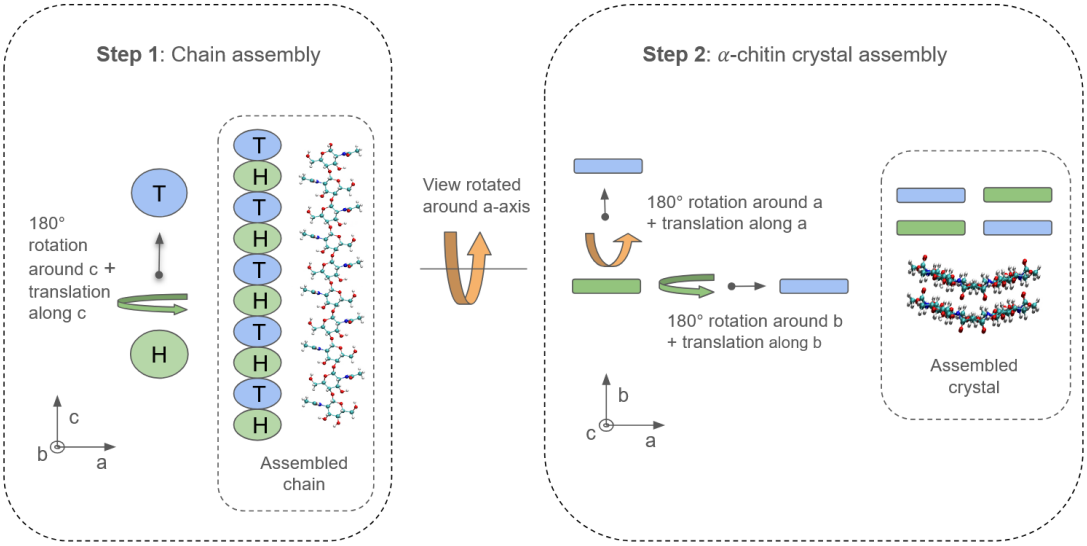

Figure 3.1: Schematic illustrations of chitin (or chitosan) oligomer and crystal structure assembly.

Fig 3.1 illustrates the process of oligomer and crystal assembly. The 2_1 rotational symmetry can be illustrated as rotations and translations of a coin which has head (H) and tail (T) sides, as can be seen in the figure. First, the monomer is rotated by 180° around the c crystallographic axis, which is then followed by a translation of c/2 unit cell along the c-axis. This type of rotation and translation is repeated until the desired chain length is achieved. Next, the assembled chain is then similarly rotated around

the b-axis by 180° followed by a translation of b/2 unit cell length along the b-axis to form a sheet, and rotated around the a-axis and translated by a/2 unit cell length to stack chains. The crystal assembled in such fashion will have $P2_12_12_1$ symmetry characteristic for α-chitin crystal. If the rotation around the b-axis is omitted, β-chitin crystal will be formed.

Simulated oligomers consist of protonated glucosamine (P), neutral glucosamine (N) and acetyl-glucosamine (A) monomers, which are shown in Fig. 3.2. First, dimers consisting of two monomers were constructed with the composition A+A, A+P, N+P, N+N and P+P. These were solvated with TIP3P water and chloride ions were added to neutralise the system in the case of P monomers (which have charge +1). Following the successful simulation of dimers, a series of 10-mers was constructed. Each oligomer was solvated with TIP3P water and an appropriate number of chloride ions was added to neutralise the system.

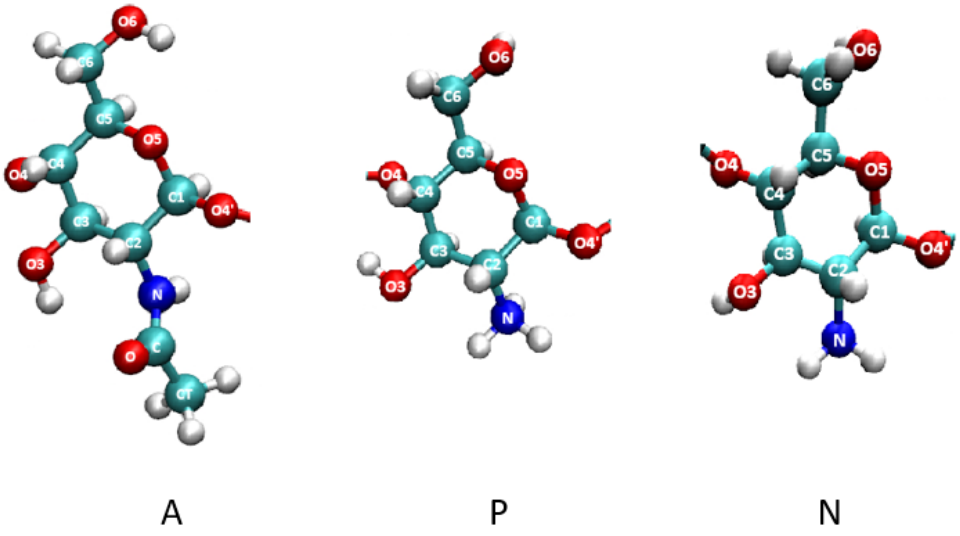

Figure 3.2: The monomers used for the simulations of chitin and chitosan with atom names: A - acetyl-glucosamine, P - protonated glucosamine and N - neutral glucosamine.

Lastly, after successful simulations of individual oligomers in water, the three different crystals structures were constructed: α-chitin crystal with 4×4×10-monomer

arrangement and neutral α-chitosan crystal, and 50% protonated α-chitosan crystal, which both had 3×6×10-monomer arrangement. As before, the systems were solvated with the water box sufficiently large to avoid any self interaction across periodic boundary. Sodium was added to the system to neutralise it and further sodium and chloride ions were added to set the bulk salt concentration to 0.15 mol L^{-1}.

Simulation parameters

The general simulation protocol was as follows. Initially, the oligomers were frozen, while minimalization was run for 1000 steps. Then, water was equilibrated for 1 ns at 300 K and 1.01325 bar using a Langevin thermostat and barostat. The electrostatics were managed using Particle Mesh Ewald (PME), and rigid bonds were applied to water using the SETTLE algorithm. Next, the oligomers were released and the system was again minimized for 1000 steps before being gradually heated from 0 to 300 K for 3 ns. Lastly, the production runs were conducted for 6, 18 and 26 ns for dimers, 10-mers and crystals respectively.

Angles and dihedral definitions

The main goal for the analysis of the oligomer systems was to ensure the correct conformational states in the simulations. Thus, the glycosidic linkage angle and dihedral angles accross the glycosidic bond were calculated. In the literature there are two ways to define these dihedral angles, so here comparison is made to both with the following definitions:

- ν = C1-O4-C4
- ψ = C1-O4'-C4'-H4'
- ϕ = H1–C1–O4'–C4'
- ψ^b = C1-O4'-C4'-C3'
- ϕ^b = O5-C1-O4'-C4'

where ' denotes the atoms of the subsequent monomer.

3.2.2 Silica model

Chapter 5 explores the interaction of chitosan oligomers with a siNP surface. Here, a silica model was chosen and initial simulations were conducted to verify the model's suitability. Silica, as an inorganic compound, is not part of traditional FFs which mainly consist of biomolecules, small organic compounds and common solvents. Thus, a suitable FF had to be chosen to model the silica surface. The requirements for such a model are: correctly reproducing silica surface charge density, correctly reproducing silica interaction with water, and compatibility with the CHARMM FF. The INTERFACE FF fulfils these requirements. Furthermore, it is implemented into the CHARMM-GUI nanomaterial builder, which makes it easy to use.

Initial coordinates

A silica slab, shown in Fig. 3.3 ($7.49 \times 7.44 \times 2.6$ nm^3) with periodicity in the $x-y$ plane was constructed using the CHARMM-GUI[100] nanomaterial modeller[101] with an α-cristobalite structure and a surface silanol (Si–OH) group concentration of 4.7 nm^{-2}. The silanol deprotonation level was 6.66 % (0.31 nm^{-2}) to mimic pH $\approx$ 5 and was determined as recommended by Emmami *et al.*[102]. This pH level was chosen because chitosan is soluble at pH below $\approx$5.4.

The system was solvated and sodium ions were added to neutralise the system. Further sodium and chloride ions were added to set the bulk salt concentration to 0.15 mol L^{-1}.

Simulation parameters

The simulation was performed in Gromacs 2022. The system was initially minimised for 5000 steps using the steepest descent method, with the silica slab restrained using harmonic potentials. The water molecules and ions were then equilibrated for 0.5 ns using the Berendsen thermostat at 300 K and the Parinello-Rahman barostat with anisotropic pressure coupling at 1.0 bar. After initial equilibration, the system was simulated using the Nose-Hoover thermostat at 300 K, the Parinello-Rahman barostat at 1 bar with anisotropic pressure coupling with 0.2 ps time constant for coupling and

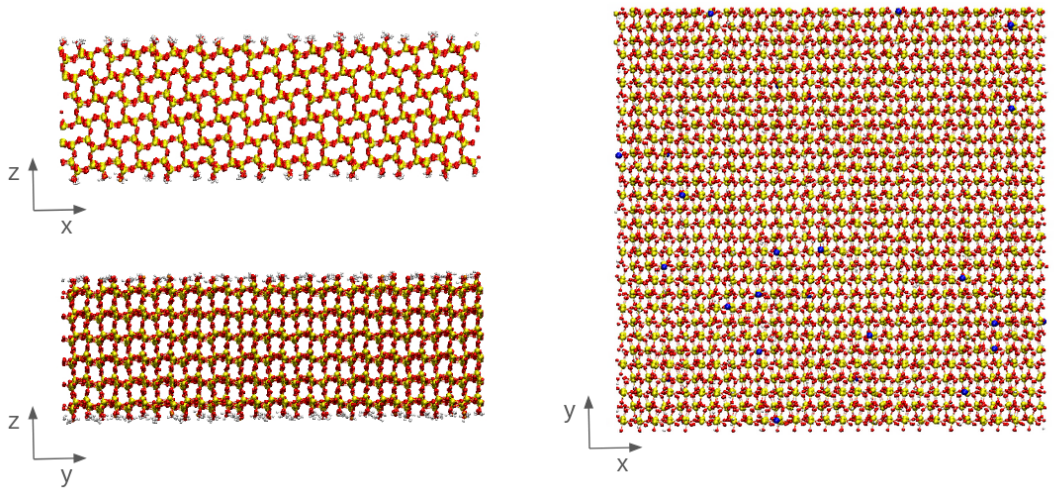

Figure 3.3: Constructed silica slab shown from different viewpoints with atom colours : oxygen - red, deprotonated surface oxygen - blue, silica - yellow, hydrogen - white.

compressibility of 2.5×10^{-6} bar^{-1} in the x and y directions and 4.5×10^{-5} bar^{-1} in the z direction and 2 fs timestep integration. The electrostatics were calculated using Particle Mesh Ewald with a 1.2 nm cutoff. The LINCS constraints algorithm was used to restrain O-H bonds. Periodic Boundary Conditions (PBC) are used, so that the silica slab is infinite in the x- and y-directions, with the solution sandwiched between silica slabs. Analyses were performed using Gromacs built-in tools.

3.3 Discussion and Results

3.3.1 Chitin and Chitosan

Dimers

The angle ν describes the connection of the two monomers which form a dimer. The experimentally obtained values of ν were reported to be 116.7° and 114.2° for anhydrous[24] and hydrous crystalline[22] chitosan respectively using XRD method. Here, ν was found to be 114° for P+P and N+P dimers, and 115° for A+A, A+P and N+N dimers, which is consistent with the experimental values.

Snapshots of the observed dihedral angles can be seen in Fig. 3.4. The comparison

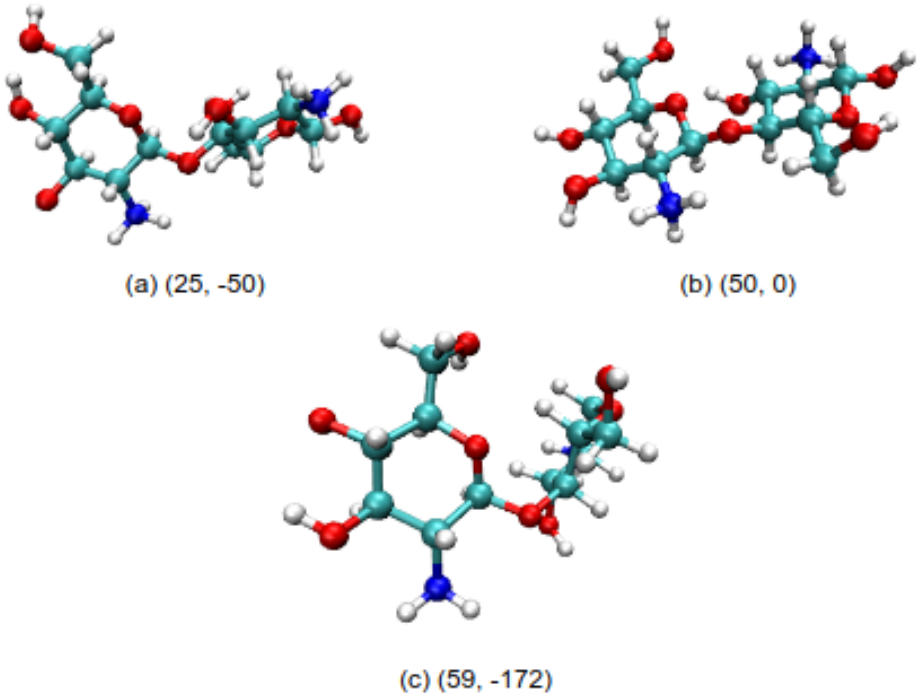

Figure 3.4: Snapshots of the observed (ϕ, ψ) configurations

between the results obtained here and other available data can be seen in Table 3.1.

Table 3.1: Averages of the dihedral angles at the glycosidic linkage. All angles are given in degrees. * indicates the range of values approximated from a figure.

	ψ	ϕ	ψ^b	ϕ^b	Method	Ref
hydr. chitosan	-	-	94.0	-92.1	XRD	[22]
Chitosan crystal	-	-	102.5	-83.4	*(aq)* MD	[72]
Chitosan molecule	-	-	110.5	-69.5		
Chitin molecule	-	-	110.5	-70.7		
chitin	[-50-50]*	[0-50]*	-	-	*(aq)* MD	[103]
CHT dimer	[-50-30]*	[25-60]*	-	-	MD	[104]
A+A	-40 ± 22	36 ± 13	83 ± 21	-86 ± 13	*(aq)* MD	
A+P	-33 ± 22	40 ± 13	89 ± 20	-82 ± 13		
N+P	-18 ± 23	46 ± 12	103 ± 21	-75 ± 12		
N+N	-22 ± 25	44 ± 13	101 ± 23	-78 ± 13		
P+P	-11 ± 23	49 ± 12	110 ± 22	-73 ± 12		

Table 3.1 shows the values of dihedral angles with a comparison available from the literature. A variation of values can be seen for the ψ and ϕ dihedral angles. The results

obtained here match the results obtained by Skovstrup *et al.*[104] who used implicit solvent MD/MC simulations. The dihedral angles oscillate during the simulation, hence a range of values is obtained, instead of a singular value. The ψ and ϕ values for chitin dimers compared to chitosan dimers indicate the structural difference around the glycosidic linkage. The molecules solvated in water have higher flexibility than the polymer chains found in water, which explains the difference between the experimental and the simulation data. Chitin has a higher population of negative values for ψ angle due to the presence of the intrachain O5 – OH3-O3 H-bond and exoanomeric effect, this is consistent with results obtained for hexamers[105].

Naumov *et al.*[72] developed and used the GROMOS56acarbo force field in GROMACS MD, with SPC water. Their results are overall comparable to the results obtained here, with an excellent agreement for the P+P dimer and CHT molecule. However, they obtain the same result for ψ^b and ϕ^b distribution they obtain for chitin and chitosan molecules. This can be explained by the lack of detailed parameterisation for the acetyl residue in chitin.

10-mers

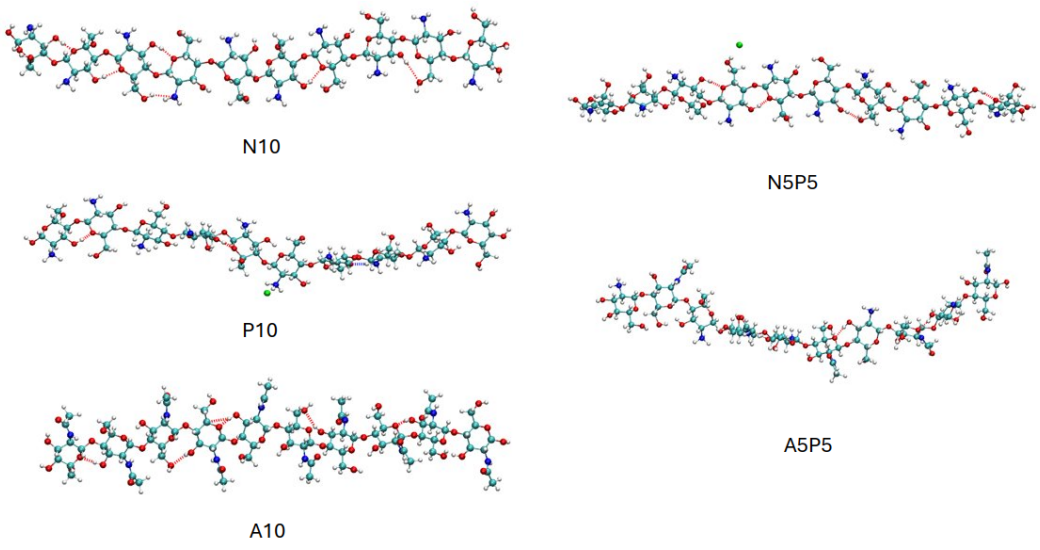

Figure 3.5: Snapshots of the simulated 10-mers. Hydrogen bonds shown as dashed red lines.

The snapshots of the 10-mer oligomers during the simulation are shown in Fig.3.5. chitin and chitosan's persistence lengths are expected to be around 5 nm[106], which is similar to 10-mers fully extended length (≈5.3 nm). Thus, it is expected that the oligomers adopt mainly extended form as can be seen from the snapshots. The oligomers containing P monomers exhibit higher flexibility due to the presence of the chloride ions, which can disrupt intrachain hydrogen bonding[107].

To further examine the structure of simulated 10-mers, the distribution of dihedral angles ϕ, and ψ was plotted and can be seen in Fig. 3.6. The range of the dihedral angles observed is consistent with the typical distribution for the C1 to C4 linked pyranose chains. As before, there is a lot of similarity between all four cases. Each semi-transparent point on the graph represents one sampling of the dihedral angles between two joined residues on the chain. The dihedral angles were sampled every 20 ps. Thus, the higher opacity areas in the graph indicated higher occurrence for the specific configuration.

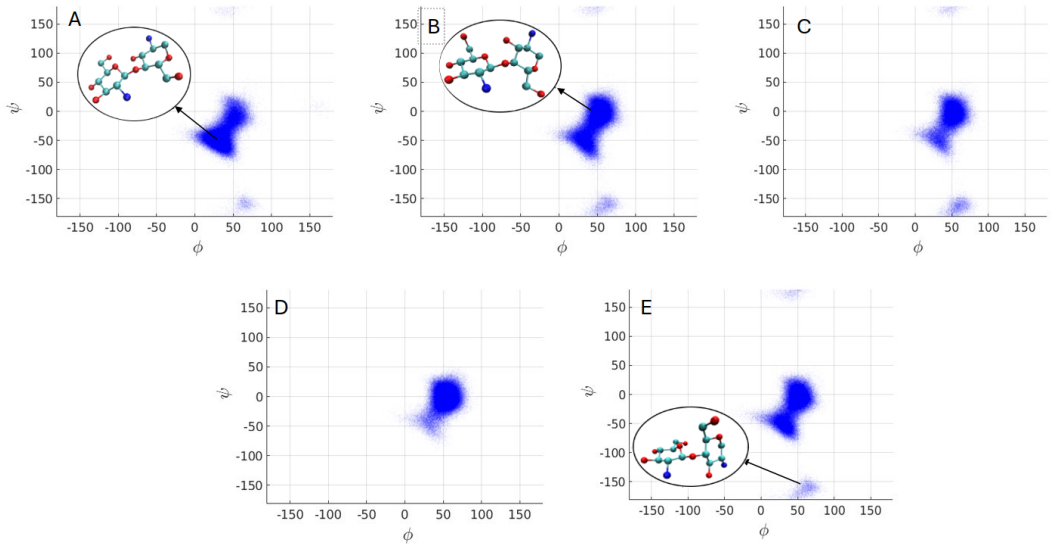

Figure 3.6: The distribution of dihedral angles ϕ and ψ for the simulated 10-mers, A - A10, B - A5P5, C - N5A5, D - P10, E - N10. The snapshots illustrate (ϕ,ψ) configurations of interest.

In the case of the chitin oligomer (A10) the most likely configuration is around $(\phi, \psi) \approx (25°, -50°)$, with a significant population around $(50°, 0°)$ as well. Interest-

ingly there is a small population around $(60°, -160°)$, which indicates the presence of local metastable energy minima. The completely protonated deacetylated chitosan decamer has the highest population around $(50°, 0°)$. The chitosan decamer with 50 % DA, P5A5 has the characteristics of both chitin and fully protonated and deacetylated decamers, as expected. The tendency for ψ angle in chitin to have a larger negative population is consistent with the behaviour observed in dimers.

Crystal structures

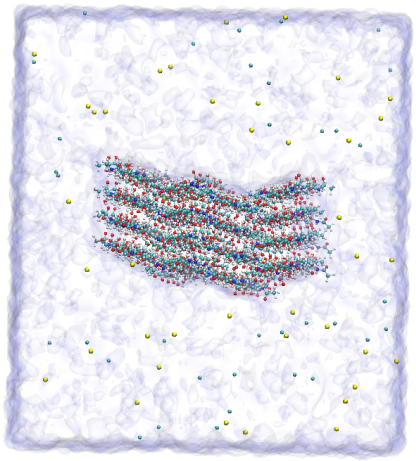

Figure 3.7: α-chitin nanocrystal during simulation.

Simulations of the crystal structures were conducted to study the solubility of chitin and chitosan nanocrystals in aqueous solution. The two chitosan nanocrystals were made of 3×6 10-mer long oligomers, while chitin nanocrystal consisted of a 4×4 10-mer long oligomers. In all three simulations, all the surfaces were exposed to water which had 0.15 mol L^{-1} sodium chloride concentration. The chitin and neutrally charged chitosan crystals,did not dissolve during the simulation. Fig. 3.7 shows α-chitin crystal during the simulation.

As can be seen, the crystalline structure remained largely unchanged with hydrogen bonding remaining stable for the duration of the simulation. The hydrogen bonds during the simulation were analysed as shown in Fig. 3.8A. Here, the hydrogen bonds can be classified as intrachain - these bonds stabilise the chitin's 2_1 chain configuration,

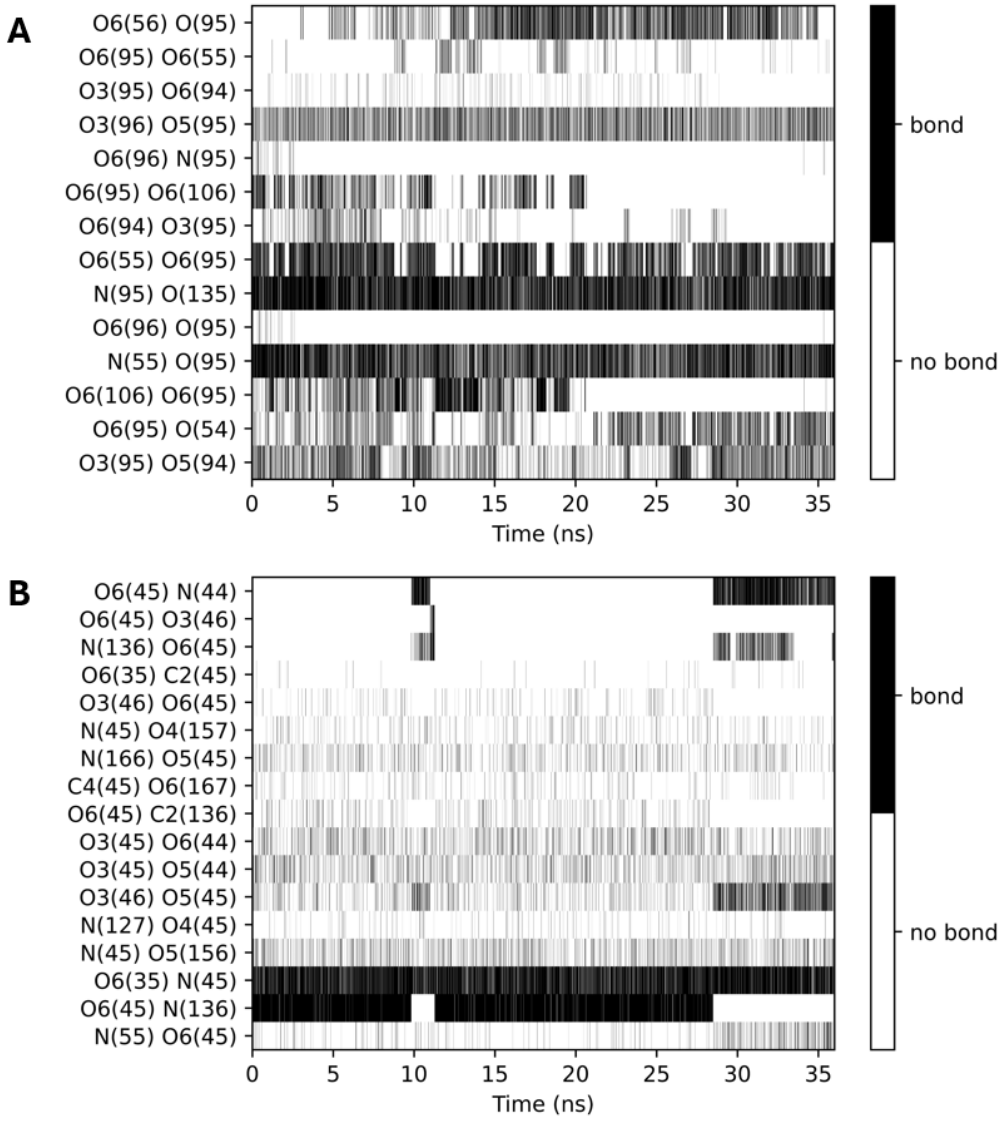

Figure 3.8: Hydrogen bond analysis for the (A) chitin monomer (residue 105) located in the centre of the chitin crystal and chitosan neutral monomer located in the middle of neutral chitosan crystal (B). The bonds are shown in donor-acceptor order. The number in bracket refers to the residue number.

intrasheet - the hydrogen bonds which contribute to lateral stacking and the intersheet bonds - which control the vertical stacking of the sheets. The chitin chain is stabilised by the intra-chain O6–HO6—O3 and O3–HO3—O5 hydrogen bonds. Intra-sheet hydrogen bonds are characterised by low occupancy O6–HO6—O6 bonds. The main hydrogen bonds contributing to intersheet bonding are O6–HO6—O6 and N–HN—O

which have the highest occupancy. These findings agree with the hydrogen bonds described by Sikorski *et al.*[21] who used high resolution synchrotron X-ray diffraction data to describe α-chitin crystal structure.

Similarly, the neutral α-chitosan crystal is stable in an aqueous solution, as indicated by the hydrogen bond analysis shown in 3.8B. As in the case of α-chitin crystal the chain structure is stabilised by the intra-chain O6–HO6—O3 and O3–HO3—O5 hydrogen bonds. Unlike chitin, the chitosan NC has a high occupancy intersheet O6–HO6—N hydrogen bond and low occupancy O6–HO6—O3, the same as chitin crystal. Intersheet bonds identified are O6–HO6—O3, N–HN—O4, N–HN—O5 which have lower occupancy compared to the O6–HO6—N intersheet bonds.

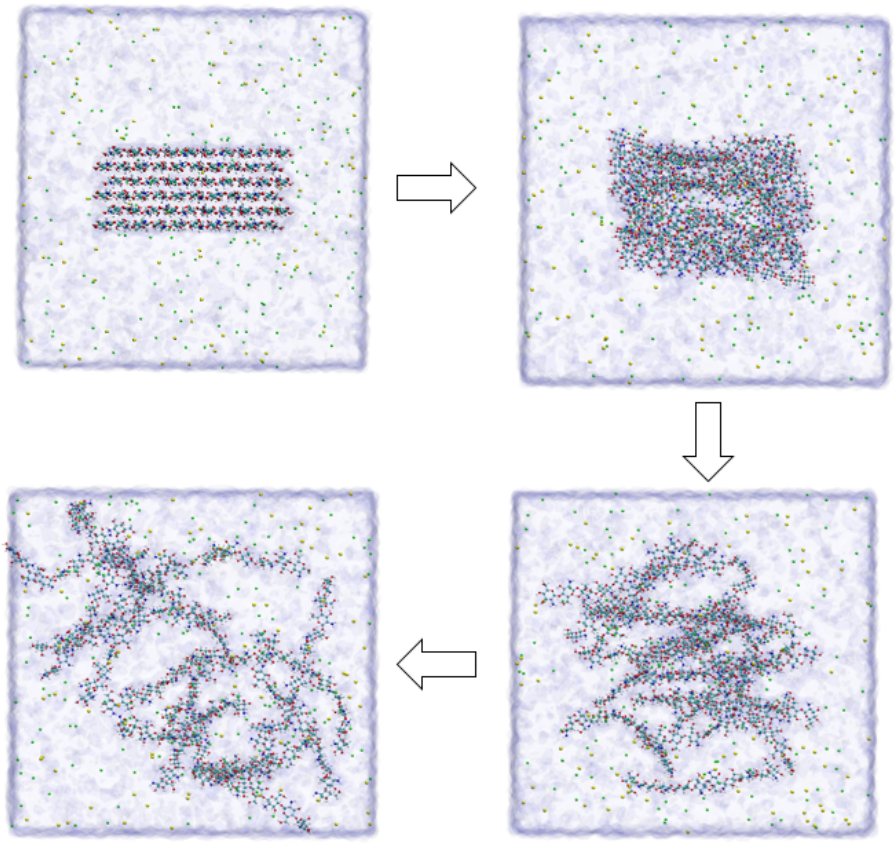

Figure 3.9: Dissolution process of protonated α-chitosan NC. Water not shown for clarity.

On the other, hand protonated α-chitosan crystal immediately started to dissolve.

Fig. 3.9 shows the dissolution process. The initial crystal structure is shown in the top left corner. The top right snapshot shows the chitosan chains adopting helical structure characteristics for solvated chitosan and chitosan strands starting to separate from each other. The final two snapshots show the chitosan crystal fully dissolved. This type of dissolution is in agreement with the MD simulations study by Naumov *et al.*[72].

3.3.2 Silica simulations

A silica slab in 0.15 mol L^{-1} sodium chloride aqueous solution was constructed to study the properties of the silica-water interface and to assess the model's accuracy for further research of the chitosan - silica interaction at this interface which is presented in chapter 5.

The time-averaged density of water at the silica water interface is shown in Fig. 3.10. The figure shows water layering at the silica surface with two peaks before the density value decays to the bulk water density. This is consistent with a previous AFM study of the water-silica interface[108].

The behaviour of ions in solution near the silica interface is also of importance. The electric double layer (EDL) is a widely known phenomenon which occurs at the aqueous interface of charged surfaces. The ions effectively screen the surface[109]. Fig. 3.11 shows the time-averaged density of sodium and chloride ions in solution. In the graph, it can be seen that sodium ions form three peaks. The higher peak is near the surface at -1.3 and 1.3 nm, while the second and third less noticeable peaks are at $\pm$1.6 and $\pm$ 1.7 nm before the density decays to the bulk solution value of 0.30 mol L^{-1}. Chloride ions, which are negatively charged are repelled from negatively charged silica surfaces and thus have low density at the interface which increases to 0.29 mol L^{-1} in the bulk region.

Furthermore, being able to distinguish the interfacial region from the bulk region is important for determining the appropriate water box size for the simulations which are conducted in PBC as is the case here. Having a sufficiently large bulk solvent region ensures the two silica surfaces cannot interact with each other and thus disrupt processes such as adsorption that are studied in later simulations.

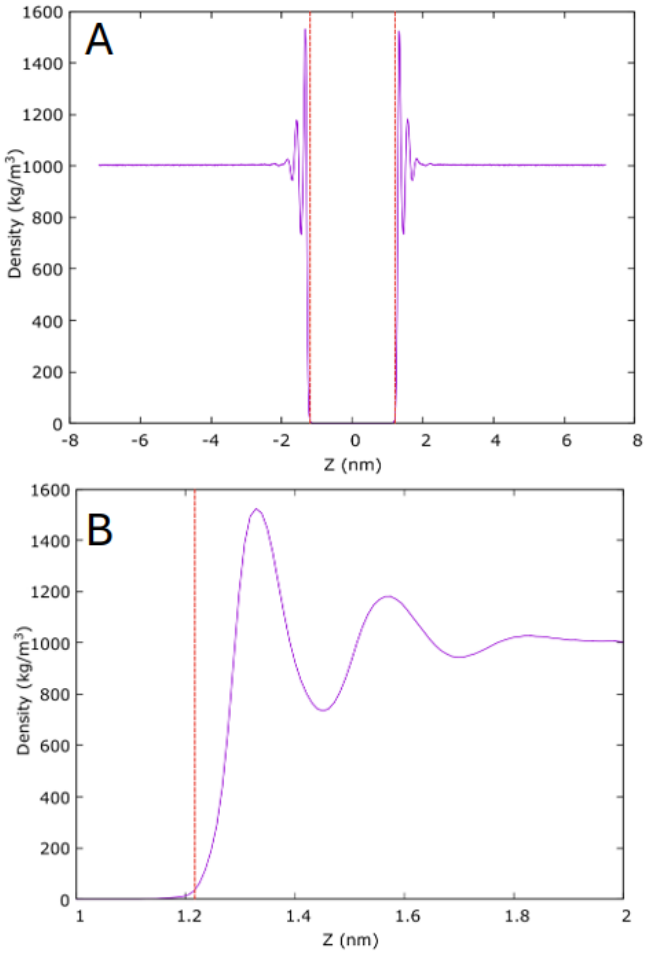

Figure 3.10: Time averaged density for water (A), interfacial region zoomed in (B). Silica surface is indicated by dashed red line.

3.4 Conclusions

A number of chitin and chitosan oligomer and crystal structures were simulated. Firstly, the aim was to verify the accuracy of the FF and the topologies. There has been an increase in scrutiny of the accuracy of the MD force fields and the topologies which are widely used. Thus, care was taken to ensure the validity of the parameters used.

Secondly, the aim was to understand the physical properties and dynamics of the small chitosan chains. Understanding the fundamental behaviour of small-length chains is essential in determining their fundamental properties. The results indicate broadly

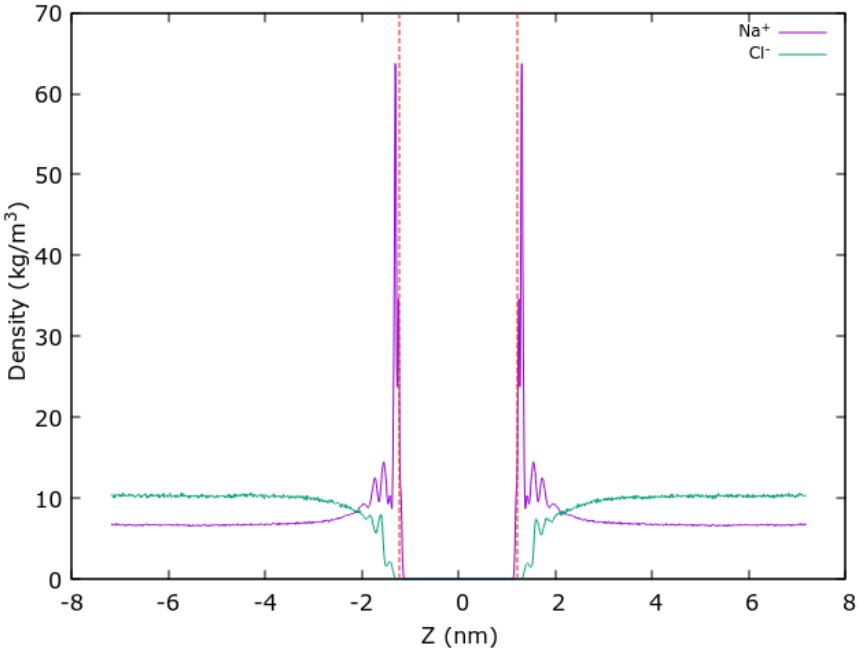

Figure 3.11: Time averaged density profile for the ions in solution.

similar structures with subtle differences between the oligomeric species. In the longer chains, these smaller differences accumulate and likely result in changes to the macro-properties of the polymers.

The dihedral angles relevant for the glycosidic linkage in aqueous oligomers were consistent with previously published studies, which were conducted using different FF parameters and experimental studies, thus it can be concluded that the FF used here is valid. Several typical configurations were found, which most likely correspond to local energy minima in the $\phi - \psi$ landscape. These are (25,-50), (50,0) and (55, -160). Notably, the (55, -160) has a much smaller occupation, and its stability is still not fully clear. The intra-chain and the polymer-water hydrogen bonding are likely affecting the conformational properties of the chains, so a better analysis for hydrogen bonding needs to be developed.

The silica slab was modelled using Interface FF, which is a physically accurate FF. The model validity was assessed by conducting an MD simulation with the water interface. The results show the water ordering at the interface and the formation of EDL due to the presence of the monovalent ions, which is in agreement with experimental

literature.

To conclude, in this chapter model validation simulations were successfully conducted, laying the groundwork for the future work presented in this thesis.

Chapter 4

Chitin and Chitosan Binding to α-chitin Crystal

In this chapter, binding of chitin and chitosan to a model α-chitin nanocrystal (α-chNC) (100) surface will be explored. Understanding the binding of chitin oligomers to the surface of α-chNC is important for improving the enzymatic de-acetylation of chitin. The enzyme needs to be able to do enough work to overcome the binding energy of the crystal. Furthermore, understanding chitosan interaction with α-chNC is important for the design of chitosan coated α-chNC, which have a potential to be used as an antimicrobial spray coating or an additive to thin-films used for food packaging. Such films have been designed experimentally, but lack structural characterisation which can lead to their further optimisation.

Chapter aims:

- To construct the α-chNC structure in silico and evaluate the crystal's cohesive energy.
- To conduct MD simulations of chitin and chitosan oligomers interactions with α-chNC in aqueous solution.
- To calculate free energy of adsorption of chitin and chitosan oligomers to the α-chNC (100) surface.

4.1 Methods

The simulations in this chapter were performed using the NAMD package (versions 2.12 and 2.15).

4.1.1 Structures

The α-chNCs as well as chitin and chitosan oligomers were constructed *in silico*, based on experimentally determined data as described below. The chitin and chitosan monomer coordinates were obtained from Naumov *et al.*[73], and assembled into oligomers and an α-chNC[21] using an in-house Python script. The α-chNC was constructed from 10-monomer-long β-1,4 linked acetylglucosamine units, arranged in a six-by-six arrangement. The chains were placed in an antiparallel fashion to obtain the desired $P2_12_12_1$ symmetry lattice.

For future reference, the atoms in the chains are labelled in Fig. 4.1.

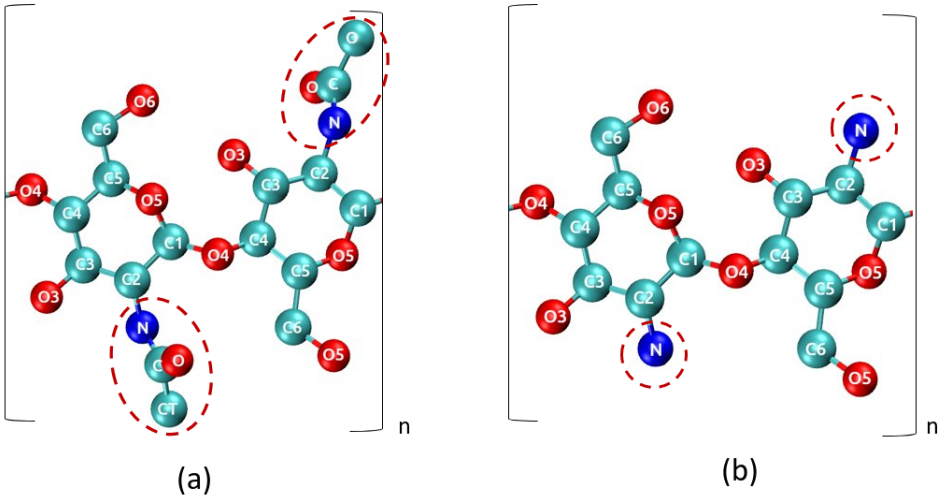

Figure 4.1: The atomic structure of chitin (a) and chitosan (b) with atom names (coloured atom type C = cyan, N = blue, O = red); hydrogens are omitted here for clarity. The naming convention used here for hydrogens adds H before its heavy atom, e.g. HO6 for hydrogen belonging to O6. The chitin chain has 2_1 symmetry along the chain, as shown in the dimer here. The structure of chitosan (N-glucosamine) differs from chitin (N-acetylglucosamine) only in the absence of the acetyl group on the amino group, as indicated by circles in red.

4.1.2 Bulk crystal and surface energies in vacuum

The calculations for the binding energies of the chitin were performed in vacuum. Periodic boundary conditions (PBC) were used in all three directions, always creating the bulk crystalline structure in the x,y-directions. A vacuum gap was added in some simulations along the z-axis to expose the (100) crystal surface. This surface was chosen as it presents a stable interface with water[110] which means that this surface is also likely to be present experimentally. Model crystals with surfaces in vacuum were constructed to study the binding energies associated with a step and an ad-chain, as can be seen in Fig. 4.2. The step shown in Fig. 4.2(b) was constructed by removing three chains from the top surface of the α-chitin crystal (Fig 4.2(a)). The ad-chain shown in Fig. 4.2(c) was constructed by adding a single chain to the surface of the α-chitin crystal (Fig. 4.2(a)) in the antiparallel direction to the crystal surface.

The cohesive energy per chain of the bulk crystal was calculated using the following relation: $E_{\text{cohesive}} = E_{36\text{bulk}}/36 - E_{\text{chain}}$, where $E_{36\text{bulk}}$ is the potential energy of the bulk crystal consisting of 36 chains, with PBC used to create a perfect space-filling crystal structure in all three directions, and E_{chain} is the potential energy of a single chitin chain in a vacuum.

The total surface energy (E_{surface}) was calculated from the difference between the potential energy of the bulk crystal ($E_{36\text{bulk}}$) and that of the relaxed crystal when the vacuum gap was present (note that this creates two equivalent surfaces at the top and bottom of the slab illustrated in Fig. 4a. Similarly, the step energy was calculated by comparison between the potential energies of a system with 33 'bulk' chains, E_{33} (Fig. 2b) and the surface energies of the two crystal surfaces, using the following relation: $E_{\text{step}} = (E_{33} - \frac{33}{36}E_{36\text{bulk}}) - E_{\text{surface}}$. The energy due to the additional chain was calculated using: $E_{\text{add-chain}} = (E_{37} - \frac{37}{36}E_{36\text{bulk}}) - E_{\text{surface}}$.

4.1.3 Oligomers in solution

Several chito-oligomers (oligomers consisting of acetylglucosamine and glucosamine monomers) were constructed and placed in a simulation box with the α-chitin crystal as described in the previous section. The structure of the chito-oligomers is shown

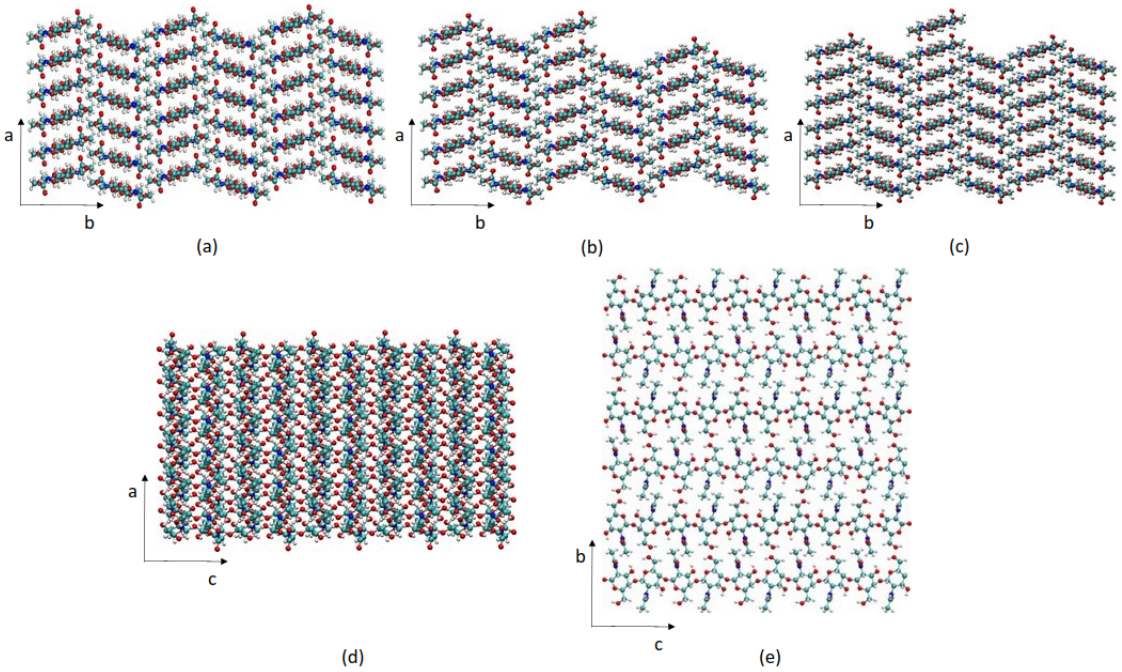

Figure 4.2: Crystal structure models used to assess the binding energy of chitin. The α-chitin crystal (a) consisted of six by six 10-monomer long chains connected across the periodic boundary in the c-direction, the views along other axes are shown in (d) and (e). This model is used to calculate the bulk crystal binding energy, and the surface energy when a vacuum gap is employed. Three chains were removed from the surface of the crystal to obtain the step configuration in (b). In (c), an additional chain was added to the top of the surface in the antiparallel direction to assess the ideal binding energy of a single chain.

in Fig. 4.3. The oligomers were placed parallel to the (100) crystal surface to simulate the adsorbed system, and 10 Å above the crystal surface to simulate oligomers in solution. Motion of the oligomers in solution is diffusive until adsoption.

The composite systems were solvated using TIP3P water, and 18 sodium and chloride ions were added to the solution to give a concentration of 0.15 mol L^{-1}. One such solvated system is shown in Fig. 4.4.

Initially, the water underwent energy minimisation for 1000 steps using the conjugate gradient algorithm, with non-solvent atoms frozen. The water was then equilibrated for 100 ps at 300 K using Langevin thermostat and at 1 bar anisotropic pressure coupling using Langevin barostat. Next, the entire system was minimised for a further 1000 steps and heated to 300 K over 300 ps in 10 K increments. The systems prepared

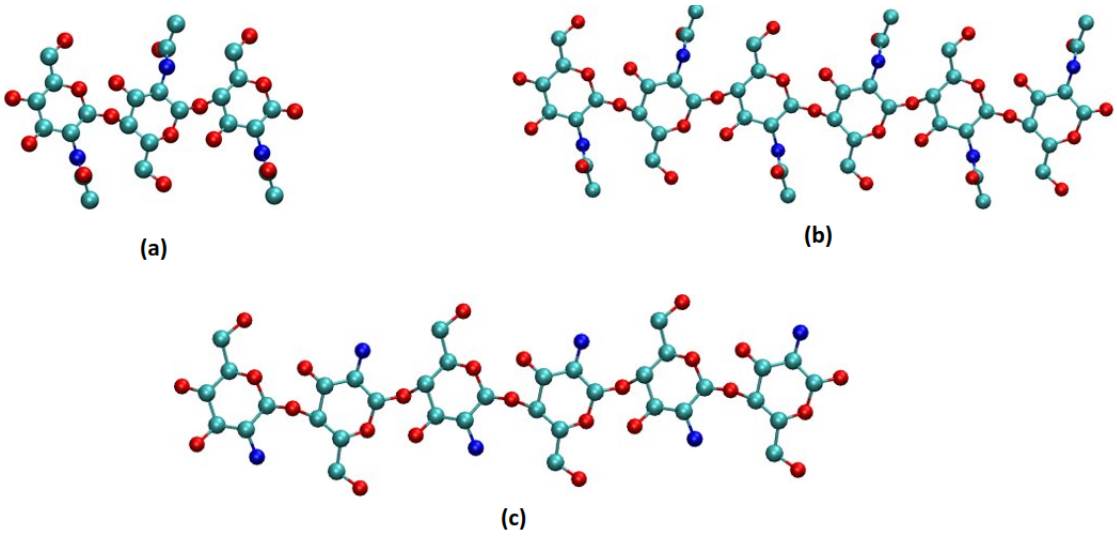

Figure 4.3: Structure of the modelled chito-oligomers: (a) A3, (b) A6 and (c) N6. A refers to the acetylglucosamine monomer of chitin, and N to the neutral glucosamine monomer of chitosan.

in this way were then used to initiate production MD runs of various durations in the NVT ensemble. The Langevin thermostat with 5 ps^{-1} damping was used to control the temperature with a 1 fs time step integrator. The electrostatics were calculated using PME with a 1.0 Å grid spacing and 12 Å cutoff for the van der Waals interactions.

4.1.4 Steered molecular dynamics

Steered MD (SMD) simulations were performed with a pulling velocity 10.0 Å ns^{-1} in the +z direction, which is normal to the (100) surface. The C4 atom (see Fig 4.1) in the first monomer of the oligomer was pulled and later used as part of the collective variable for umbrella sampling. The energy (dE) involved in breaking a bond between the oligomer and the nanocrystal surface was calculated using:

$$dE = \left(F_0 + \frac{dF}{2}\right)\frac{dF}{k} \tag{4.1}$$

where F_0 is the force after the bond breaking, dF is the change in force involved with detaching the chain and the spring constant k =1 kcal mol^{-1} $Å^{-2}$ [111].

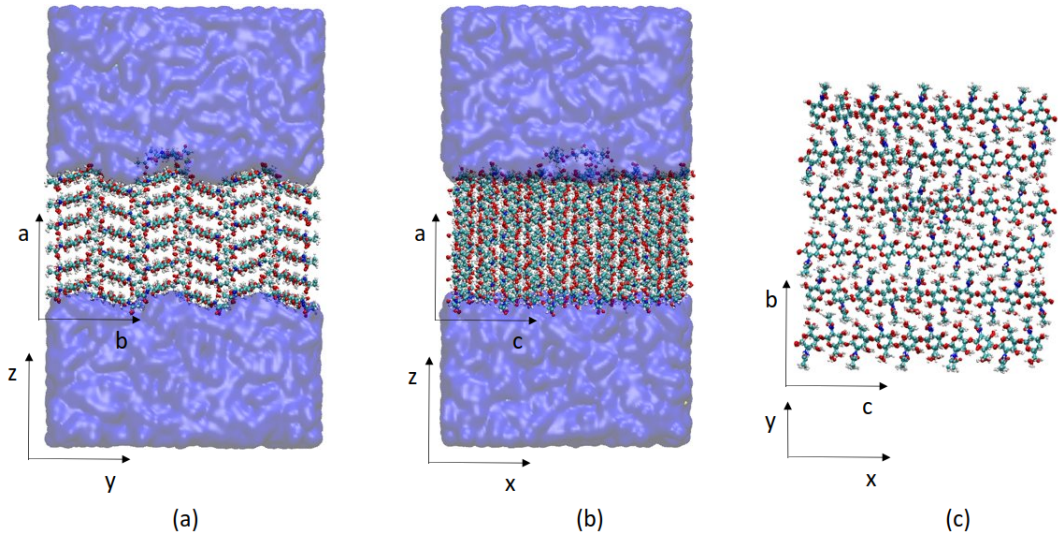

Figure 4.4: α-chitin crystal surface with an A3 oligomer placed on the (100) crystal surface. The system is rotated such that the (100) surface is in the x-y plane in the simulations. a) shows the simulation box view along the x-axis (c crystallographic axis), b) shows the view along the y-axis (b crystallographic axis), and c) shows the view from above along the z-axis. In c) water is omitted for clarity.

4.1.5 Umbrella sampling

Umbrella sampling (US) was used to obtain the free energy curve (FEC) of the projection of the distance of the C4 atom along the z-axis. The C4 atom chosen here is the same atom used for the SMD pulling. The (100) surface of the crystal was defined as the centre of mass of the C2 atoms in the top layer of the crystal. US is an enhanced sampling method that enables faster phase space sampling.

The simulation snapshots obtained from the SMD pulling were used for the US set. For each system, 20 windows were used, with 1 Å spacing between the windows for the A3 system, and 36 windows for A6 and N6 systems with same spacing as before. The constant used for the harmonic potential was $k = 2.5$, 5 and 6 kcal mol^{-1} Å^{-2}. The harmonic potential, V used for the enhanced sampling is given by $V = \frac{1}{2}k(\xi - \xi_0)^2$, where ξ is the collective variable and ξ_0 represents the target centre of each window. Here, the collective variable used is the previously described reaction coordinate.

Each window was simulated for 20 ns, with some windows extended up to 70 ns

when necessary (as further explained in the discussion). The FEC was then calculated using the weighted histogram method (WHAM) implementation by Grossfield[99].

4.1.6 Hydrogen bond analysis

The command "measure hbonds" implemented in VMD was used to calculate the number of hydrogen bonds, with a distance cutoff of 3.5 Å and 30° cutoff for the angle deviation from the 0° (180°) donor-hydrogen-acceptor angle as defined by the VMD plugin. The results were post-processed to plot the bonds of interest and calculate their occupancy. The hydrogen bonds involving water-chitosan interactions were calculated using the VMD hydrogen bonds GUI plugin in VMD.

4.2 Results

4.2.1 Free Energy Curves

The FEC obtained from the US for the A3 oligomer (Fig. 4.3(a)) is shown in Fig. 4.5. The FECs for the A6 and N6 oligomers (Fig. 4.3(b) and (c)) can be seen in Fig. 4.6. The curves calculated for chitin (A3 and A6) show good binding between the oligomer and the crystal, as indicated by the energy minima at short distances. The depth of the FEC minima is equivalent to the binding energy of the oligomer to the crystal surface. The total depth of the potential is ≈-3.8 and ≈-12.5 kcal mol^{-1} for A3 and A6, respectively. Overall the obtained FEC is relatively smooth with some minor local maxima present, which do not present significant free-energy barriers to the adsorption of the molecule from the solution. The FEC curves are approaching the asymptotic value, which is expected to be reached when no part of the oligomer is within the cutoff distance of the crystal surface. For 3-mer and 6-mers this distance is approx. 22 Å and 40 Å respectively.

There is a significant difference between the FECs for A6 and N6 oligomers (Fig. 4.6). The overall depth of the potential well of the N6 oligomer is six times lower than that of the A6 oligomer. The low binding energy between the N6 oligomer and the surface of the chitin crystal is most likely due to the absence of the acetyl group,

which is not present in chitosan. Our simulations imply that acetylamino-acetylamino group binding in the c-crystallographic direction (intersheet in the crystal) is much stronger than the acetylamino-amino group binding, which appears to be the cause of the difference in the binding energies. The importance of the acetyl group for the oligomer-crystal binding is further explored below in the SMD section.

Recently, an AFM study [112] showed that chitosan has 6 times higher affinity for hydrogen bonding to water than to chitin. This is comparable to the results obtained here that indicate 6 times weaker binding affinity of chitosan to the chitin crystal, compared to the chitin binding affinity to the chitin crystal.

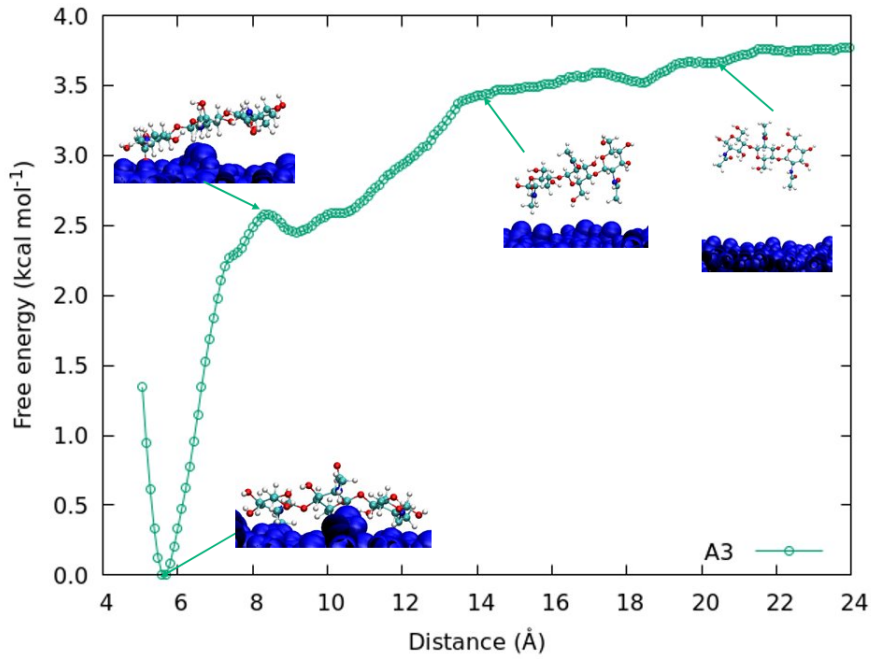

Figure 4.5: Free energy landscape for A3 oligomer, with snapshots of the system at different reaction coordinate (distance).

The convergence of the US set cannot be directly assessed. Due to the possibility of uneven sampling, certain regions of the energy profile could be undersampled leading to the energy profile not converging to true value. Hence, the consistency of the results is indirectly evaluated.

The shape of the obtained FECs resemble the potentials of mean force (PMFs) obtained in a study of the self-assembly of cellulose nanocrystals using US[113], as can

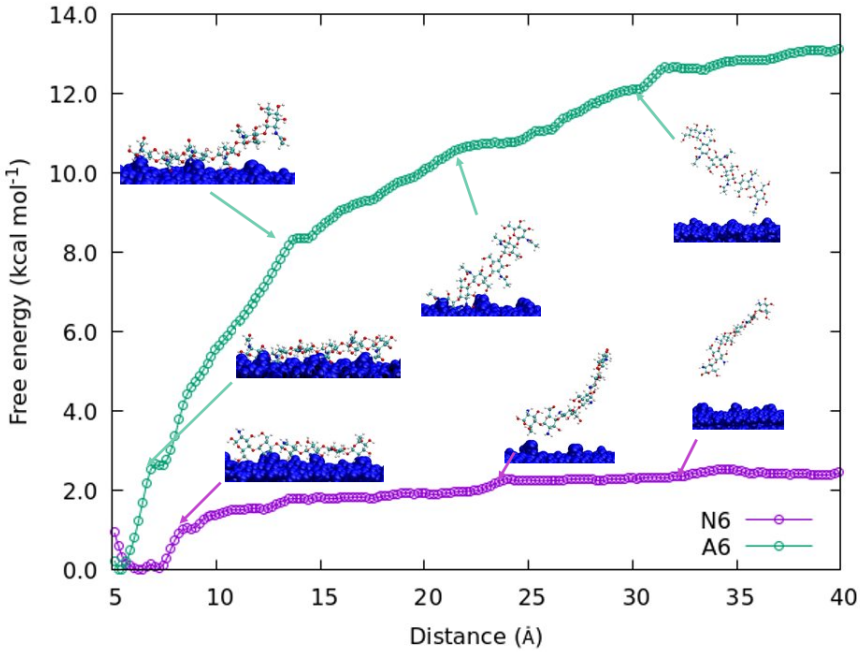

Figure 4.6: Free energy along the distance for A6 (green symbols) and N6 (purple symbols) oligomers.

be expected for similar compounds.

The choice of reaction coordinate is one of the challenging aspects of collective variable enhanced sampling methods. The reaction coordinate must sufficiently describe the system and the studied reaction coordinate using only one dimension (or two in some instances). Here, the projection of the distance along the z-axis between the end C4 atom and the surface of the crystal was chosen. The benefit of this is that it mimics the spontaneously occurring adsorption process. However, a potential downside of this approach is that it is not possible to distinguish between adsorbed and de-adsorbed states for the certain ranges of the reaction coordinate.

The umbrella potential constant, k, and the spacing between the windows are important parameters in US. The US method relies on there being sufficient overlap between the adjacent windows. The standard way to check for the window overlap along the reaction coordinate is to look at the histograms of reaction coordinate values within each window. The histograms for A3 are shown in Fig. 4.7, and include all the US windows. The histograms show very good overlap and have an approximately symmet-

rical appearance. The different histogram heights arise by extending the simulation within some windows as explained below. Simulations with different k values are also discussed below.

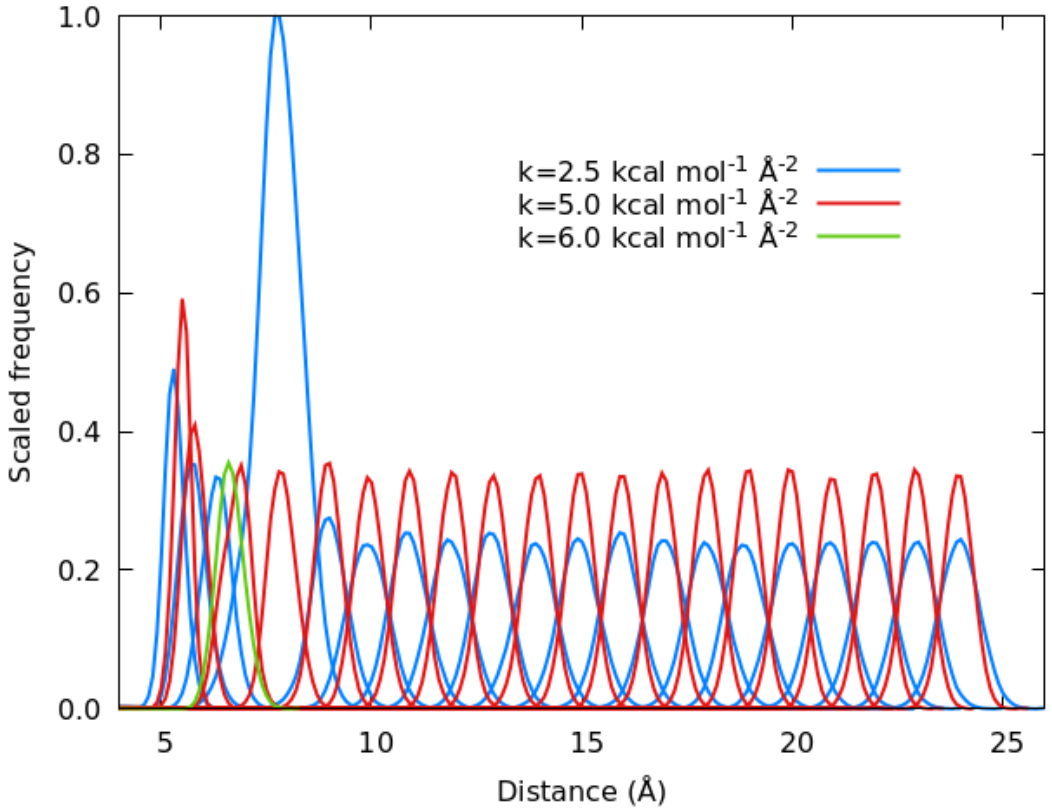

Figure 4.7: Histograms for the A3 oligomer system. Each curve on this graph is a histogram for a particular window. Blue curves correspond to the windows with k=2.5 kcal mol^{-1} Å^{-2}, red k=5.0 kcal mol^{-1} Å^{-2} and green k=6.0 kcal mol^{-1} Å^{-2}.

Histograms can be used to refine the choice of k value. An asymmetrical shape for a particular window can indicate uneven sampling of the reaction coordinate within it. Fig. 4.8 shows the reaction coordinate value during the A3 simulation for the window centred at 8 Å, where a low value k=2.5 kcal mol^{-1} Å^{-2} has been used. There is obvious uneven sampling in the distribution of the values of the distance with time, indicating the presence of an energy barrier (with two energetic minima at ≈7 Å and ≈8 Å) within the window, which the system is slow to cross at this temperature. To improve the sampling, we conducted another full set of US simulations with k=5.0 kcal

mol^{-1} Å^{-2}, and additional individual windows with k=6 kcal mol^{-1} Å^{-2}.

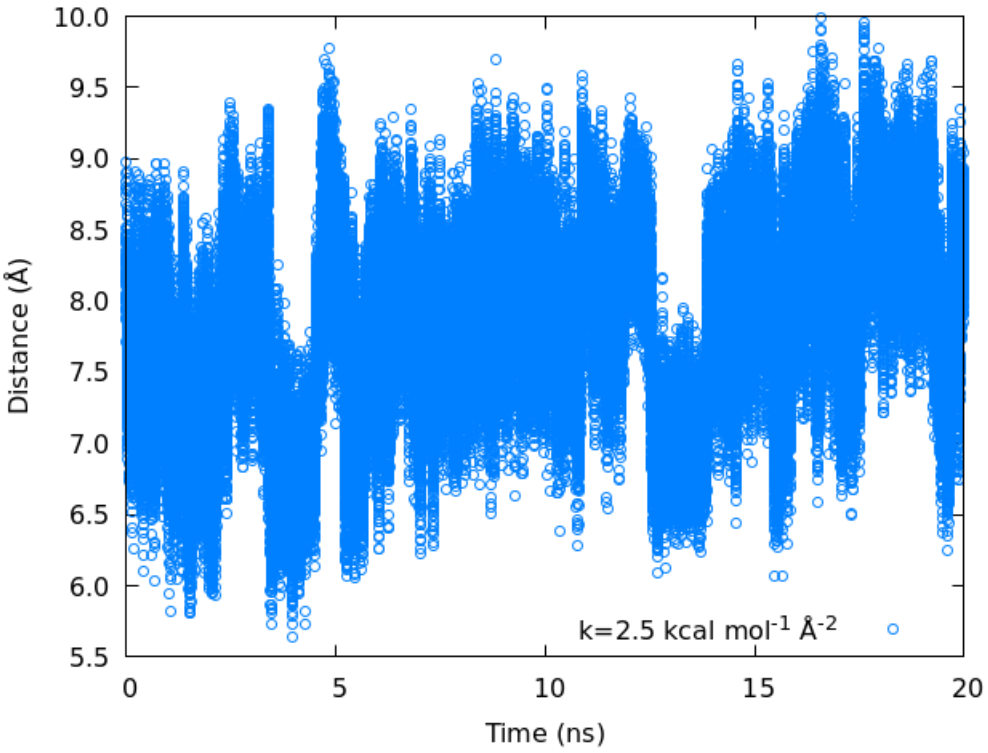

Figure 4.8: The collective variable of the window with the centre 8 Å and k =2.5 kcal mol^{-1} Å^{-2}.

Fig. 4.9 shows the influence of the k values on the final FEC. It can be seen that changing k within the window centred at 7 Å influences the energy values. The shape of the graph remains relatively the same, i.e. positions of the smaller energy barriers, but the height of the curve changes. The reason for this is the tendency for the system to get trapped on one side of the barrier within the window. By using a larger value of k, the height of this barrier is reduced, overcoming this effect. Thus, including the additional simulation with k=6.0 kcal mol^{-1} Å^{-2} increases the reliability of the FEC, as the system can now sufficiently explore the phase-space along the reaction coordinate.

4.2.2 Binding energy of chitin

In order to provide a context for the binding energy calculations, the total potential energy of some key interactions in vacuum was calculated. The cohesive energy of

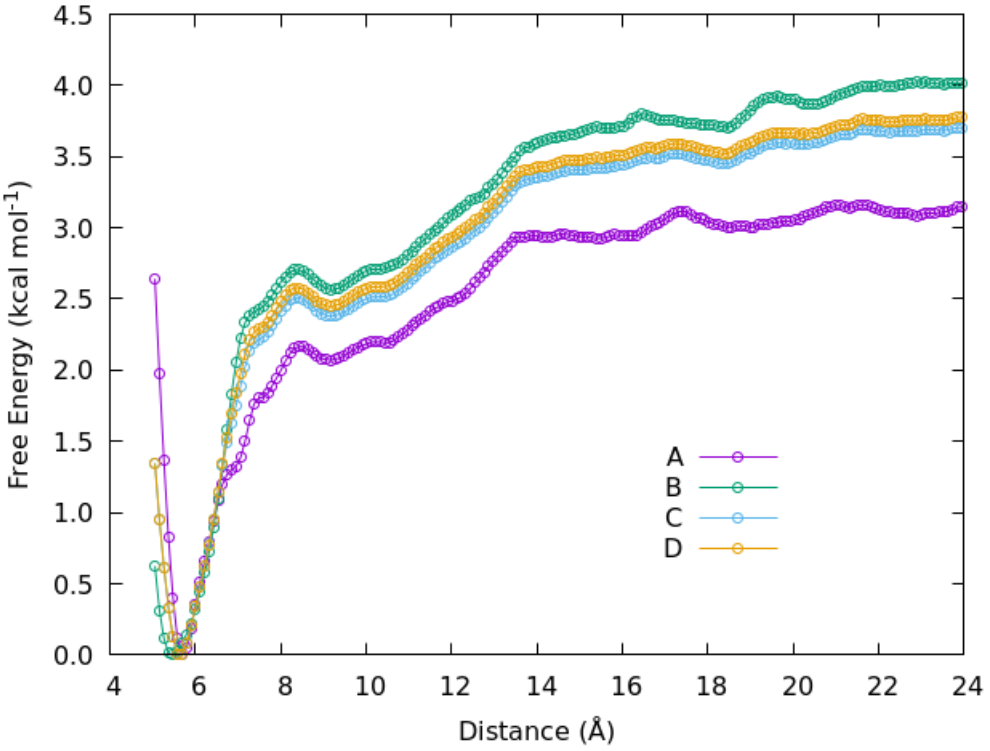

Figure 4.9: The choice of k value influences the final FEC. Curves A and B were obtained from the US sets with k=5 kcal mol^{-1} Å^{-2} and k=2.5 kcal mol^{-1} Å^{-2}. Some windows were extended up to 70ns per window in set B to improve phase-space sampling. Curve C was obtained by combining the two sets (A and B), while curve D was obtained the same as C, but with added window at 7 Å and k=6 kcal mol^{-1} Å^{-2}.

the chitin crystal was calculated to be -19.4 kcal mol^{-1} per monomer; this includes contributions from Van der Waals (vdw) forces and electrostatics. The excess energy due to the surface was calculated to be 10.9 kcal mol^{-1} per monomer (156 mJ m^{-2}). An experimental surface energy of a chitin nanocrystal[114] determined using the contact angle method was reported to be 50 mJ m^{-2}. The energy due to the step was 8.5 kcal mol^{-1} per monomer for the crystal with 33 chains, and the binding energy for the additional chain was -2.34 kcal mol^{-1} per monomer.

The binding energy of the additional chain on the top of the crystal surface supports the results we obtained from the US study. The short oligomer length can explain the lower depth of the energy minima in the FEC; monomers at the oligomer ends bind less effectively to the crystal surface. We expect a stronger binding for longer chains due to

the higher number of hydrogen bonds and dispersion energy. The hydrogen bonds may exhibit the cooperability effect which has been observed in cellulose[115]. This means that the strength of the hydrogen bonds is dependent on the chain length for oligomers up to chain length 7.

Strelcova *et al.*[116] studied parts of chitin nanofibrils in water using MD. Chitin nanofibrils are naturally assembled chitin chains usually consisting of 18-25 chitin chains approximately 570 monomers in length. They calculated the total contribution to binding per single monomer to be -8.7 kcal mol^{-1} using the Molecular Mechanics/Poisson-Boltzman Surface Area (MM/PBSA) post-processing method implemented in Amber for 20-monomer long chains. This value is expected to differ from values calculated in this work as the chitin fibrils differ in structure from the α-chitin crystal due to their smaller and finite size. The nanofibrils typically have a polygonal surface with a large surface area of the crystal exposed to the solvent. Nevertheless, this shows that the results obtained here are in line with these other calculations, given the inherent approximations of the potential model employed herein.

4.2.3 MD

It is expected that chito-oligomers will adsorb to the chitin crystal surface at a pH level higher than 6, at which they are mainly neutral. In the un-biased MD simulations, the neutral oligomer adsorbed on the surface did not spontaneously desorb into the solution. Furthermore, the behaviour of a charged chitosan oligomer was explored, which we obtained by protonating the amino groups of the N6 oligomer. This classical MD simulation was performed to verify that the chitosan oligomer constructed here would desorb from the crystal into the solution at a pH value below 6; indeed the charged chitosan oligomer desorbs from the chitin crystal surface. The other oligomers showed different mobility on the crystal surface, but remained adsorbed for the duration of the simulations.

The adsorption process for A6 oligomer is shown in more detail in Fig. 4.10. Fig. 4.10A shows the z coordinate of the A6 COM. The oligomer approaches the (-1 0 0) surface of the α-chNC at around 40 ns and forms temporary h-bonds with the

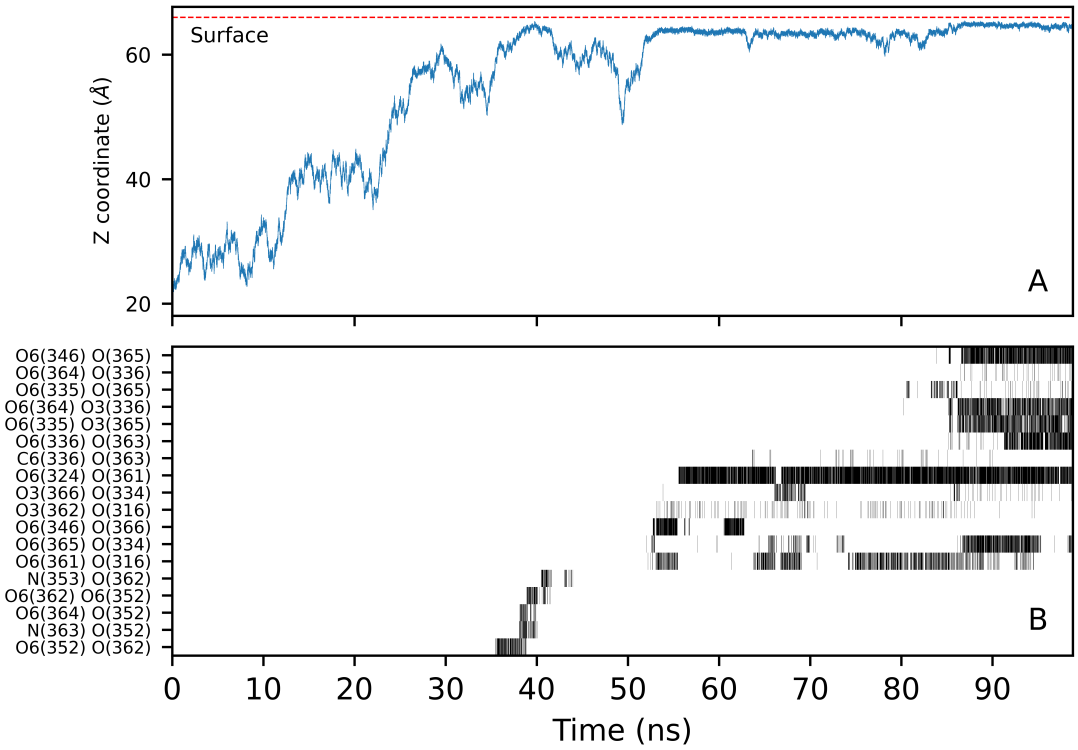

Figure 4.10: The simulation of A6 adsorption to α-chNC surface. The z coordinate of the COM of A6 oligomer (A) and hydrogen bonding analysis (B), which includes only those hydrogen bonds significantly contributing to the adsorption process. The h-bonds are shown in donor - acceptor order, with number in bracket signifying the residue number.

surface (Fig. 4.10B). Between ≈45 and 55 ns the oligomer briefly moves away from the surface, before adsorbing again at ≈55 ns. More hydrogen bonds are formed and at ≈85 ns and at this time oligomer becomes fully adsorbed to the crystal surface. The A6 simulation was extended to 100 ns, during which the oligomer remained adsorbed. This indicates strong adsorption, where the oligomer remains adsorbed without external forces introduced in the system, which is consistent with the US results.

4.2.4 SMD

In constant velocity SMD, the spring force varies during the simulation, as shown in Fig. 4.11(a) for the A3 oligomer SMD. The drops in force and sharp increases in the spring extension (Fig. 4.11(b)) can be correlated with the breaking of hydrogen bonds,

and with the change in the glycosidic bond conformation as seen in Table 4.1. The intra-chain hydrogen bonds arise as a consequence of steric effects (exoanomeric effect) and stabilise the 2_1 chain configuration. After the breaking of the hydrogen bonds between the crystal and the oligomer, conformational changes of the oligomer occur. This explains the changes in force observed after the oligomer has been completely pulled from the crystal.

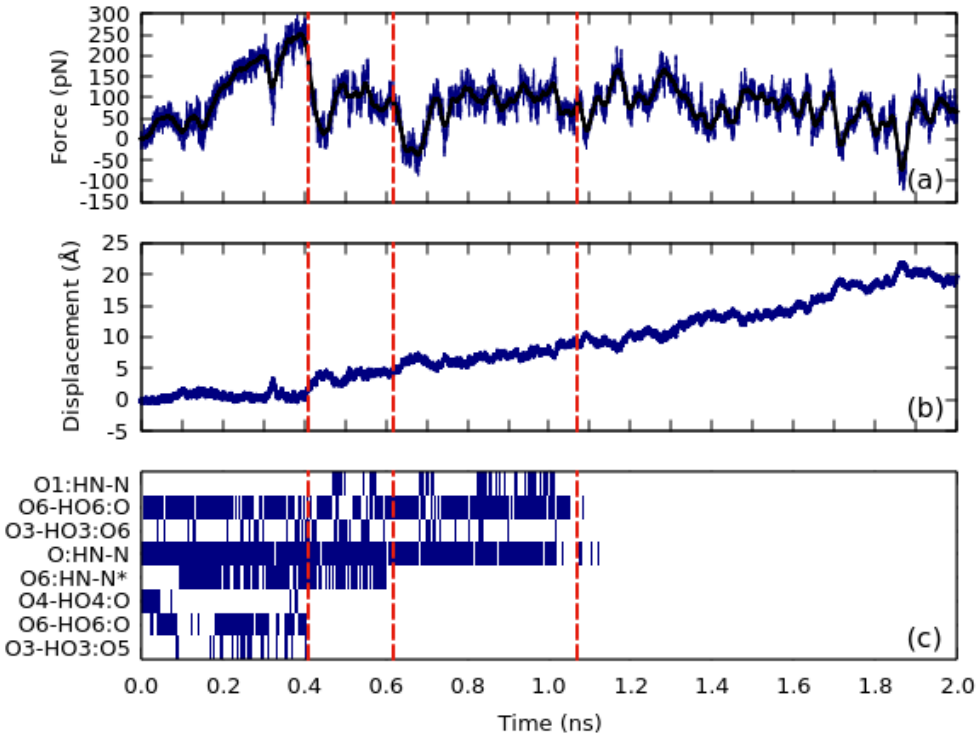

Figure 4.11: The force-time (a) and displacement-time (b) graphs for the A3 oligomer pulled from the surface of the crystal with constant velocity. (c) shows the occupancy of hydrogen bonds during the simulation. The times of interest are marked with red vertical lines.

The O6-HO6-O and O:HN-N bonds contributed more significantly towards the oligomer-crystal binding than the rest of the hydrogen bonds, as seen from their high occupancies prior to their breaking in Fig. 4.11(c). Interestingly, one bond-breaking event observed during the SMD pulling at 0.62 ns was breaking the interchain hydrogen bond O6-HO6:N*, where * refers to the intrachain hydrogen bond.

Table 4.1: SMD A3 and A6 energies and hydrogen bonds broken during the simulation, where * indicates intra-chain hydrogen bond.

Time (ns)	dE (kcal mol^{-1})	H-bonds
A3		
0.41	6.5	O3-HO3:O5, O6-HO6:O, O4-HO4:O
0.62	0.7	O6-HN-N*
1.10	1.7	O6-HO6:O
A6		
0.45	3.0	O:HN1-N
1.10	4.9	O:HN1-N $\times$ 2
1.50	2.2	O:HN1-N (O6:HO6-O6)
2.50	2.2	O:HN1-N $\times$ 2

The hydrogen bond analysis also suggests that the intra-chain hydrogen bonds are mostly preserved during the pulling, indicating that the oligomer's 2-fold linear structure is mostly conserved. Similar results were observed for the rest of the A6 oligomer as shown in Table. 4.1.

4.2.5 Readsorption

Following the SMD pulling of the A3 and A6 oligomers from the crystal surface, unbiased MD simulations were performed to see if the oligomers spontaneously readsorb. Despite the shape of the free energy landscapes in Fig. 4.5 and Fig. 4.6, this adsorption is expected to be slow (on the MD timescale of 100 ns) due to kinetic effects and the orientational requirements for successful adsorption. The adsorption events are observed after 65 ns and 70 ns for the A3 and A6 oligomers, respectively.

The readsorption process is shown in more detail for A3 oligomer in Fig 4.12. The oligomer approaches surface for the first time at $\approx$ 10 ns and forms several short-lived hydrogen bonds. During this time the oligomer does not fully adsorb, but instead diffuses back into the bulk solution. The next approach occurs at $\approx$ 55 ns, when the oligomer starts forming longer lasting hydrogen bonds with the surface. Finally, at around 65 ns the oligomer lies completely flat on the surface. This is shown by the increased number of hydrogen bonds forming around that time.

The A6 simulation was extended to 100 ns, during which the oligomer remained ad-

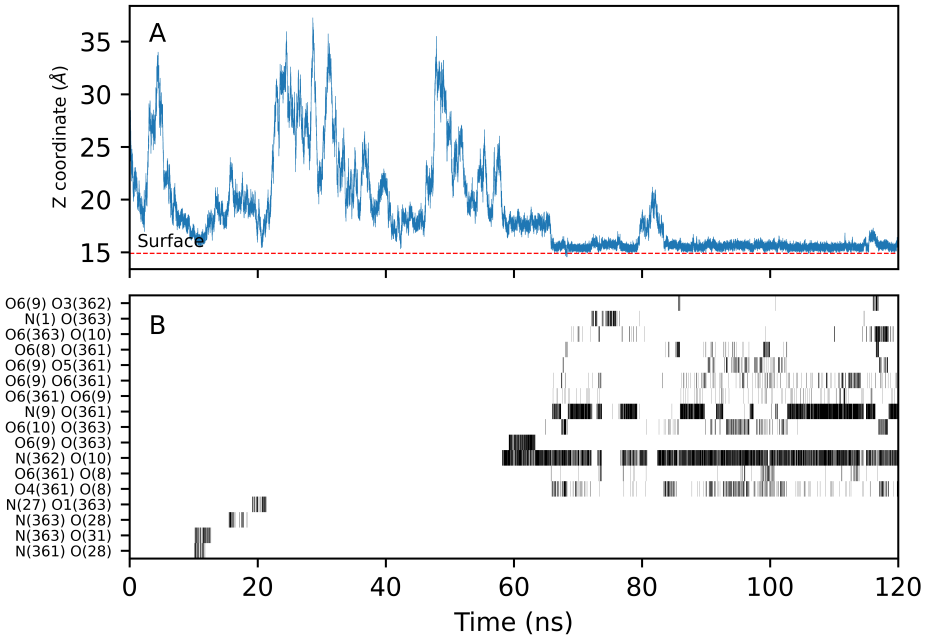

Figure 4.12: The simulation of A3 adsorption to α-chNC surface following the SMD. The z coordinate of the COM of A6 oligomer (A) and hydrogen bonding analysis (B), which includes only significantly hydrogen bonds contributing to the adsorption process. The h-bonds are shown in donor - acceptor order, with number in bracket signifying the residue number.

sorbed. This indicates strong adsorption, where the oligomer remains adsorbed without external forces introduced in the system, which is consistent with US results.

The potential energy of the simulation was monitored to see how it changes upon the oligomer adsorption, to again obtain an indication of the magnitude of the adsorption free energy[117]. The potential energy values rapidly oscillate around their mean value. The time average of the different parts of the simulations was calculated to evaluate the change in the potential energy of the whole system due to oligomer adsorption. The difference in potential energy in the part of the simulation where the A6 oligomer is adsorbed and the part where it is free in solution is -14.2±1.3 kcal mol^{-1} or -2.4±0.2 kcal mol^{-1} per monomer, consistent with the adsorption energy values of -12.2 kcal mol^{-1}. The time-averaged potential energy difference for A3 oligomer is -9.8±1.3 kcal mol^{-1}, or -3.3±0.4 kcal mol^{-1} per monomer. Again this adsorption value supports that

from the FEC calculations.

The A6 oligomer is adsorbed in the b direction across the crystal surface, which is not the most energetically favourable. This finding is in agreement with a study by Yudin *et al.*[118], who used MD alongside experimental methods to assess the orientation of a chitosan chain on the chitin crystal surface. Although the details of the MD methodology were unclear, the experimental and theoretical results indicated the strongest binding when the chitosan chain had a parallel or antiparallel orientation along the crystal surface, lining up with the chains on the crystal. This parallel or antiparallel orientation (in the c direction) enables the formation of the highest number of hydrogen bonds. Such adsorption is seen for the A3 oligomer.

4.3 Conclusion

MD simulations were used to study the binding energy of chito-oligomers with a model α-chitin surface. The free energy landscapes of the chitin trimer, and chitin and chitosan hexamers adsorbing to the crystal surface using US were calculated. The oligomer-crystal binding energy was -12.5 kcal mol^{-1} and -2 kcal mol^{-1} for chitin and chitosan 6-monomer-long oligomer chains respectively. To validate free energy calculations, several additional calculations were performed. First, the binding energy of chitin crystal and excess surface energy in a vacuum were calculated. Then, using SMD pulling, the strength of the chitin oligomer binding to the chitin crystal surface and the breaking of the relevant hydrogen bonds was evaluated. The SMD pulling disrupted the intra-chain bonding and caused conformational changes in the oligomer. This explains the slow adsorption process observed during classic MD simulations. These results align with similar studies carried out for cellulose and chitin nanofibrils[116, 113].

The calculations performed here help shed light on the dynamics of chito-oligomers and their adsorption to the chitin crystal. The slow dynamics of the crystal-oligomer interactions mean that it is challenging to study the self-assembly of chitin nanofibrils and crystals using classical MD. The FECs can be used to further the understanding of these processes. The FECs can also be helpful when constructing and validating coarse-grained models for chitin and chitosan, which can span into the nanofibril length scale

and microsecond timescale. Furthermore, understanding the material properties at the nanoscale is very valuable when designing novel materials and processes, such as composite chitin thin films and enzymes engineered for the production of chitosan.

Chapter 5

Chitosan adsorption at a silica surface

5.1 Introduction

Chitosan–silica composites have been studied in various forms, including silica-chitosan hydrogels for heavy-metal absorption[119], and chitosan-coated silica nanoparticles for targeted chemotherapy drug delivery[120].

Understanding the interface between the silica surface and chitosan, and the mechanism of chitosan adsorption, is crucial for ensuring particle stability and fine-tuning the properties such as particle charge, size and bioactivity. Several studies have used experimental methods, for example quartz crystal microbalance and UV-vis spectra, to explore the mechanism of chitosan adsorption from solution onto silica surfaces[121, 122]. While these studies provide useful information such as chitosan adsorption density and chitosan layer thickness, these experimental methods cannot provide an atomistic level of detail of the adsorption process.

Chapter aims:

- To complement previous experimental studies by using MD simulations.
- To provide insight and understanding of the dynamics of chitosan adsorption at

the molecular level, that can be used to further improve and optimise chitosan-coated silica nanoparticles tailored to specific applications.

- To calculate the binding free energy of chitosan adsorption to silica surface using umbrella sampling.

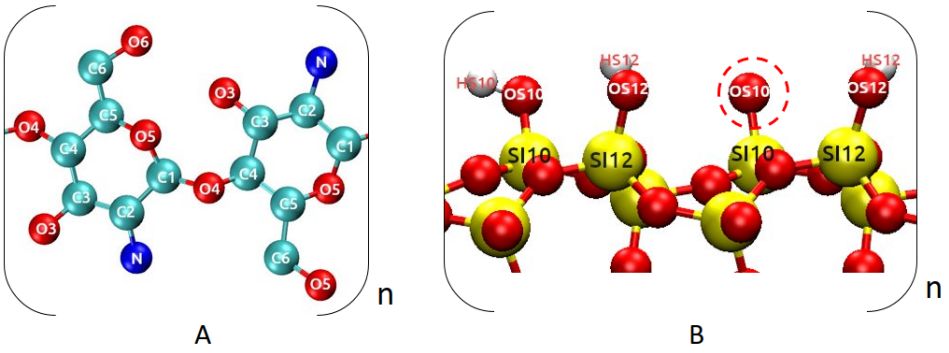

Figure 5.1: Schematic diagram for chitosan (A) and the silica surface (B) where atoms are labelled for reference. The dashed red circle in (B) highlights de-protonated surface oxygen. The colours are assigned according to the atomic species: cyan - carbon, red - oxygen, blue - nitrogen, yellow - silicon and white - Hydrogen. Hydrogen atoms in (A) are omitted for clarity.

The silica-water interface is characterised by the presence of the electric-double layer (EDL). The EDL consists of ions which screen silica's negatively charged surface. The extent of the EDL can be approximated by the Debye length, which depends on the concentration of the ions in the bulk and the temperature[109].

Standard MD simulations were used to explore the adsorption of chitosan oligomers from aqueous solution to a model silica nanoparticle (Si-NP) (2 0 -2) surface, as illustrated in Fig 5.1B. Oligomer-by-oligomer adsorption was studied as well as simultaneous multi-oligomer adsorption. SMD and US were used to calculate the free energy of adsorption of chitosan to the Si-NP surface and to determine the mechanism of adsorption.

These simulations can be used both to aid interpretation of experiments and, in the future, for design optimisation for bespoke applications of the functionalised nanoparticles.

5.2 Methods

5.2.1 System setup and general simulation protocol

A silica slab ($7.49 \times 7.44 \times 2.6$ nm^3) with periodicity in the $x-y$ plane was constructed using the CHARMM-GUI [100] nanomaterial modeller[101] with an α-cristobalite structure and a surface silanol (Si-OH) group concentration of 4.7 nm^{-2}. The slab exposes two chemically identical surfaces to the solution (Surface I and II) that are able to adsorb oligomers. Chitosan oligomers were constructed using an in-house Python code. The silanol deprotonation level was 6.66 % (0.31 nm^{-2}) and the chitosan was fully protonated to mimic pH ≈ 5. Interface [84] and Charmm36[123] force fields were used to model the silica and chitosan[124] respectively. The structures were combined using VMD[125] to obtain the desired initial system configuration. The system was then solvated with TIP3P[126] water, and Na^+ (or Ca^{2+}) and Cl^- ions were added to neutralise the system and set the bulk solution concentration to 0.15 mol L^{-1}.

All the simulations were performed using Gromacs[127] 2022.2 software, with the inputs prepared using the ParmEd code[128]. The analysis was performed using Gromacs built-in tools, VMD and MDAnalysis[129], while the plots were made using Gnuplot[130].

The general simulation protocol was as follows: The system was initially minimised for 5000 steps using the steepest descent method, with non-solvent molecules restrained using harmonic potentials. The water molecules and ions were then equilibrated for 0.5 ns using the Berendsen thermostat at 300 K and the Parinello-Rahman barostat with anisotropic pressure coupling at 1.0 bar. After initial equilibration, the system was simulated using the Nose-Hoover thermostat at 300 K, the Parinello-Rahman barostat at 1 bar with anisotropic pressure coupling, and 2 fs timestep integration. The electrostatics were calculated using PME and a 1.2 nm cutoff was used for vdw calculations. The LINCS constraints algorithm was used to restrain hydrogen bonds. Periodic Boundary Conditions (PBC) are used, so that the silica slab is infinite in the x- and y-directions, with the solution sandwiched between silica slabs.

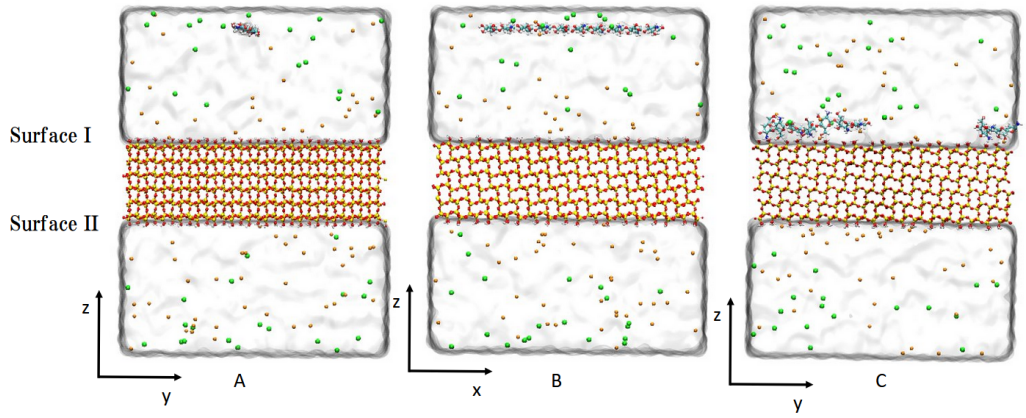

Figure 5.2: A typical system is shown at the beginning (A and B) and at the end (C) of the simulation. The system is periodic in all three dimensions. The colours are assigned according to the atomic species: cyan - carbon, red - oxygen, blue - nitrogen, yellow - silicon, white - hydrogen, green - chloride ions, orange - sodium ions.

5.2.2 Chitosan adsorption

Table 5.1: Summary of the standard MD simulation systems.

Chitosan	Silica slab no.	N(water)	N(Na^+)	N(Cl^-)	N(Ca^{2+})
6-mer	1	12813	66	36	0
6-mer	2	13069	67	37	0
6-mer	3	13084	67	37	0
10-mer	1	14833	68	42	0
10-mer	2	13759	65	39	0
10-mer	3	13852	65	39	0
8 × 10-mer	1	21529	61	105	0
8 × 10-mer	1	21555	0	104	30
-	1	22208	141	105	0

A number of systems were created for standard MD simulations. These are described below (with the quantitative component summary provided in Table. 5.1) and a representative system is shown in Fig. 5.2. Here, a single chitosan 6-mer (0.9 kDa) or 10-mer (1.6 kDa) was placed 3 nm above the silica surface, and the system was further simulated as described in the afore-mentioned general protocol for 200 ns. The entire protocol was repeated twice, with newly generated silica slabs to ensure random silanol deprotonation sites. All the production trajectories done in triplicate were analysed

and they gave statistically similar results, therefore one representative trajectory obtained for each system was used as an exemplar and described in detail in the results section.

To further study the loading capacity, which is the amount of chitosan able to adsorb to the silica surface, simulations with multiple chitosan oligomers present in the system were conducted. This was done using two separate methodologies: i) inserting oligomers into the system one by one and ii) adding all oligomers simultaneously at the beginning.

In the first methodology, oligomers were added one-by-one to the system. The system was initially set up in the same way as for the single-oligomer adsorption simulations. However, in this case, the simulation was stopped after 100 ns. Following this, the water and ions were removed and an additional single oligomer was placed 3 nm above the surface, bringing the total number of chitosan chains in the system to two. The system was then resolvated and sodium chloride was added as described in the main simulation protocol. The production run was again 100 ns. The same process as before was repeated twice more, bringing the total number of chitosan oligomers in the system to four. This system was then simulated for 800 ns.

In the second methodology eight 10-mer chitosan oligomers were placed 3 nm above the silica surface in a 4×2 arrangement with 1.5 nm spacing between the oligomers. The system was then prepared as described in the general protocol. An additional system was created in which Ca^{2+} and Cl^{-} ions were added to neutralise the system and bring the bulk solution concentration to 0.15 $mol\ L^{-1}$ to study the effects of the cation valency on the adsorption process. Lastly, a system of comparable size was created which contained only a solvated silica slab, neutralised with NaCl to 0.15 mol L^{-1} concentration. This system served as a control for the density profile calculations. All three systems were equilibrated using the main simulation protocol as above with a production run of 700 ns for each. In total, 9 different systems were simulated using standard MD totalling 3.4 μs.

5.2.3 Adsorption free energy

SMD and US were performed using both a single 6-mer and a single 10-mer chitosan oligomer with constant 1 nm ns^{-1} pulling velocity and harmonic constant k = 100 kcal mol^{-1} nm^{-2}. SMD was performed on the systems with a single chitosan oligomer already adsorbed to the surface (after 200 ns of standard MD simulation time). The C4 atom (see Fig. 5.1) in the first monomer of the chitosan chain was pulled in the +z direction (normal to the silica surface) and later used to define the distance collective variable in the US simulations.

The SMD trajectory was analysed and used to obtain snapshots for the US windows. In total 53 and 72 windows were utilised with window spacing 0.1 nm for the 6-mer and 10-mer systems respectively (see umbrella histograms Fig. 5.8). The harmonic constant k = 250 kcal mol^{-1} nm^{-2} was used. Each window was simulated for at least 40 ns, while the simulation time for any windows with uneven sampling was extended up to 80 ns. The total simulation times per umbrella sampling set were 1.34 μs and 3.66 μs for the 6-mer and 10-mer system respectively. The collective variable was defined as the distance between the C4 atom used in the SMD and the silica surface, with the surface defined as the arithmetic mean of the z positions of the silanol oxygen atoms. The free energy curves were calculated using the Gromacs built-in function which employs the WHAM[131]. The US results were carefully analysed to assess the fidelity of the calculations.

5.2.4 Analysis

Hydrogen bond analysis was performed using VMD's "measure hbonds" command with cutoffs 0.35 nm and 30° as pre-defined in VMD. Partial densities were calculated using the gmx density command using 140 slices. Unless stated otherwise, in the time-averaged calculations the initial 20 ns of the simulation were omitted so that a steady state had been reached.

5.3 Results and Discussion

5.3.1 Single chain adsorption dynamics

The simulations of a single chitosan oligomer were performed in triplicate as described in the methods section. The trajectories exhibit similar behaviour, so we describe one 10-mer trajectory in detail as representative. The chitosan oligomer readily approached the silica surface within 1 ns, initially with an orthogonal orientation to the surface. Through the next 10 ns of the simulation, the oligomer adopted an orientation parallel to the silica surface. Once adsorbed, the oligomer stayed on the surface for tens of nanoseconds, before partially desorbing and moving parallel to the surface. Thus, the oligomer remained relatively mobile on the silica surface but did not desorb back into the bulk solution. The z-component of the centre of mass (COM) of the 10-mer oligomers for all three replicas are shown in Fig. 5.3.

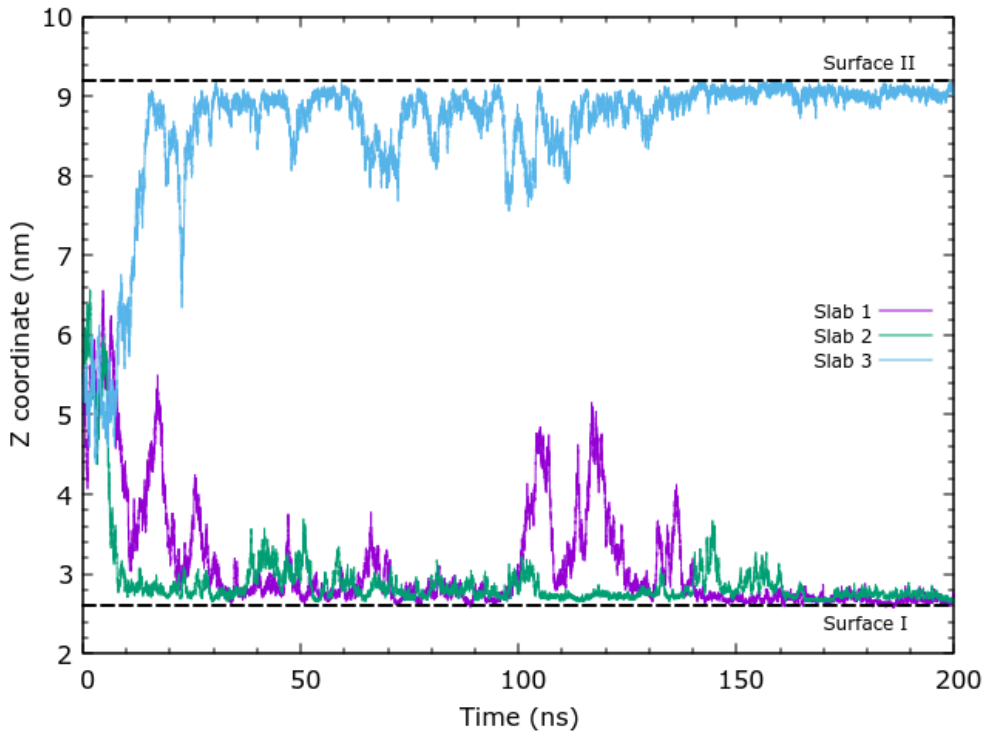

Figure 5.3: z component of chitosan 10-mer COM without PBC wrapping. Three independent simulations (triplicates) are reported (labelled slab 1,2 or 3).

As described in Methods, the initial structure of the triplicates differs in the random

distribution of the deprotonated silanol groups on the silica slab surface. One constraint of the MD simulations is the inability to correctly model the protonation/deprotonation process of the silanol groups. Nevertheless, this is an equilibrium process, so on average the system will have the same number of protonated and deprotonated groups, but they will have different distributions. Simulations with different random de-protonation patterns enable us to see if the distribution of these sites makes a statistical difference to the adsorption process. In the COM plots shown in Fig. 5.3, due to the use of unwrapped coordinates, surface I is at ≈ 3 nm and surface II at ≈ 9 nm in the figure. Chitosan is able to adsorb to either surface I or surface II as they are chemically the same. The 6-mer chitosan oligomers exhibit similar adsorption dynamics with the z component of the COM shown in the Fig 5.4. Complete desorption into the solution is occasionally seen in the 6-mer adsorption simulation, with the oligomer subsequently re-adsorbing to the surface.

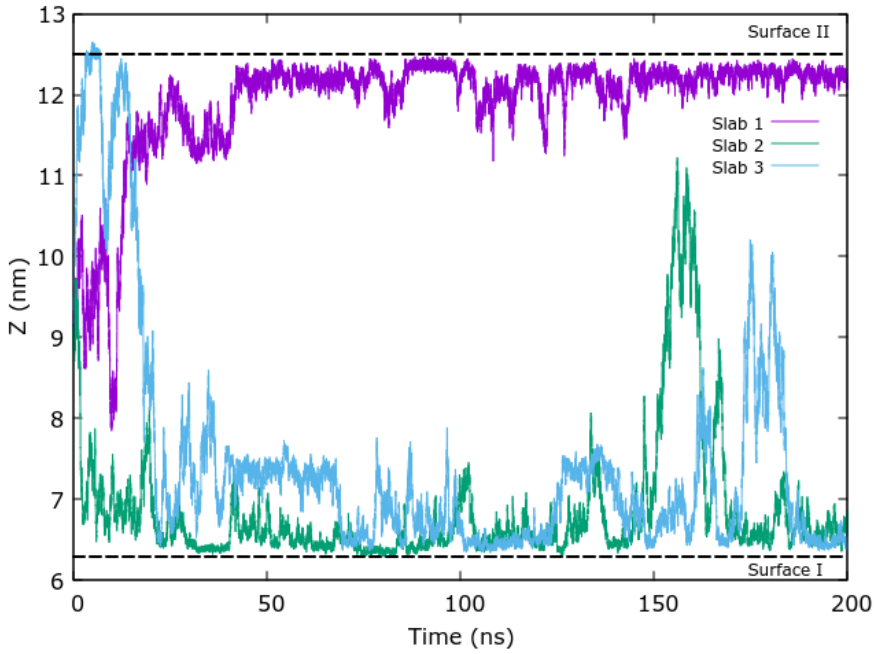

Figure 5.4: z component of chitosan 6-mer COM without PBC wrapping. Three independent simulations (triplicates) are reported (labelled slab 1,2 or 3).

It is widely assumed that the adsorption process is driven by electrostatic interactions. The silica surface is negatively charged at pH 5, with deprotonated silanol groups

($Si–O^-$). At the same pH chitosan's amino groups are protonated ($–NH_3^+$) making chitosan act as a weak polycationic electrolyte. However, hydrogen bonds are also important for adsorption, as shown here. While it is not possible to distinguish individual energy contributions, hydrogen bonds arising from the electrostatic and Lennard-Jones terms can be monitored. Fig. 5.5 shows the hydrogen bonds between the chitosan 10-mer and silica slab during the simulation. The hydrogen bonds tend to break and form during the adsorption process. The highest number of simultaneous hydrogen bonds occurs after 150 ns of simulation, where the COM z-coordinate plateaus (Fig. 5.3). The chitosan atoms that contribute the most to hydrogen bonding are O6 and N atoms, which are on opposite sides of the carbohydrate ring (see Fig. 5.1). Moreover, due to chitosan's helical conformation, which is typical of 1–4 linked polysaccharides in aqueous solution, two neighbouring O6 or N atoms never contribute to hydrogen binding at the same time.

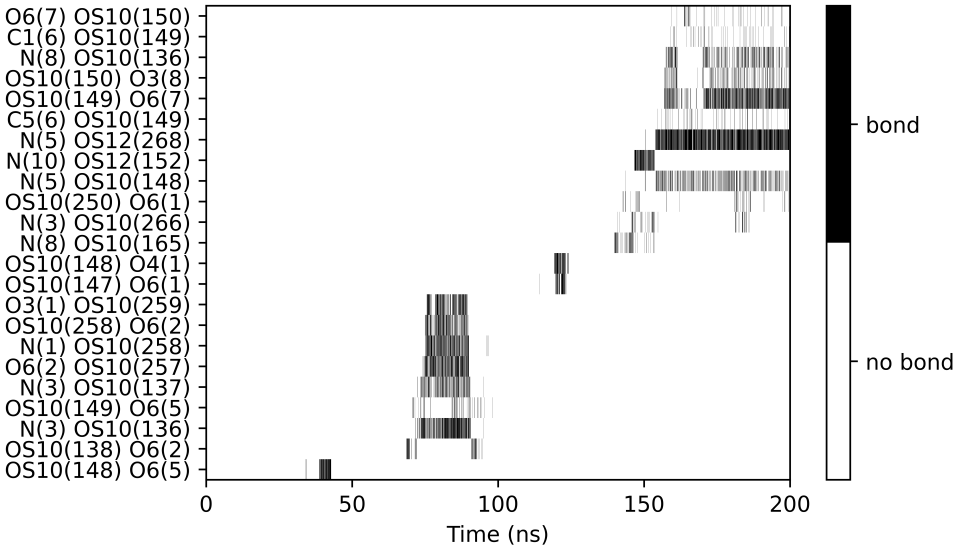

Figure 5.5: Chitosan - silica hydrogen bond formation and breaking during the adsorption process. The pairs are listed in donor-acceptor order. The atom names are as illustrated in Figure. 5.1 with the number in the bracket referring to the residue number.

5.3.2 Chitosan desorption from the surface using SMD

SMD is used to qualitatively analyse hydrogen bond making and breaking between the chitosan and silica surfaces during forced desoprtion. This also provides the initial structures for the US windows. Figure 5.6 shows the analysis for the 10-mer chitosan SMD simulation, where the adsorbed oligomer is pulled directly up from the silica surface in the normal direction. The force curve shown in Fig. 5.6A shows large variations in the force during the initial stage (0-2 ns) of the pulling. When the chain is entirely pulled from the surface at time $\approx$ 4.9 ns, a large force drop occurs. The corresponding displacement curve of the pulled C4 atom is shown in Fig 5.6B.

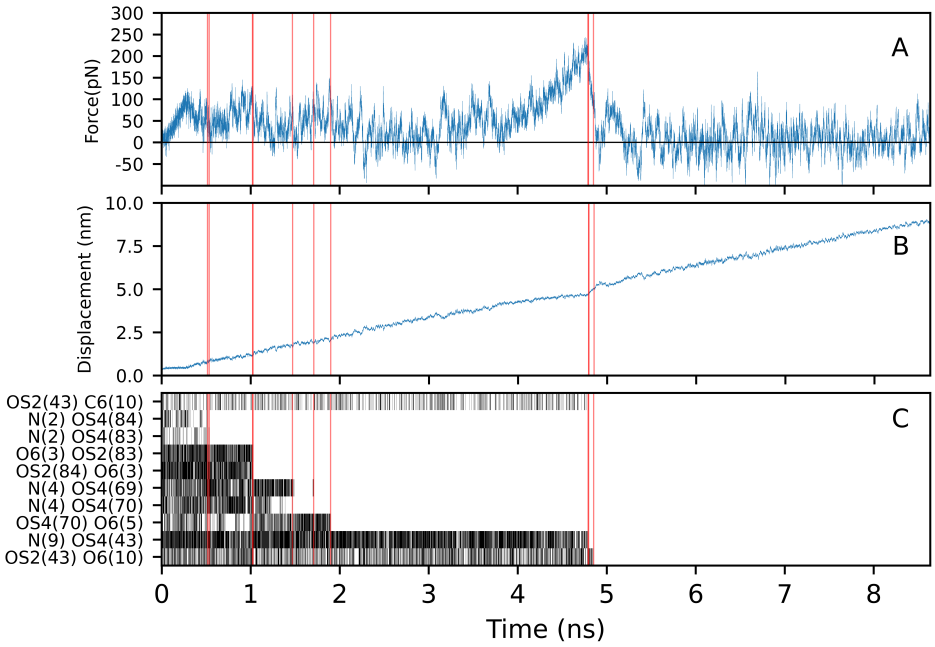

Figure 5.6: SMD analysis for a 10-mer chitosan oligomer pulled from the silica surface showing (A) the force and (B) the displacement curves. (C) shows when key hydrogen bonds exist, with red vertical lines indicating the time of bond breaking. The pairs are listed in donor-acceptor order. The atom names are as illustrated in Figure 5.1 with the number in the bracket referring to the residue number

Fig. 5.6C shows the breaking of the key hydrogen bonds between the chitosan chain and silica surface. These events are indicated with vertical red lines and correspond

to the force drops observed in Fig. 5.6A. The main chitosan atoms responsible for chitosan-to-silica hydrogen bonds are the nitrogen of the amino group and the O6 atom (see Fig. 5.1). The nitrogens from monomers 2, 4 and 9 and O6 atoms from monomers 3, 5 and 10 are the main contributors. The silanol oxygens (OS2, OS4) can act both as donors or acceptors in hydrogen bonding due to being part of the silanol functional group (Si-OH), with OS4(43) oxygen being the only deprotonated oxygen relevant for the hydrogen bonding. Thus, this atom can only be an acceptor. This hydrogen bonding pattern is consistent with previous observations in the spontaneous adsorption section. The harmonic constant (k) value used in the simulations here is too small for the stiff spring approximation to apply, and thus free energy is not calculated directly from the SMD trajectories[132], but by US instead.

5.3.3 Free energy of adsorption

The calculated free energy profiles for the 6-mer and 10-mer chitosan oligomer adsorption processes are shown in Fig. 5.7. The distance indicated in the energy curves graph is the reaction coordinate used in the US and is equal to the distance between the C4 atom of the first monomer and the silica surface. The other parts of the chain are not restrained by the harmonic potential and are thus allowed to move freely.

The energy minimum occurs at 0.4 nm distance, which corresponds to the adsorbed state. After the minimum, both curves are relatively smooth indicating no significant intermediate energy barriers to the adsorption process. Here, it is important to consider the length of each chain when evaluating the free energy curves. The end-to-end distances are 5.20 nm and 3.0 nm for completely straight 10-mer and 6-mer oligomers, respectively. Hence, the chitosan oligomer is fully desorbed only at a distance greater than the end-to-end chain length added to the thickness of the EDL, which can be approximated by the 0.8 nm Debye length for 0.15 mol L^{-1} NaCl concentration. Thus, by simple addition we expect the free energy curves to reach a plateau around 6.0 nm and 3.8 nm respectively for the 10-mer and 6-mer, consistent with Fig. 5.7.

The free energy of adsorption of chitosan oligomers to the silica surface can be calculated as the difference between the adsorbed state and the solvated state, which is

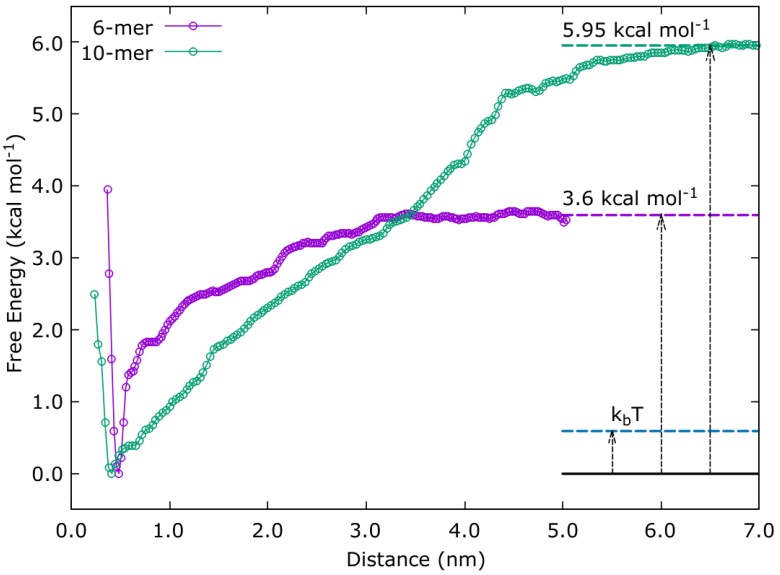

Figure 5.7: Free energy curve for the 6-mer and 10-mer adsorption.

characterised by the free energy curve reaching a constant value. The free energy of adsorption has thus been calculated to be 3.60±0.46 kcal mol^{-1} and 5.95±0.25 kcal mol^{-1} for the 6-mer and 10-mer, respectively. For both oligomers, this equates to approximately 0.6 kcal mol^{-1} per monomer. Thus, it might be concluded that the chitosan with higher molecular weight would exhibit stronger adsorption to the surface as has been experimentally shown by Matusiak *et al.*[122] who measured the adsorption of chitosan with three different molecular weights on siNPs using the ninhydrin colorimetric method[133]. Furthermore, as illustrated in Figure 5.7, $k_BT \approx 0.6$ kcal mol^{-1} at $T = 300$ K, which explains why individual monomers repeatedly adsorb and desorb from the silica surface during the standard MD simulations, giving the adsorbed oligomer mobility without complete desorption which can be seen from the Figure 5.3.

The US method cannot be directly evaluated for convergence, so extensive indirect methods are employed. Firstly, the overlap of neighbouring histograms, which are presented in the Fig. 5.8, are evaluated to ensure that they show good overlap for all the windows. Another, often overlooked, property of the US histograms is the shape of each "umbrella" which should have a fairly symmetrical shape, indicating adequate sampling in the window. In cases where very asymmetrical umbrellas were observed,

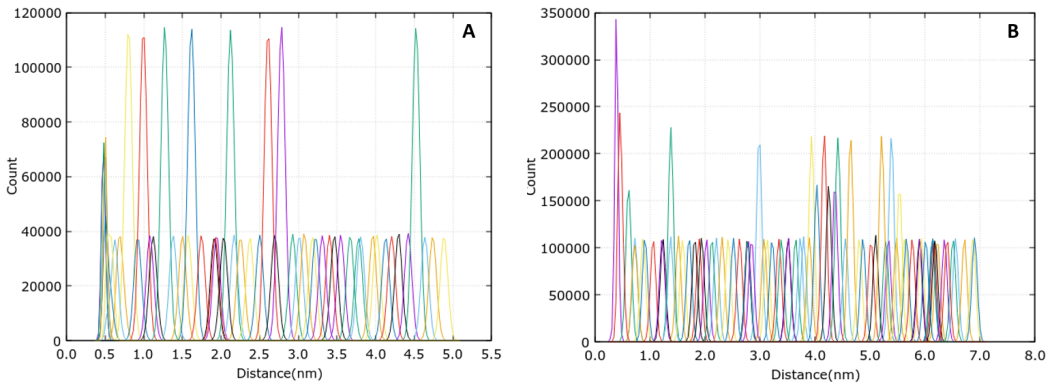

Figure 5.8: Histograms for 6-mer (A) and 10-mer (B) US sets.

the simulation were extended until a more symmetrical shape was achieved to ensure adequate sampling. Additionally, the distance between the end C1 atom (at the opposite side of the oligomer to the C4 atom) and the silica surface was tracked to observe sampling of the phase space by the so-called orthogonal reaction coordinate, which is also responsible for US convergence. Fig. 5.9 shows that the two distances display good overlap along both x and y directions, which is indicative of good convergence of the calculated free energy profile.

Figure 5.9 also enables the visualisation of the adsorption dynamics of the chitosan oligomer. Each vertical section of a particular colour in the graph represents a single window (colours are repeated due to the limited number of colours in the palette). The Distance C4 shown on the x-axis is the collective variable used for umbrella sampling. The Distance C1 shown on the y-axis represents the unconstrained end of the chitosan chain, which is allowed to move freely. This type of graph enables us to see two-dimensional space sampling and check for overlap between the windows along both C4 and C1 distances.

As the C4 distance is increased, the C1 distance remains small until the C4 distance reaches 3 nm, indicating that chitosan remains partially adsorbed for those windows. For C4 distances between 3 and 4 nm chitosan can either remain partially adsorbed or fully desorb, which depends on whether the initial configuration for the particular window has an energetically favourable position towards adsorption. Multiple windows

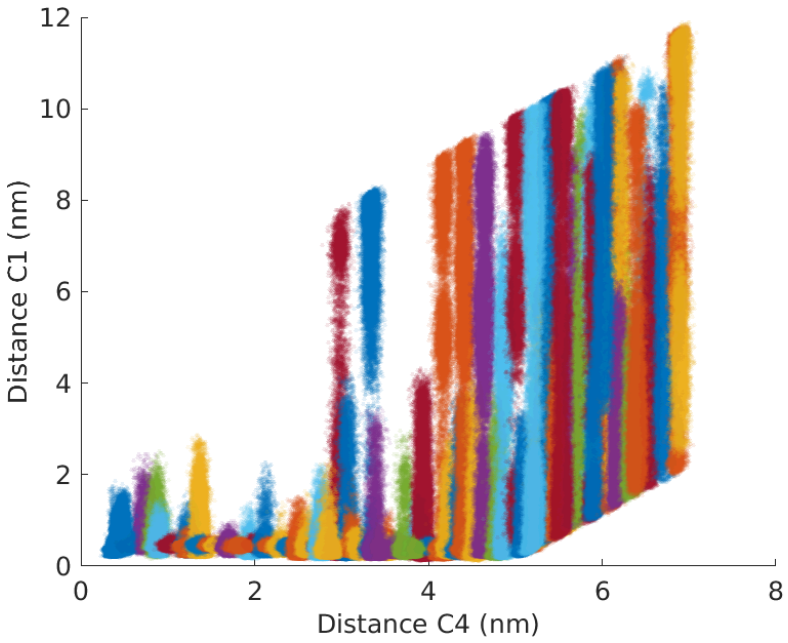

Figure 5.9: Constrained reaction coordinate (Distance C4) and unconstrained orthogonal (Distance C1) correlation plot for 10-mer US set.

for this range of C4 distances ensure good overlap and thus sufficient sampling of the conformational space. For C4 distances beyond 4 nm, the oligomer can fully desorb to explore the full conformational space.

5.3.4 Multiple chain adsorption dynamics

To determine the maximum adsorption capacity of chitosan to the silica surface, systems with multiple 10-mer chitosan oligomers present were studied. The chitosan oligomers were initially placed into the solution 3 nm above the surface of the silica slab. Due to the periodicity of the system in the z direction, the chitosan is able to access both Surface I and Surface II, which have the same structure and deprotonation level. The oligomers were placed closer to Surface I, so that the maximum level of oligomer adsorption is reached for that surface. However, upon reaching equilibrium the same level of adsorption should be observed for both surfaces.

In the systems where the chitosan oligomers were added one by one to the system, totalling four oligomers in the system, the number of adsorbed oligomers per surface

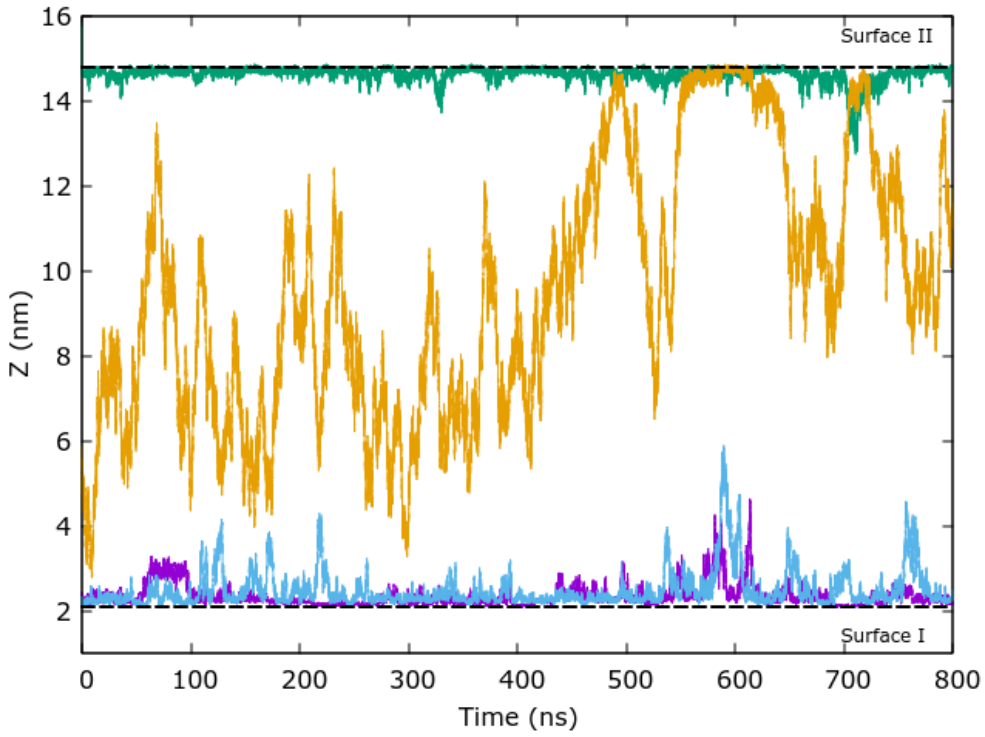

Figure 5.10: Z position of 4 chitosan 10-mer oligomer COMs.

was two for Surface I and one for Surface II. The oligomer that was added last to the simulation did adsorb to surface II for about 65 ns, but then it desorbed again (see Fig. 5.10). It remained in solution at 800 ns when the simulation was terminated.

In the systems where eight 10-mer chitosan oligomers were added simultaneously, the behaviour of the oligomers depended on the salt used. As before, in the system solvated with the sodium chloride, two chitosan oligomers adsorbed per surface and the other four oligomers remained in solution (see Fig. 5.11 for the oligomer COM z-coordinates throughout the simulation). This is equivalent to an adsorbed concentration of 0.35 monomers nm^{-2} (0.094 mg m^{-2}). This is in agreement with the experimental study by Tiraferri *et al.*[121] that used a quartz crystal microbalance with dissipation monitoring (QCM-D), and found adsorption of 0.083 mg m^{-2} at pH 4 and 100 mM NaCl concentration. They also measured the thickness of the adsorbed chitosan layer to be 0.6 nm at pH 4, which corresponds to the distance between N and C6 atoms of a chitosan monomer in the simulations, Which can be used to approximate the

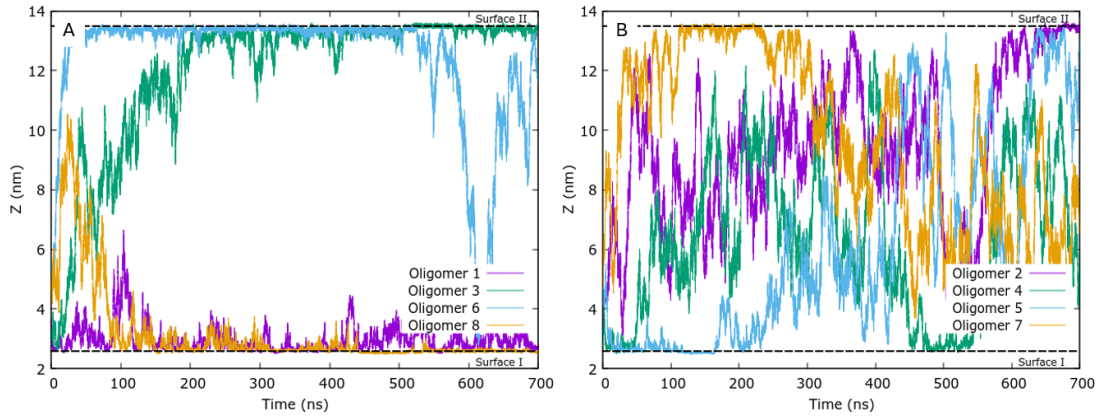

Figure 5.11: Z-position of 8 chitosan oligomers COMS. Oligomers 1,3,6 and 8 are shown in A, oligomers 2,4,5 and 7 are shown in B for clarity.

width of a single chitosan monomer in hydrated conformation adsorbed to the surface.

Fig. 5.12 shows the time-averaged density profiles of different species in various simulations relevant to the eight 10-mer system. Here, the density has been calculated in slices taken parallel to the silica surface (across the $x-y$ plane) at different values of z, with the z axis being normal to the silica surfaces. The negatively charged silica surface is screened by the ions present in the solution, which form the EDL, and this can be seen in the Na^+ cation density profile shown in Fig. 8(a) when no chitosan is present. As a weakly charged electrolyte, the chitosan oligomers compete with cations for silica adsorption sites. Each chitosan monomer contains a positively charged amino group ($-NH_3^+$), which has a +1e charge. This is the same valency as the sodium ions, and hence chitosan is able to displace sodium from the silica surface, as can be seen by the lower sodium peak heights in Fig. 5.12(b) when the chitosan oligomers are adsorbed.

In the system where the sodium ions are replaced by calcium ions, which have a +2e charge (Fig. 5.12(c)), the chitosan is not able to displace the calcium ions. Thus, chitosan is only able to adsorb to the deprotonated silanol sites which are unoccupied by calcium. There are 30 calcium ions and 36 deprotonated silanol groups in the system, which leave 6 deprotonated sites free for chitosan adsorption. In the density profile, it can be seen that the concentration of Ca^{2+} ions in bulk is zero, and that some chitosan adsorption occurs at surface I, due to it having uncompensated deprotonated

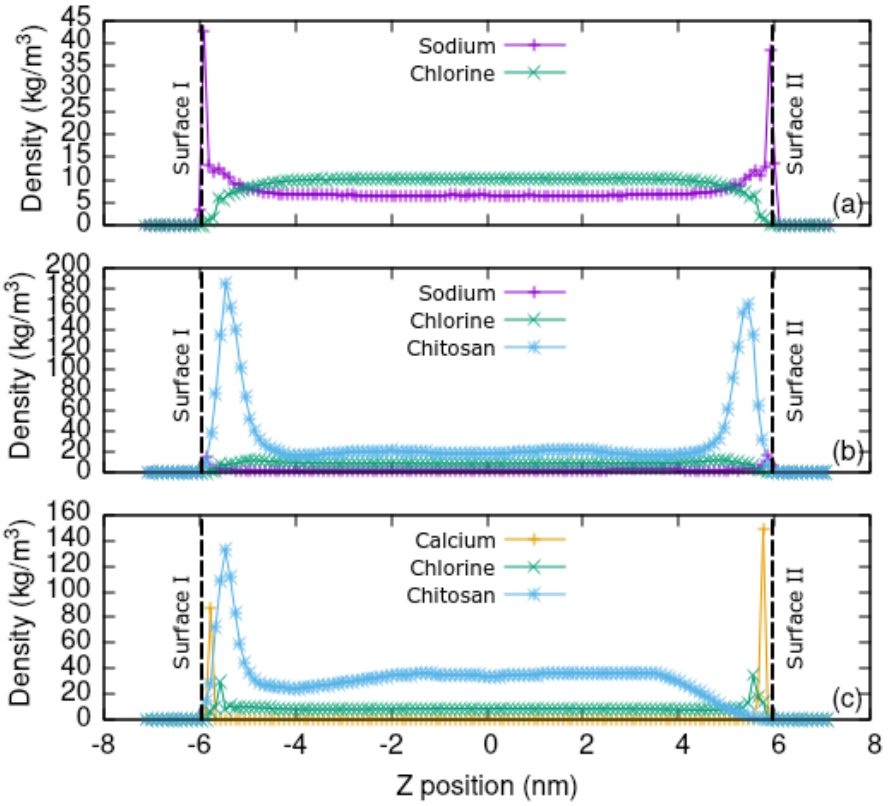

Figure 5.12: Partial density profiles in various simulations. (a) silica slab only plus NaCl solution, (b) with eight 10-mer chitosan olimers, (c) with chitosan but with sodium replaced by calcium ions.

silanol while the chitosan initial position was closer to surface I. This shows that charge compensation is a dominant feature of the chitosan adsorption process that ultimately dictates the density of the adsorbed chitosan layer, and furthermore, that this can be controlled by choice of solute ions.

5.4 Conclusions

MD simulations and enhanced sampling methods have been used to simulate chitosan oligomer adsorption to a model silica surface. The dynamics of adsorption of a single chitosan oligomer from aqueous solution with 0.15 mol L^{-1} NaCl concentration was studied, which corresponds to physiological conditions (or a technological application with high salt concentration) at pH 5. Chitosan readily adsorbs to the silica surface,

although it remains mobile on the surface.

Hydrogen bond formation and breaking has been studied throughout the simulation, and hydrogen bond breaking was further analysed using SMD. The chitosan atoms which contribute to hydrogen bonding are the nitrogen atom from amino group and the O6 atom. To further quantify the strength of adsorption, umbrella sampling was used to calculate the chitosan oligomer free energy of adsorption to the surface in aqueous solution with a NaCl concentration of 0.15 mol L^{-1}. The calculated energies were 3.60 ± 0.46 kcal mol^{-1} and 5.95 ± 0.25 kcal mol^{-1} for 10-mer and 6-mer oligomers respectively, which is $\approx$0.6 kcal mol^{-1} per monomer. This is comparable to the k_BT, which explains why chitosan oligomers remain mobile of the silica surface.

The simulations show that on average 0.35 monomers adsorb per nm^2 of the silica surface (a chitosan mass density of 0.094 mg m^{-2}) with NaCl salt, which is in good agreement with experimental studies, and aligns with the deprotonated silanol density (0.31 per nm^2). In addition, the chitosan layer thickness reported in literature corresponds to the thickness of single hydrated chain. The importance of salt used was also demsontrated, and it was found that divalent salts out-compete chitosan for potential absorption sites and thus prevent chitosan from adsorbing to the silica surface.

These results provide insight into fundamental interactions between chitosan and silica surfaces. This can be used as a guide for future experiment design, with the concept of charge compensation and ion valency used to control adsorbed densities. The optimisation of chitosan-coated silica nanoparticles could lead to more effective targeted drug delivery with lower cytotoxicity, and to optimise functionalised antimicrobial food packaging.

Chapter 6

Chitosan interaction with *E. Coli* cell membrane

Chitosan's antimicrobial activity is perhaps its most desirable property for applications. However, as discussed in Section 1.7 the mechanism of action is still debated. Thus, the optimal antimicrobial activity is hard to achieve.

In this chapter, chitosan interaction with a simplified model *Escherichia coli (E. coli)* bacterial membrane will be studied. The cell membrane is a first-line defence mechanism of the bacterial cell against antimicrobial compounds. Hence, studying chitosan's interaction with the membrane is the first step towards understanding chitosan's antimicrobial activity.

Chapter aims:

- To construct *in silico* model *E. coli* membranes.
- To study the dynamics of chitosan's interactions with the constructed membranes and determine the impact of the presence of chitosan on the membrane properties.
- To compare results with the literature in an effort to determine the level of detail required for *in silico* studies of chitosan-membrane interactions.

6.1 Bacterial membranes

Bacterial membranes differ depending on the bacterial species[134], but can be classified based on the main membrane structure using Gram staining[135]: gram-negative, gram-positive bacteria and less commonly gram-indeterminate groups. The main structural motifs of gram-positive and gram-negative bacterial membranes are shown in Fig. 6.1.

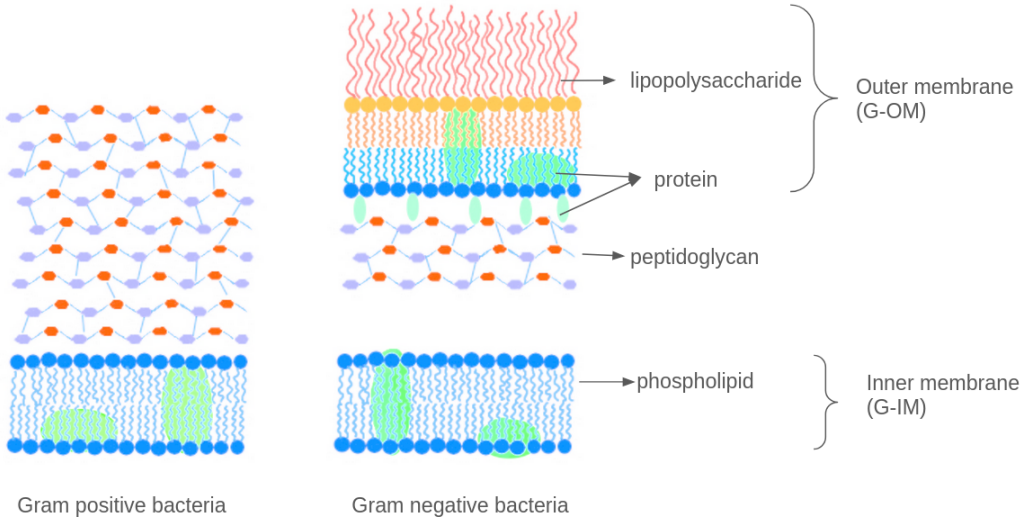

Figure 6.1: Schematic representation of gram positive and gram negative membranes.

Gram-positive bacteria have a thick, mesh-like peptidoglycan layer outside the cytoplasmic membrane, which stains purple with the crystal violet pigment used in Gram stain. A notable example of gram-positive bacteria with clinical significance is *Staphylococcus aureus*[136]. Although part of the normal human microbiome, it is an opportunistic pathogen that can cause various illnesses, from minor skin infections to life-threatening conditions such as meningitis and sepsis.

Gram-negative bacteria lack the peptidoglycan layer and do not stain with crystal violet. A notable example is *E. coli*[137], which is also part of the normal human biome and most strains are harmless. However, pathogenic strains can cause a range of diseases including gastroenteritis, sepsis and pneumonia. *E. coli* is frequently used as a model organism and is thus very well studied.

6.2 *E.coli* membrane structure

The cell envelope of gram-negative bacteria, including *E. coli*, consist of inner (G-IM) and outer membranes (G-OM) with a thin layer of peptidoglycan in between them[138]. G-OM is a highly asymmetric membrane, with the outer leaflet consisting of lipopolysaccharide (LPS) and Lipid A. LPS is typically composed of six acyl chains, core oligosaccharides and O-antigen polysaccharides. The inner leaflet consists of palmitoyl(16:0)-2-palmitoleoyl(16:1 cis-9)-phosphatidylethanolamine (PPPE), 1-palmitoyl(16:0)-2-vaceno
yl(18:1 cis-11)-phosphat-idylglycerol (PVPG) and 1',3'-1-dipalmitoyl-2-divaccenoyl cardiolipin (PVCL2). G-IM is symmetrical and consist of 1-palmytoyl-2-cis-9,10-methylene hexadecanoyl-phosphatidylethanolamine (PMPE), 1-oleoyl-2-(9Z-hexadecenoyl)-sn-glyceo-3-phosphoethanolamine (OYPE), 1-pentadecanoyl-2-cis-9,9R, 11S-methylene-hexadecanoyl-snglycero-3-phosphoethanolamine (QMPE), 1-palmitoyl-2-(9R, 11S-methylene-hexadecanoyl)-glycero-sn-3-phosphoglycerol (PMPG), 1-palmitoyl-2-(9Z-hexadecenoyl)-sn-glyceo-3-phosphoglycerol (PYPG), 1-palmitoyl-2-oleoyl-sn-glycero-3-phosphoethanolamine(POPE) and PVCL2[139]. A schematic drawing of all the lipids is shown in Figure 6.2.

The membrane also contains transmembrane proteins, which enable the bacteria to exchange ions and small molecules with its surroundings[140]. The transmembrane proteins contribute to 35-50 % [141, 142] of the membrane mass and $\approx$ 70 % of the total surface area in gram negative bacteria. The protein tend to be localised in clusters causing significant variations in local protein density[143].

This is particularly important for maintaining the transmembrane potential, which is the difference of electrostatic potentials across the membrane, typically in the range of 100 mV for *E. coli*.[144]. The transmembrane potential arises due to the different concentrations of ions, such as Na^+, K^+, Cl^- and Ca^{2+} across the membrane and is vital for the survival of bacterial cells, as it has an important role in cell motility, osmotic pressure regulation, cell signalling and transport of nutrients[145]. However, the simulations of membranes containing transmembrane proteins and explicit trans-

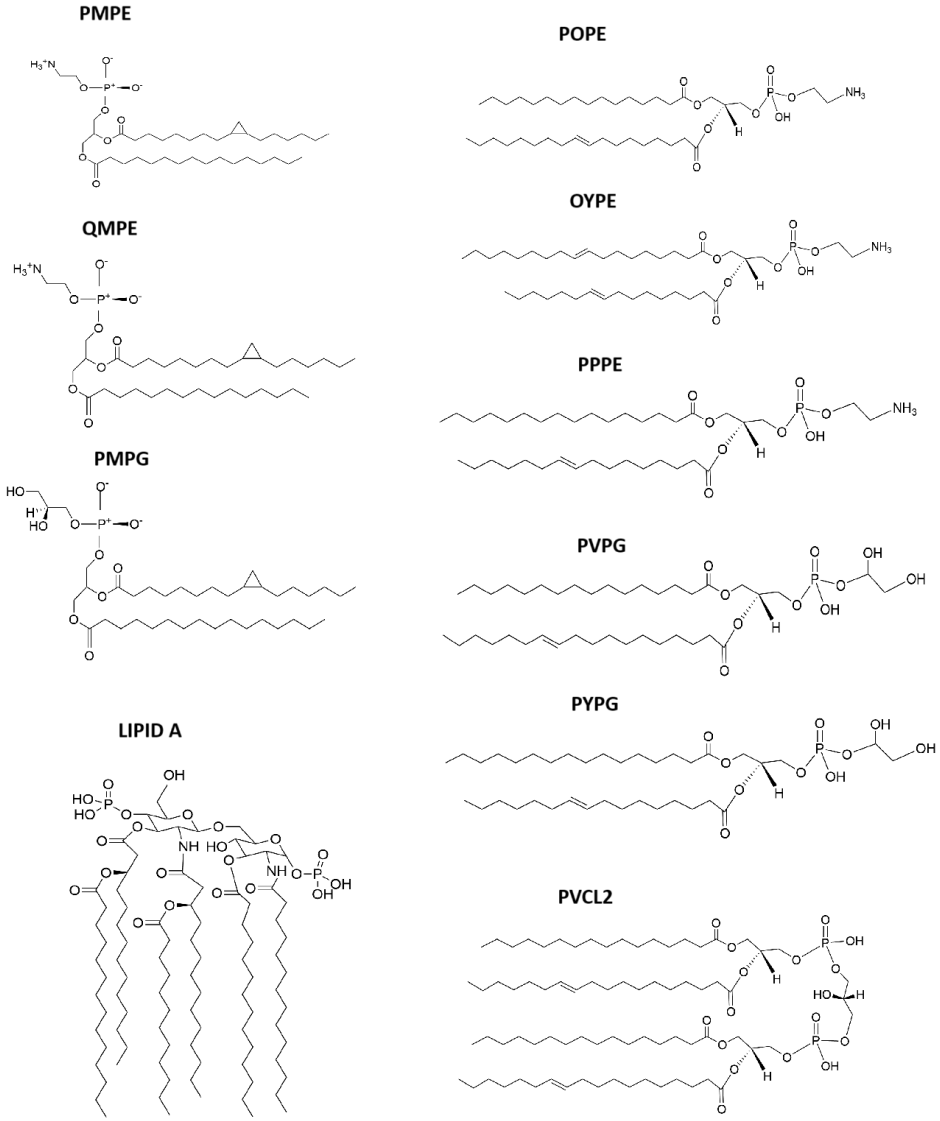

Figure 6.2: Schematic of G-OM and G-IM lipids.

membrane potential are outside the scope of this thesis due to the prohibitively high computational cost of such simulations.

6.2.1 Computational studies of chitosan interaction with membranes

In the computational studies the complex lipid structure of the *E. coli* is often replaced by a 3:1 ratio of POPE and 2-oleoyl-1-pamlitoyl-sn-glyecro-3-glycerol (POPG). POPE and POPG are simple model lipids often used in computational studies to construct model membranes, as they reduce the complexity (and often the size) of the simulation setup. POPE has neutral charge, while POPG had -1e charge, thus this simulation setup correctly reproduces net charge density of the G-IM.

There are not many computational studies that report the interactions of chitosan with bacterial membranes. Zhu *et al.*[146][1] studied chitosan interaction with a G-OM model membrane consisting of Lipid A in the outer leaflet and POPE and POPG (3:1 ratio) in the inner leaflet. They found that chitosan inserts itself $\approx$ 1 nm deep into the outer leaflet of the G-OM model membrane. Truong and Yi[147][2] used US to study chitosan heptamer interaction with a model symmetrical bacterial membrane consisting of POPE and POPG lipids (3:1 ratio). They found that the energy minima occurred at 2.6 nm from the centre of the lipid bilayer, with energy minima ranging from -4.78 to -10.5 kcal mol^{-1} depending on the chitosan protonation level. Neither of these studies modelled the LPS of the G-OM, which has a crucial role in protecting bacteria from antimicrobial agents. Atila *et al.*[148] used density functional theory (DFT) to study the interaction of chitosan, curcumin and α-tochopherol with a realistic model of G-OM containing the entire LPS structure. They claim that low M_w chitosan is able to diffuse through the LPS.

[1] This study was machine translated from Chinese to English using ChatGPT LLM (https://chatgpt.com/)

[2] This study was machine translated from Korean to English using ChatGPT LLM (https://chatgpt.com/)

6.3 Methodology

6.3.1 Membrane construction

The model *E. Coli* membranes were constructed using the CHARMM-GUI[149] Membrane builder [139]. To decrease the complexity of the simulation setup and rationalise the size of the system, the two membranes were created in two independent simulation systems. The lipid composition for the G-OM is shown in Table 6.1 with LPS with R1 Core and O1 O-antigen used, while the membrane composition for the G-IM is shown in Table 6.2. The R1 core sequence used was →3)β-D-glucose(1→3)[α-D-galactose(1→2)α-D-galactose(1→2)]α-D-Glucose(1→3)α-D-Glucose(1→3)[αLD-manno heptose(1→7)]αLD-mannoheptose(1→3)αLD-mannoheptose(1→5)[α-3-deoxy-D-manno-oct-2-ulosonic acid(2→4)]α-3-deoxy-D-manno-oct-2-ulosonic acid(2→ and the O1 O-antigen: O antigen: →3)β-D-Nacetyl-D-mannosamine(1→2)]α-L-rhamnose)α-L-rhamno se(1→2)α-D-Galactose(1→3)β-N-acetyl-D-glucosamine(1→.

Table 6.1: G-OM membrane composition

Lipid Name	Outer leaflet	Inner leaflet	Charge (e)
E. Coli Type 1 Lipid A	35	0	-10
PPPE	0	75	0
PVPG	0	20	-1
PVCL2	0	5	-2
Total	35	100	-350/-30

Both membranes were solvated to achieve 50 Å water padding on both sides and 190 Ca^{2+} ions were added to the core O antigen region of G-OM to neutralise the system and additional 81 Na^{+} and Cl^{-1} ions were added to obtain a salt concentration of 0.15 g mol^{-1}. The G-IM was neutralised using sodium ions and further sodium and chloride ions were added to obtain a salt concentration of 0.15 g mol^{-1}. For both systems, the "More charm minimization during input generation" option was selected and NAMD outputs were produced. The simulations were conducted in NAMD 3.7b with CHARMM36 FF.

Table 6.2: G-IM membrane composition

Lipid Name	Inner/Outer leaflet	Charge (e)
PMPE	46	0
POPE	13	0
QMPE	12	0
OYPE	8	0
PMPG	10	-1
PYPG	9	-1
PVCL2	2	-2
Total	100	-23

6.3.2 Membrane simulation protocol

Membrane simulations require a careful equilibration protocol due to the membrane's high compressibility compared to that of the water. To achieve a stable, well-equilibrated membrane, the CHARMM-GUI protocol was followed[139] and conducted in 6 steps. During the equilibration process planar, dihedral and carbohydrate chair restraints were applied with progressively decreasing strength in each step as seen in Table 6.3. The equilibration was performed in an NPT ensemble with semi-isotropic pressure coupling using a Langevin thermostat and barostat.

Table 6.3: Parameters for the equilibration process. PR - planar restraint, DR - dihedral restraint, and CR - carbohydrate chair restraint potential strengths are given in kcal mol^{-1} $Å^{-2}$.

Step	Minimize (steps)	Run (steps)	Timestep (fs)	PR	DR	CR
1	10^4	1.25×10^5	1.0	5	500	500
2	-	1.25×10^5	1.0	5	200	200
3	-	1.25×10^5	1.0	2	100	100
4	-	2.5×10^5	2.0	1	100	100
5	-	2.5×10^5	2.0	0.2	50	50
6	-	2.5×10^5	2.0	0	0	0

The production runs were conducted for 500 ns with no restraints in the NPT ensemble at 303.15 K and 1 bar. A 2 fs timestep was used with a Langevin thermostat and semi-isotropic Langevin pressure coupling. The last 100 ns of the trajectory were analysed. The last frame of the simulation was used to construct new systems containing chitosan oligomers. A G-OM system containing one 10-mer oligomer was

constructed (see Fig. 6.3) and three independent simulations were run with different initial velocities. For both G-OM and G-IM systems, eight 10-mer oligomers were constructed, where the oligomers were added to the system in 4 × 2 arraignments with 15 Å space between the oligomers, as shown in Fig. 6.4. In both cases, the oligomer(s) were added to the system 30 Å above the surface of the membrane. The overlapping water and ions were deleted (with a 4 Å margin). The system was then neutralised by adding Cl^- ions. The simulations were conducted with the same setting as before for the production run.

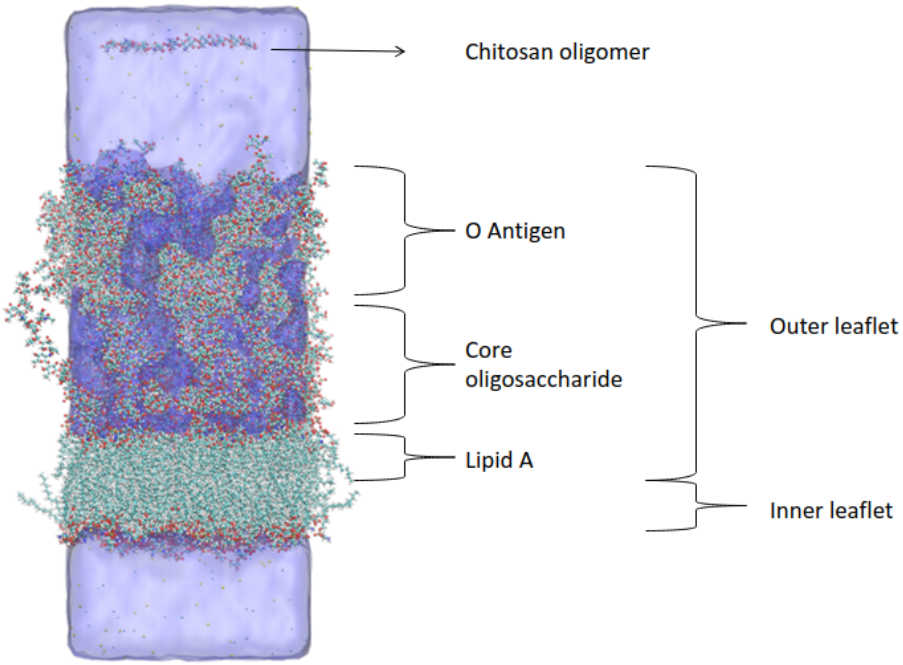

Figure 6.3: G-OM system setup with single chitosan oligomer.

6.3.3 Analysis

The trajectories were analysed using VMD and its plugins. A pre-analysis membrane alignment was performed by a tcl script (see Appendix) which centred the membrane in the middle of the simulation cell and removed the membrane COM motion. The partial densities were calculated by VMD's Membrane plugin using the last 100 ns of the trajectories along the z-axis with 1 Å bin spacing. The membrane thickness

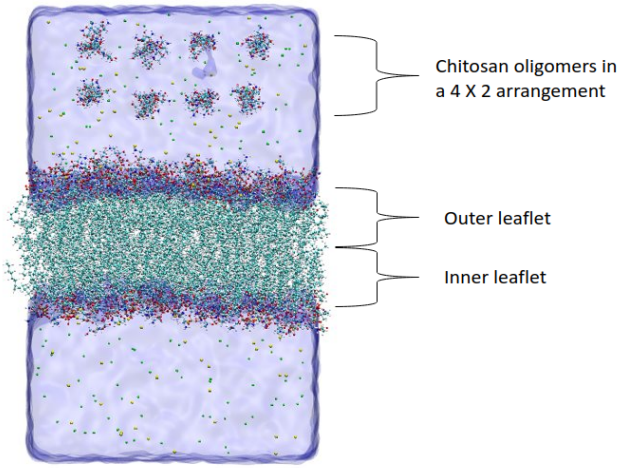

Figure 6.4: G-IM setup with eight chitosan oligomers.

was measured as the time-averaged distance between average z-position of phosphorus atoms of the lipid heads (P, PA and PB) in the lower and upper leaflet. Hydrogen bonds were calculated using "measure hbonds" VMD command with standard 3.5 Å and 30° cutoffs.

6.4 Results and Discussion

6.4.1 G-OM charge distribution

G-OM is a highly charged membrane as can be seen from Table 6.1. Thus, it can be assumed that electrostatics and charge distribution govern the dynamics of chitosan interactions with G-OM. Fig. 6.5 shows a snapshot of the G-OM after 500 ns of simulation time, with atoms which contribute to net membrane charge and ions emphasised. The negatively charged phosphate group oxygens in the outer leaflet (blue) are neutralised by Ca^{2+} ions (pink). The sodium ions have a higher concentration near the inner leaflet due to the negatively charged phosphate group oxygens (red) found at the edge of the inner leaflet.

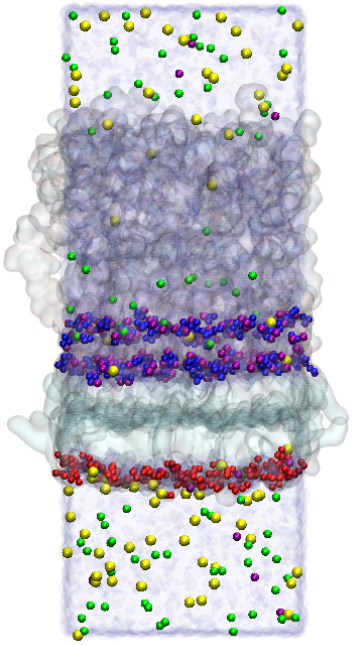

Figure 6.5: Equilibrated G-OM membrane snapshot with ions and the most negatively charged ions emphasised. Atom colours: red - phosphate group oxygens in the inner leaflet, blue - phosphate group oxygens in the outer leaflet, yellow - sodium, green - chloride, pink - calcium.

6.4.2 Single chitosan oligomer adsorption to G-OM

In the simulations where a single chitosan oligomer was initially placed into solution 30 Å above G-OM (shown in Fig. 6.3), the chitosan subsequently diffuses towards the membrane's lower leaflet and adsorbs in two out of three replicates. Due to the very high similarity of the two trajectories, only one is described as an exemplar. Fig. 6.6 shows the COM z-position of the chitosan oligomer during the simulation. The oligomer approaches the surface at 74 ns with the orientation normal to the membrane surface. During the adsorption process the oligomer reoriented itself to a parallel orientation to the membrane surface. A stable adsorption was achieved at 80 ns. One of three triplicate simulations showed mildly different dynamics to the previous two, hence this trajectory was extended to 200 ns simulation time. The oligomer first diffused towards the outer membrane and interacted with the outermost part of the LPS. Following the interaction with the LPS, chitosan oligomer diffused back into the solution and adsorbed

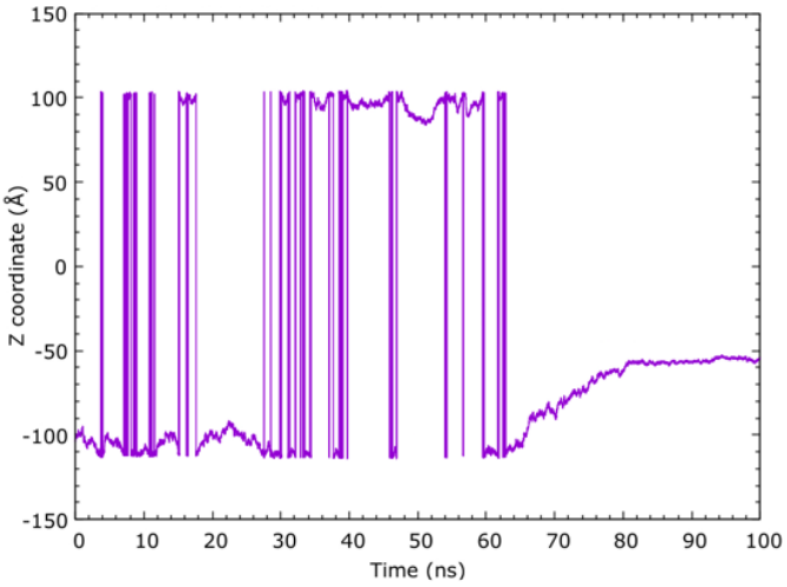

Figure 6.6: Z-position of COM of chitosan oligomer during the simulation. The vertical lines on the graph indicate chitosan COM crossed the periodic boundary in the z direction.

to the inner leaflet by the end of 200 ns simulation time. During the interaction with LPS, chitosan formed several short-lived hydrogen bonds with the LPS. The bonds formed are the same as those formed when multiple oligomers are present in the solution and thus further described in the next section.

6.4.3 Multiple oligomer interaction

To study systemic changes to the membrane due to the larger presence of the chitosan oligomers in the system, a membrane simulation with eight chitosan oligomers present was conducted. Fig. 6.7A shows the z-coordinate of all oligomer COMs. Three chitosan oligomers adsorbed to the inner leaflet within 50 ns of the simulation and additional oligomers adsorbed to the inner leaflet at 150 ns and 400 ns. In total, five oligomers adsorbed to the inner leaflet and adopted a completely parallel orientation to the membrane. The remaining three oligomers in the solution weakly interacted with the LPS at the upper leaflet. Fig. 6.7B shows the hydrogen bonding analysis for the main hydrogen bonds present during the entire simulation, only the most populated hydrogen

bonds are shown. As can be seen, chitosan's amino group is the main contributor to the hydrogen bonding as the donor, with minor contributions from O3 and O6. The main acceptors are phosphate group oxygens (O13, O14, OP13, OP14). The inner leaflet has the total -30e charge which is overcompensated compensated by the five adsorbed oligomers which have a total +50e charge.

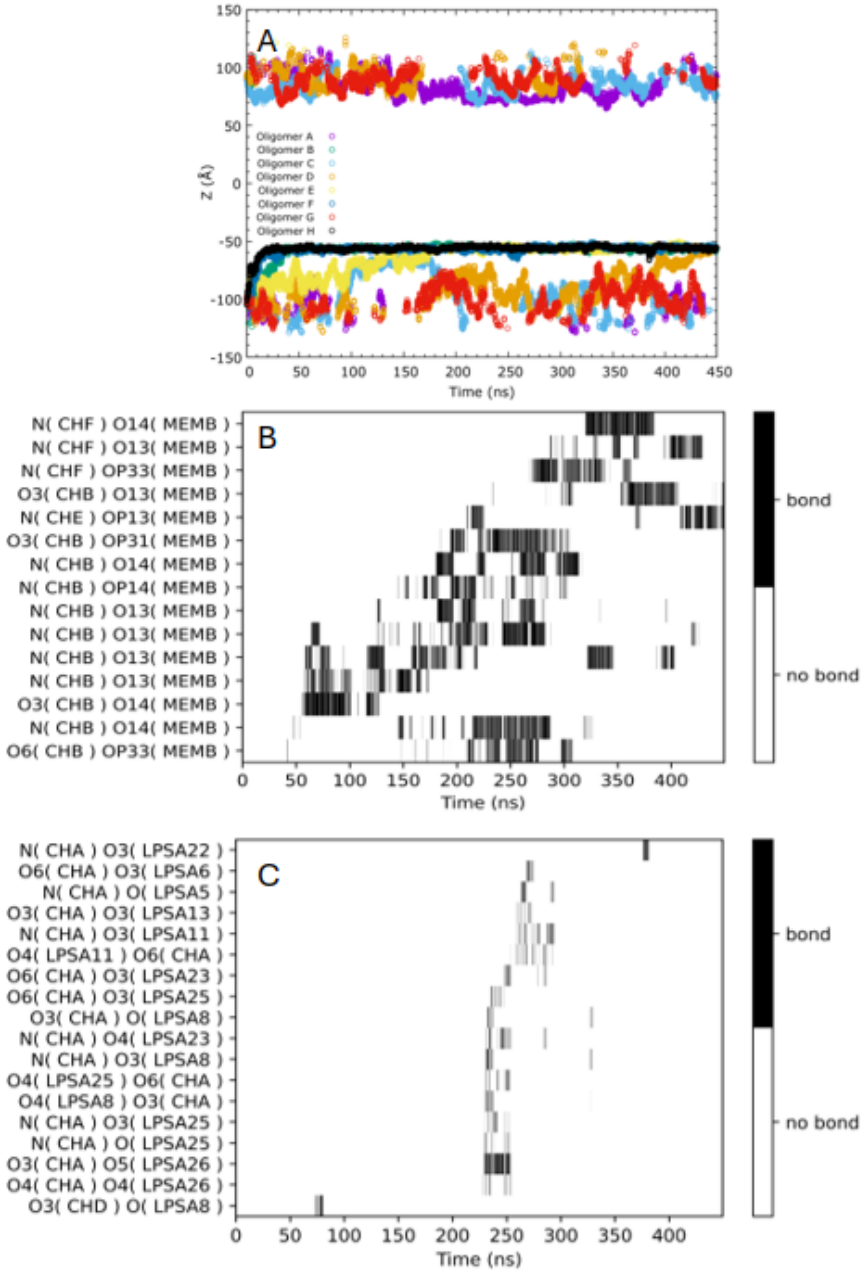

Figure 6.7: The z-coordinate of the COM of the eight chitosan oligomers is shown in panel A for G-OM system. In B, the hydrogen bonds between the oligomers and the inner leaflet and C the hydrogen bonds between the oligomers and the LPS for the entire trajectory. The hydrogen bonds are shown in donor acceptor order and the segment ids are shown in bracket.

Fig.6.7C shows the hydrogen bonds between chitosan oligomers and the LPS. Here,

it can be seen that the chitosan forms short-lived hydrogen bonds with LPS. Chitosan mainly acts as the hydrogen bond donor although there are some bonds where chitosan is the acceptor. The main chitosan donors are amino group nitrogens (N) and hydroxyl group oxygens (O3, O4, O6). The main acceptors are the hydroxyl group oxygens (O3, O6) and the acetyl group oxygen (O). The overall charge of the outer leaflet is -350e, however, the negative charges are concentrated in the lipid A and core oligosccharide region where they are neutralised by Ca^{2+} ions, thus it is unlikely that the chitosan interaction with LPS is driven by electrostatics.

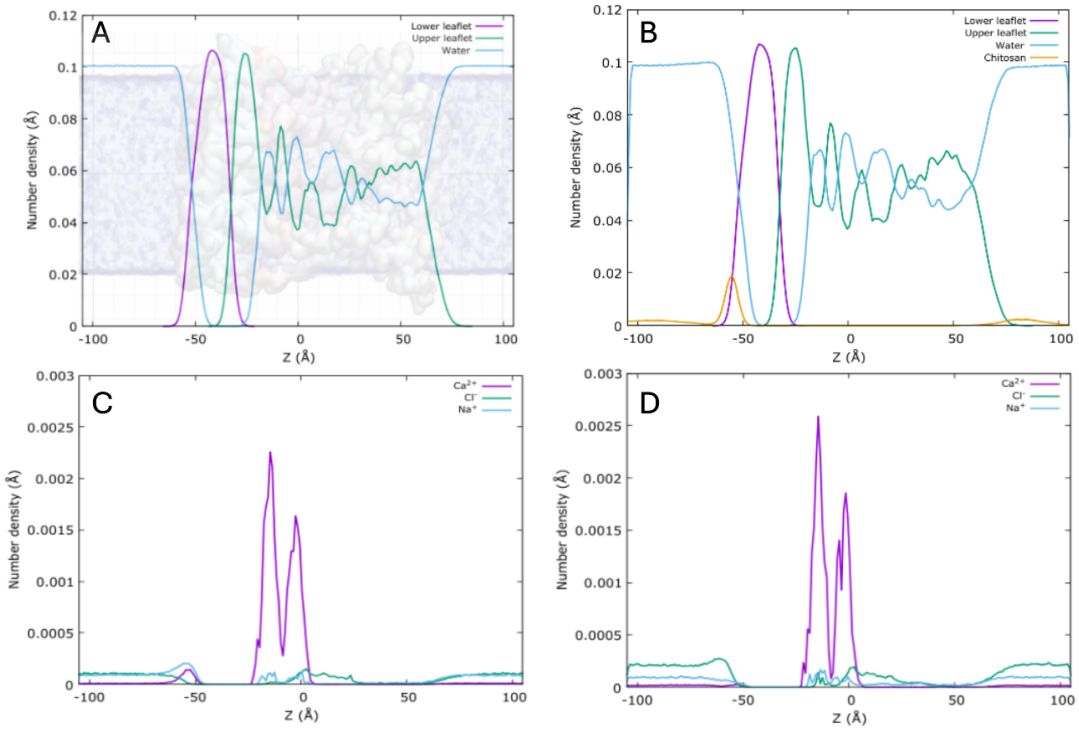

Figure 6.8: Time averaged G-OM density profiles with (panels B and D) and without (A and C) the eight chitosan oligomers. The ions are shown in C and D, and the lipids, water in A and B. B also shows the profile for the chitosan oligomers.

The membrane thickness (excluding LPS) was calculated to be 35.9±0.2 Å with no chitosan present and 36.2±0.2 Å with eight chitosan oligomers present, indicating that chitosan did not influence the membrane thickness in a significant way. The calculated membrane thickness is also consistent with CHARMM-GUI reference paper, which reports a membrane thickness of 36.6±0.3 Å[150]. Fig. 6.8 shows the time-

averaged density profile of the simulated membranes with (B and D) and without (A and C) chitosan present. Chitosan adsorbs to the inner leaflet of the membrane at -50 Å and displaces Ca^{2+} ions from the surface of the inner leaflet and causes higher concentration in the core LPS region. Chloride ion concentration is also increased near the inner leaflet due to the presence of chitosan. Thus, the presence of chitosan changes the ion placement around the membrane structures.

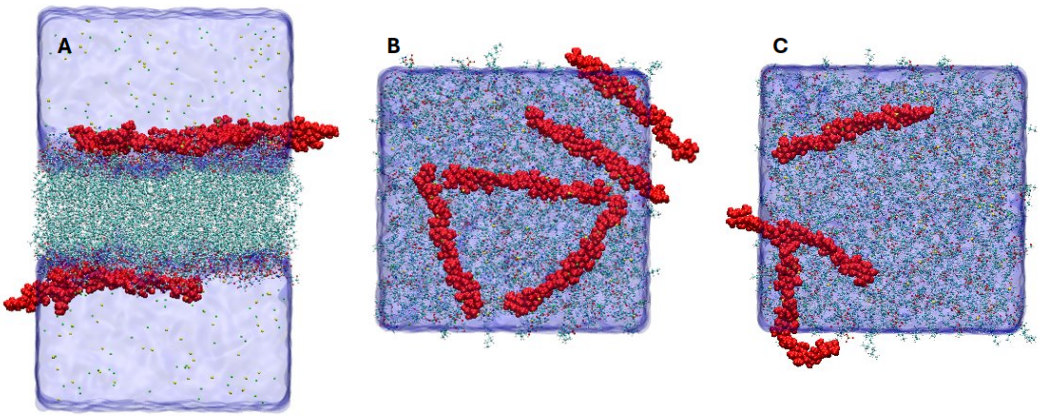

Figure 6.9: Snapshot of the G-IM with 8 oligomers system at the end of simulation. A - side view, B - top view, C - bottom view. Chitosan is shown in red for emphasis.

Chitosan oligomers readily adsorb to the G-IM membrane. G-IM is negatively charged with a -23e charge per leaflet. Chitosan oligomers adsorb asymmetrically to the membrane with five oligomers adsorbing to the top leaflet and three adsorbing to the lower leaflet as can be seen in Fig. 6.9. Each chitosan oligomer has a +10e charge, thus chitosan adsorption changes the surface charge of the membrane. Partial density profiles, shown in Fig. 6.10 show the changes in ion concentration around the membrane in the system with and without chitosan. In the system without chitosan, (see Fig. 6.10C) Na^+ density is highest near the membrane surface screening the membrane's negative charge. In the system with chitosan oligomers adsorbed to the membrane, (see Fig. 6.10D) Cl^- replaced the sodium ions near the surface. The asymmetric concentrations of chloride ions are due to the asymmetric chitosan adsorption to the membrane surface. Fig. 6.10A and D show that there is no overall change to the membrane density due to the chitosan adsorption. This is further evidenced by

the average membrane thickness values of 38.74±0.44 Å and 38.99±0.42 Å without and with adsorbed chitosan respectively. These values are also in agreement with the value of 38.3±0.1 Å reported in CHARMM-GUI reference paper[150]. Despite the lack of systemic change to the density of the membrane, chitosan adsorption disrupts the ionic profile potentially disrupting the transmembrane potential which is vital for normal cell functioning.

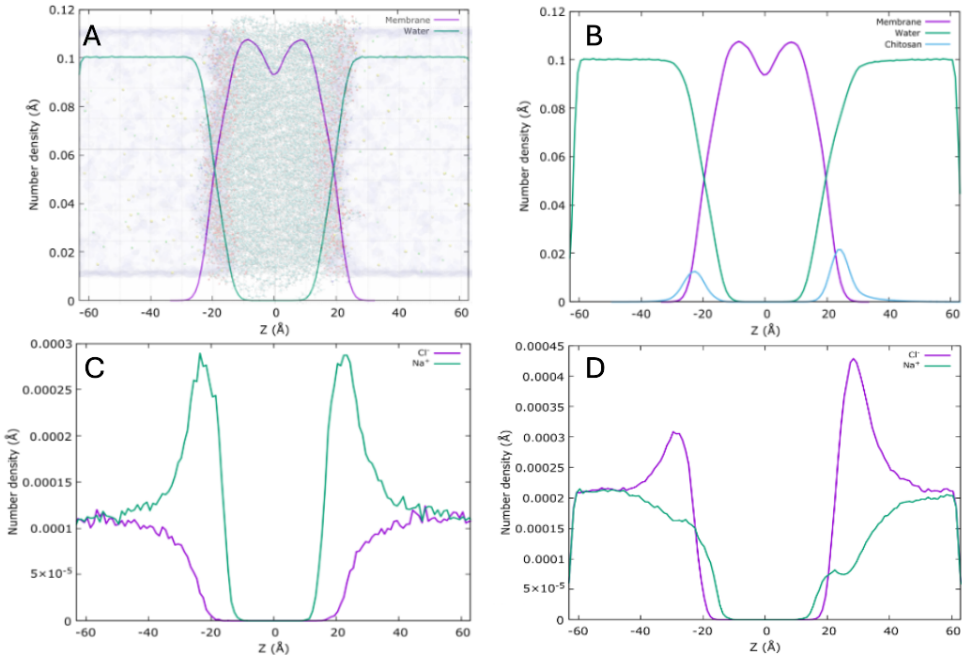

Figure 6.10: Time averaged G-IM density profile A and C - system without chitosan, B and D system with 8 chitosan oligomers. Note outer leaflet is positioned z>0.

The main hydrogen bonds between chitosan and the G-IM are shown in Fig. 6.11. The first hydrogen bonds appear at around 48 ns. The main hydrogen bond donors are nitrogen atoms which are part of chitosan's amino group. Chitosan's O3 and O6 also act as hydrogen bond donors. The main hydrogen bond acceptors are oxygens located in the phosphate groups of the membrane's phospholipid heads indicating a non-specific electrostatics-driven interaction. Liu *et al.*[151] studied chitosan interaction with phosphatidylcholine (PC) liposomes using IR spectra and found chitosan's amino group interacts with the PC phosphate group, which is consistent with the hydrogen bonding pattern observed here.

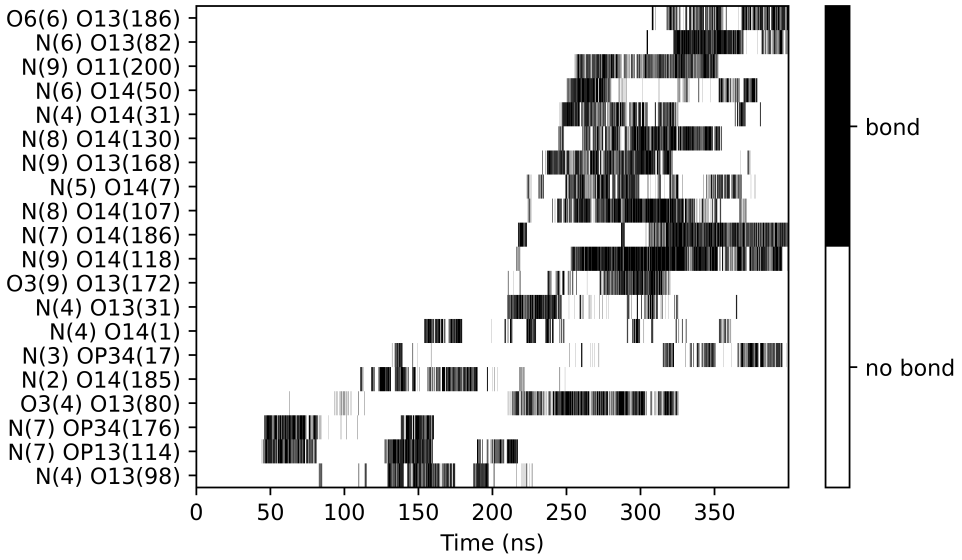

Figure 6.11: G-IM hydrogen bond analysis

6.5 Conclusions

Chitosan interactions with realistic model *E. coli* outer and inner membranes were explored. Here, only weak chitosan interaction with LPS was observed, while strong adsorption was observed for an inner leaflet of the G-OM. This highlights the importance of using more realistic membrane models over highly simplistic symmetric ones, which do not capture the required level of detail. The chitosan is readily adsorbed to the G-IM, similar to the results reported in the literature for simple model bacteria models.

While the research presented in this chapter presents advances in the understanding of the origins of chitosan's antimicrobial activity, it also shows the need for further research on chitosan's interaction with bacterial components. Bacterial membranes contain transmembrane proteins which facilitate the transport of the small hydrophilic molecules across the bacterial membrane, which may be one of the routes through which low-M_w chitosan may enter the cell. Furthermore, the transmembrane potential was not modelled here, which is important for cell functioning and the transport of molecules across the membrane. To further investigate the energy landscape of the chitosan diffusion through the bacterial membrane, US could be used which requires

significant computational resources.

The findings presented here can be used as a guide for future research on the origins of chitosan's antimicrobial activity. This preliminary research indicates chitosan interacts with the G-OM membrane in a somewhat unexpected way which merits further examination. Firstly, chitosan oligomer interaction with the inner and outer leaflets of the G-OM greatly differs. Thus, using a simple phospholipid bilayer (whether experimental or computationally) is not sufficient to fully explain the origins of chitosan's antimicrobial activity. Furthermore, a lack of strong interactions between chitosan and LPS may indicate that porin proteins have a greater role in chitosan diffusion through the membrane than previously thought.

Chapter 7

Conclusions

7.1 Summary of results

Chitosan is a promising polysaccharide with many potential applications, including food packaging and drug delivery due to its biodegradability and antimicrobial properties. Chitosan is derived from chitin, the second most abundant biopolymer in nature. However, despite the long history of chitosan research the lack of understanding of chitosan interaction at the interfaces has slowed the commercialisation of chitosan-containing materials. To guide the rational design of novel material it is crucial to understand the underlying molecular mechanisms governing the adsorption processes. The aim of this thesis was to study fundamental properties of chitosan interactions with surfaces at the aqueous interfaces.

To achieve this, extensive MD simulations were conducted. In chapter 3, the chitosan model was validated against available literature to ensure the accuracy of the novel results. Then, using the chosen model the interaction of chitin and chitosan with α-chitin nanocrystal and silica surfaces were studied and presented in chapters 4 and 5.

Chitin and chitosan oligomer adsorption to α-chitin nanocrystal surface was found to be governed by the hydrogen bond network formation. The free energy landscapes of the chitin trimer, and chitin and chitosan hexamers adsorbing to the crystal surface using umbrella sampling were calculated. The oligomer-crystal binding energy was -

12.5 kcal mol^{-1} and -2 kcal mol^{-1} for chitin and chitosan 6-monomer-long oligomer chains respectively. The binding energy of chitin crystal and excess surface energy in a vacuum were calculated. Then, using SMD pulling, the strength of the chitin oligomer binding to the chitin crystal surface and the breaking of the relevant hydrogen bonds were evaluated. The SMD pulling disrupted the intra-chain bonding and caused conformational changes in the oligomer.

Next, in chapter 5, chitosan oligomer adsorption to a model silica surface was studied and it was found that this process is governed by electrostatic interactions. Chitosan readily adsorbs to the silica surface, although it remains mobile on the surface. Hydrogen bond formation and breaking have been studied throughout the simulation, and hydrogen bond breaking was further analysed using SMD. The chitosan atoms which contribute to hydrogen bonding are the nitrogen atom from the amino group and the O6 atom. To further quantify adsorption strength, umbrella sampling was used to calculate the chitosan oligomer free energy of adsorption to the surface in aqueous solution with a NaCl concentration of 0.15 mol L^{-1}. The calculated energies were 3.60 ± 0.46 kcal mol^{-1} and 5.95 ± 0.25 kcal mol^{-1} for 10-mer and 6-mer oligomers respectively, which is $\approx$0.6 kcal mol^{-1} per monomer. This is comparable to the k_BT, which explains why chitosan oligomers remain mobile on the silica surface.

The simulations show that on average 0.35 monomers adsorb per nm^2 of the silica surface (a chitosan mass density of 0.094 mg m^{-2}) with NaCl salt, which is in good agreement with experimental studies and aligns with the deprotonated silanol density (0.31 per nm^2). In addition, the chitosan layer thickness reported in the literature corresponds to the thickness of a single hydrated chain. The importance of salt used was also demonstrated, and it was found that divalent cations out-compete chitosan for potential absorption sites and thus prevent chitosan from adsorbing to the silica surface.

Lastly, in chapter 6, the interaction of chitosan with gram-negative *E. coli* membranes was studied. Here, the simulation setup focused on constructing the gram negative outer and inner membranes with realistic lipid and lipopolysaccharide component composition, while keeping the system size sufficiently small to efficiently use

available computational resources. Chitosan oligomers readily adsorbed to the inner membrane and this behaviour is in line with published literature, where interaction of chitosan with simple negatively charged membranes was conducted. However, the simulations of chitosan with the outer membrane showed that chitosan oligomers interact only weakly with LPS, which may indicate the greater role of transmembrane proteins for the diffusion of the chitosan oligomers into the membrane than previously reported in computational studies.

7.2 Conclusions and perspectives for future research

The research presented in this thesis lays fundamental groundwork for studying chitosan interactions at the aqueous interfaces. The methodology presented here can be used as a guide for future research and can be expanded to chitosan interaction with other surfaces, while the scripts developed for pre-processing and analysis can be used for other similar systems with no or little editing required. In particular, the script which constructs polysaccharide oligomers and crystals can be easily expanded for simulations of chemically similar polysaccharides and thus enable the study of chemically modified polymers. Such research would be beneficial to further expand the impact of this work.

Results presented in chapters 4 and 5 can be used to inform the rational design of novel chitosan composite materials for a variety of applications. Potential applications include chitosan-coated chitin NPs used as non-toxic antimicrobial spray coatings, chitosan-coated silica nanoparticles which can be used for targeted drug delivery and composite antimicrobial nanoparticles, which can be used as a filler in functionalised bioplastic-packaging. Furthermore, the results obtained in chapter 4 can be used to inform the design of enzymes, which can be used for enzymatic deacetylation of chitin and thus provide a green alternative to the harsh chemicals used in current industrial chitosan production.

Interest in the simulations of complex bacterial membranes and their interactions with various antimicrobial compounds is growing. The work presented in chapter 6 explored the chitosan interaction with *E. coli* G-IM and G-OM membranes. While chitosan readily adsorbs to the G-IM and inner leaflet of the G-OM, it only weakly in-

teracts with the LPS. To the author's best knowledge, the *in silico* studies of chitosan interaction with full LPS dynamics have not been previously reported in the literature. This research highlights the downsides of oversimplification when conducting computational simulations and lays the groundwork for future studies aiming to elucidate the origins of chitosan's antimicrobial activity.

The simulations presented in this thesis were all-atom MD simulations, and thus limited in size to ∼150k atoms and sub-microsecond simulations times, which limit the size and complexity of the simulated systems. Thus, the results presented here could be complemented by coarse-grained modelling of chitosan composite systems. Coarse-grained simulations enable much larger system size and simulation time, however, they come with a reduced precision due to the simplifications used in model construction. It is important to validate coarse-grained models against fully atomistic simulations. The results presented in Chapter 4, such as glycosidic bond and dihedral angles and the hydrogen bonding dynamics can be used to inform new coarse-grained models. Furthermore, free energy curves such as those calculated from US simulations are particularly suited for this purpose. Thus, using coarse-grained simulations could help bridge the gap between the fully atomistic simulations and experiments.

In conclusion, this thesis addresses the gap in understanding chitosan adsorption in aqueous environments. The insights presented here not only contribute to the existing body of research but also provide guidance for the design of novel chitosan materials for antimicrobial applications.

Bibliography

[1] S. Lee, L. T. Hao, J. Park, D. X. Oh, and D. S. Hwang, "Nanochitin and nanochitosan: Chitin nanostructure engineering with multiscale properties for biomedical and environmental applications," *Advanced Materials*, vol. 35, no. 4, p. 2203325, 2023.

[2] A. Yurtsever, P.-X. Wang, F. Priante, Y. Morais Jaques, K. Miyata, M. J. MacLachlan, A. S. Foster, and T. Fukuma, "Probing the structural details of chitin nanocrystal–water interfaces by three-dimensional atomic force microscopy," *Small Methods*, vol. 6, no. 9, p. 2200320, 2022.

[3] B. Bellich, I. D'Agostino, and A. Cesàro, ""the good, the bad and the ugly of chitosans," *Marine drugs*, vol. 14, no. 5, p. 99, 2016.

[4] C.-L. Ke, F.-S. Deng, C.-Y. Chuang, and C.-H. Lin, "Antimicrobial actions and applications of chitosan," *Polymers*, vol. 13, no. 6, 2021.

[5] R. Priyadarshi and J.-W. Rhim, "Chitosan-based biodegradable functional films for food packaging applications," *Innovative Food Science & Emerging Technologies*, vol. 62, p. 102346, 2020.

[6] M. Dash, F. Chiellini, R. Ottenbrite, and E. Chiellini, "Chitosan—a versatile semi-synthetic polymer in biomedical applications," *Progress in Polymer Science*, vol. 36, no. 8, pp. 981–1014, 2011. Special Issue on Biomaterials.

[7] L. Mu, L. Wu, S. Wu, Q. Ye, and Z. Zhong, "Progress in chitin/chitosan and their derivatives for biomedical applications: Where we stand," *Carbohydrate Polymers*, vol. 343, p. 122233, 2024.

[8] J. Jin, B. Luo, S. Xuan, P. Shen, P. Jin, Z. Wu, Y. Zheng, J. Jin, B. Luo, S. Xuan, P. Shen, P. Jin, Z. Wu, and Y. Zheng, "Degradable chitosan-based bioplastic packaging: Design, preparation and applications," *International journal of biological macromolecules.*, vol. 266, p. 131253, 2024.

[9] R. A. Ilyas, H. A. Aisyah, A. H. Nordin, N. Ngadi, M. Y. M. Zuhri, M. R. M. Asyraf, S. M. Sapuan, E. S. Zainudin, S. Sharma, H. Abral, M. Asrofi, E. Syafri, N. H. Sari, M. Rafidah, S. Z. S. Zakaria, M. R. Razman, N. A. Majid, Z. Ramli, A. Azmi, S. P. Bangar, and R. Ibrahim, "Natural-fiber-reinforced chitosan, chitosan blends and their nanocomposites for various advanced applications," *Polymers*, vol. 14, no. 5, 2022.

[10] G. Crini, "Historical review on chitin and chitosan biopolymers," *Environmental Chemistry Letters*, vol. 17, pp. 1623–1643, Dec. 2019.

[11] F. Hoppe-Seyler, "Ueber chitin und cellulose," *Berichte der deutschen chemischen Gesellschaft*, vol. 27, no. 3, pp. 3329–3331, 1894.

[12] W. N. Haworth, "Bakerian lecture-the structure, function and synthesis of polysaccharides," *Proceedings of the Royal Society of London. Series A. Mathematical and Physical Sciences*, vol. 186, no. 1004, pp. 1–19, 1946.

[13] W. W. Heckert, "Textile, us patent 2,099,363," 1937.

[14] L. LL, "Manufacture of paper. us patent 2,184,307," 1939.

[15] M. M, "Antistatic photographic film. us patent 2,139,689," 1938.

[16] M. RW, "Adhesive. us patent 2,182,524," 1939.

[17] R. A. Muzzarelli, C. Jeuniaux, G. W. Gooday, *et al.*, *Chitin in nature and technology*, vol. 385. Springer, 1986.

[18] S. HIRANO, "Production and application of chitin and chitosan in japan," *Chitin and chitosan.*, pp. 37–43, 1989.

[19] B. L. Rivas and J. D. Giraldo, "Direct ionization and solubility of chitosan in aqueous solutions with acetic acid," *Polymer bulletin*, vol. 78, no. 3, pp. 1465–1488, 2021.

[20] L. Vachoud, N. Zydowicz, and A. Domard, "Physicochemical behaviour of chitin gels," *Carbohydrate research.*, vol. 326, no. 4, pp. 295–304, 2000.

[21] P. Sikorski, R. Hori, and M. Wada, "Revisit of α-chitin crystal structure using high resolution x-ray diffraction data," *Biomacromolecules*, vol. 10, no. 5, pp. 1100–1105, 2009.

[22] K. Okuyama, K. Noguchi, T. Miyazawa, T. Yui, and K. Ogawa, "Molecular and crystal structure of hydrated chitosan," *Macromolecules.*, vol. 30, no. 19, pp. 5849–5855, 1997.

[23] K. Noguchi, M. Kanenari, T. Egawa, K. Osawa, K. Okuyama, and K. Ogawa, "Structural diversity of chitosan and its complexes," *Carbohydrate Polymers*, vol. 41, no. 3, pp. 237–247, 2000.

[24] T. Yui, K. Imada, K. Okuyama, Y. Obata, K. Suzuki, and K. Ogawa, "Molecular and crystal structure of the anhydrous form of chitosan," *Macromolecules.*, vol. 27, no. 26, pp. 7601–7605, 1994.

[25] J. Kawada, T. Yui, Y. Abe, and K. Ogawa, "Crystalline features of chitosan-l- and d-lactic acid salts," *BIOSCIENCE BIOTECHNOLOGY AND BIOCHEMISTRY*, vol. 62, pp. 700–704, APR 1998.

[26] M. Rinaudo and I. Younes, "Chitin and chitosan preparation from marine sources. structure, properties and applications," *Marine drugs /*, vol. 13, no. 3, pp. 1133–1174, 2015.

[27] I. Tsigos, A. Martinou, D. Kafetzopoulos, and V. Bouriotis, "Chitin deacetylases: new, versatile tools in biotechnology," *TRENDS IN BIOTECHNOLOGY*, vol. 18, pp. 305–312, JUL 2000.

[28] X. Liu, L. Song, L. Li, S. Li, and K. Yao, "Antibacterial effects of chitosan and its water-soluble derivatives on e. coli, plasmids dna, and mrna," *Journal of Applied Polymer Science*, vol. 103, no. 6, pp. 3521–3528, 2007.

[29] K. Divya, S. Vijayan, T. K. George, and M. Jisha, "Antimicrobial properties of chitosan nanoparticles: Mode of action and factors affecting activity," *Fibers and Polymers*, vol. 18, no. 2, pp. 221–230, 2017.

[30] E. I. Rabea, M. E.-T. Badawy, C. V. Stevens, G. Smagghe, and W. Steurbaut, "Chitosan as antimicrobial agent: Applications and mode of action," *Biomacromolecules*, vol. 4, no. 6, pp. 1457–1465, 2003.

[31] Y.-J. Jeon, P.-J. Park, and S.-K. Kim, "Antimicrobial effect of chitooligosaccharides produced by bioreactor," *Carbohydrate Polymers*, vol. 44, no. 1, pp. 71–76, 2001.

[32] V. Tikhonov, E. Stepnova, V. Babak, I. Yamskov, J. Palma-Guerrero, H.-B. Jansson, L. Lopez-Llorca, J. Salinas, D. Gerasimenko, I. Avdienko, and V. Varlamov, "Bactericidal and antifungal activities of a low molecular weight chitosan and its n-/2(3)-(dodec-2-enyl)succinoyl/-derivatives," *Carbohydrate Polymers*, vol. 64, no. 1, pp. 66–72, 2006.

[33] S. Tokura, K. Ueno, S. Miyazaki, and N. Nishi, "Molecular weight dependent antimicrobial activity by chitosan," *Macromolecular Symposia*, vol. 120, pp. 1–9, 1997.

[34] T. Takahashi, M. Imai, I. Suzuki, and J. Sawai, "Growth inhibitory effect on bacteria of chitosan membranes regulated with deacetylation degree," *Biochemical Engineering Journal*, vol. 40, no. 3, pp. 485–491, 2008.

[35] N. Sudarshan, D. Hoover, and D. Knorr, "Antibacterial action of chitosan," *Food Biotechnology*, vol. 6, no. 3, pp. 257–272, 1992.

[36] M. Kong, X.-G. Chen, Y.-P. Xue, C.-S. Liu, L.-J. Yu, Q.-X. Ji, D. Cha, and H. Park, "Preparation and antibacterial activity of chitosan microshperes in a

solid dispersing system," *Frontiers of Materials Science in China*, vol. 2, no. 2, pp. 214–220, 2008.

[37] P. Dutta, J. Duta, and V. Tripathi, "Chitin and chitosan: Chemistry, properties and applications," *Journal of Scientific and Industrial Research*, vol. 63, no. 1, pp. 20–31, 2004.

[38] H. Yilmaz Atay, *Antibacterial Activity of Chitosan-Based Systems*, pp. 457–489. Singapore: Springer Singapore, 2019.

[39] M. Rinaudo, "Chitin and chitosan: Properties and applications," *Progress in Polymer Science*, vol. 31, no. 7, pp. 603–632, 2006.

[40] M. M. Mincea, M. Frandes, B. Timar, V. Ostafe, and C. Moraru, "A meta-analysis on randomised controlled clinical trials evaluating the effect of the dietary supplement chitosan on weight loss, lipid parameters and blood pressure," *Medicina.*, vol. 54, no. 6, p. 109, 2018.

[41] H. Eslami, P. Maroufi, F. Pakdel, S. Taghizadeh, E. Fakhri, K. Ganbarov, M. Yousefi, A. Tanomand, B. Yousefi, S. Mahmoudi, and H. S. Kafil, "Chitosan biomaterials application in dentistry," *International journal of biological macromolecules.*, vol. 162, pp. 956–974, 2020.

[42] Y. Luo and Q. Wang, "Recent advances of chitosan and its derivatives for novel applications in food science," *J Food Processing & Beverages*, vol. 1, no. 1, 2013.

[43] M. T. McDonnell, D. A. Greeley, K. M. Kit, and D. J. Keffer, "Molecular dynamics simulations of hydration effects on solvation, diffusivity, and permeability in chitosan/chitin films," *The journal of physical chemistry.*, vol. 120, no. 34, pp. 8997–9010, 2016.

[44] G. T. Beckham and M. F. Crowley, "Examination of the α-chitin structure and decrystallization thermodynamics at the nanoscale," *The Journal of Physical Chemistry B*, vol. 115, no. 15, pp. 4516–4522, 2011. PMID: 21452798.

[45] G. T. Beckham, J. F. Matthews, B. Peters, Y. J. Bomble, M. E. Himmel, and M. F. Crowley, "Molecular-level origins of biomass recalcitrance: Decrystallization free energies for four common cellulose polymorphs," *The Journal of Physical Chemistry B*, vol. 115, no. 14, pp. 4118–4127, 2011. PMID: 21425804.

[46] X. Ou, J. Zheng, X. Zhao, and M. Liu, "Chemically cross-linked chitin nanocrystal scaffolds for drug delivery," *ACS Applied Nano Materials*, vol. 1, no. 12, pp. 6790–6799, 2018.

[47] A. Ahmad, N. Mubarak, K. Naseem, H. Tabassum, M. Rizwan, A. Najda, M. Kashif, M. Bin-Jumah, A. Hussain, A. Shaheen, M. M. Abdel-Daim, S. Ali, and S. Hussain, "Recent advancement and development of chitin and chitosan-based nanocomposite for drug delivery: Critical approach to clinical research," *Arabian Journal of Chemistry*, vol. 13, no. 12, pp. 8935–8964, 2020.

[48] X. Ding, W. Yu, Y. Wan, M. Yang, C. Hua, N. Peng, and Y. Liu, "A ph/ros-responsive, tumor-targeted drug delivery system based on carboxymethyl chitin gated hollow mesoporous silica nanoparticles for anti-tumor chemotherapy," *Carbohydrate Polymers*, vol. 245, p. 116493, 2020.

[49] M. Liu, H. Zheng, J. Chen, S. Li, J. Huang, and C. Zhou, "Chitosan-chitin nanocrystal composite scaffolds for tissue engineering," *Carbohydrate Polymers*, vol. 152, pp. 832–840, 2016.

[50] S. Deepthi, J. Venkatesan, S.-K. Kim, J. D. Bumgardner, and R. Jayakumar, "An overview of chitin or chitosan/nano ceramic composite scaffolds for bone tissue engineering," *International Journal of Biological Macromolecules*, vol. 93, pp. 1338–1353, 2016. Biological Macromolecules for Tissue Regeneration.

[51] R. Jayakumar, R. Ramachandran, V. Divyarani, K. Chennazhi, H. Tamura, and S. Nair, "Fabrication of chitin–chitosan/nano tio2-composite scaffolds for tissue engineering applications," *International Journal of Biological Macromolecules*, vol. 48, no. 2, pp. 336–344, 2011.

[52] M. G. Mehrabani, R. Karimian, R. Rakhshaei, F. Pakdel, H. Eslami, V. Fakhrzadeh, M. Rahimi, R. Salehi, and H. S. Kafil, "Chitin/silk fibroin/-tio2 bio-nanocomposite as a biocompatible wound dressing bandage with strong antimicrobial activity," *International Journal of Biological Macromolecules*, vol. 116, pp. 966–976, 2018.

[53] R. A. Muzzarelli, P. Morganti, G. Morganti, P. Palombo, M. Palombo, G. Biagini, M. Mattioli Belmonte, F. Giantomassi, F. Orlandi, and C. Muzzarelli, "Chitin nanofibrils/chitosan glycolate composites as wound medicaments," *Carbohydrate Polymers*, vol. 70, no. 3, pp. 274–284, 2007.

[54] N. Naseri, C. Algan, V. Jacobs, M. John, K. Oksman, and A. P. Mathew, "Electrospun chitosan-based nanocomposite mats reinforced with chitin nanocrystals for wound dressing," *Carbohydrate Polymers*, vol. 109, pp. 7–15, 2014.

[55] G. Xia, Y. Liu, M. Tian, P. Gao, Z. Bao, X. Bai, X. Yu, X. Lang, S. Hu, and X. Chen, "Nanoparticles/thermosensitive hydrogel reinforced with chitin whiskers as a wound dressing for treating chronic wounds," *J. Mater. Chem. B*, vol. 5, pp. 3172–3185, 2017.

[56] H. Lee, M. H. Heo, H. Jeong, S. Y. Kim, J. S. Yuk, S. H. Park, and J. Shin, "Water-redispersible and high-yield α-chitin nanocrystals isolated using electron-beam irradiation as adsorbents to remove heavy metals and dye," *Nanoscale*, vol. 15, pp. 10990–11004, 2023.

[57] I. Anastopoulos, A. Bhatnagar, D. N. Bikiaris, and G. Z. Kyzas, "Chitin adsorbents for toxic metals: A review," *International Journal of Molecular Sciences*, vol. 18, no. 1, 2017.

[58] L. A. Goetz, B. Jalvo, R. Rosal, and A. P. Mathew, "Superhydrophilic anti-fouling electrospun cellulose acetate membranes coated with chitin nanocrystals for water filtration," *Journal of Membrane Science*, vol. 510, pp. 238–248, 2016.

[59] Y. Wang, L. Zhu, J. You, F. Chen, L. Zong, X. Yan, and C. Li, "Catecholic coating and silver hybridization of chitin nanocrystals for ultrafiltration membrane

with continuous flow catalysis and gold recovery," *ACS Sustainable Chemistry & Engineering*, vol. 5, no. 11, pp. 10673–10681, 2017.

[60] A. P. Mathew, M.-P. G. Laborie, and K. Oksman, "Cross-linked chitosan/chitin crystal nanocomposites with improved permeation selectivity and ph stability," *Biomacromolecules*, vol. 10, no. 6, pp. 1627–1632, 2009. PMID: 19388678.

[61] M. K. Patel, F. Hansson, O. Pitkänen, S. Geng, and K. Oksman, "Biopolymer blends of poly(lactic acid) and poly(hydroxybutyrate) and their functionalization with glycerol triacetate and chitin nanocrystals for food packaging applications," *ACS Applied Polymer Materials*, vol. 4, no. 9, pp. 6592–6601, 2022.

[62] C. C. Satam, C. W. Irvin, A. W. Lang, J. C. R. Jallorina, M. L. Shofner, J. R. Reynolds, and J. C. Meredith, "Spray-coated multilayer cellulose nanocrystal—chitin nanofiber films for barrier applications," *ACS Sustainable Chemistry & Engineering*, vol. 6, no. 8, pp. 10637–10644, 2018.

[63] M. R. Barkhordari and M. Fathi, "Production and characterization of chitin nanocrystals from prawn shell and their application for stabilization of pickering emulsions," *Food Hydrocolloids*, vol. 82, pp. 338–345, 2018.

[64] E. Perrin, H. Bizot, B. Cathala, and I. Capron, "Chitin nanocrystals for pickering high internal phase emulsions," *Biomacromolecules*, vol. 15, no. 10, pp. 3766–3771, 2014. PMID: 25180643.

[65] A. Bakhshian Nik, H. Zare, S. Razavi, H. Mohammadi, P. Torab Ahmadi, N. Yazdani, M. Bayandori, N. Rabiee, and J. Izadi Mobarakeh, "Smart drug delivery: Capping strategies for mesoporous silica nanoparticles," *Microporous and Mesoporous Materials*, vol. 299, p. 110115, 2020.

[66] D. Napierska, L. C. J. Thomassen, V. Rabolli, D. Lison, L. Gonzalez, M. Kirsch-Volders, J. A. Martens, and P. H. Hoet, "Size-dependent cytotoxicity of monodisperse silica nanoparticles in human endothelial cells," *Small*, vol. 5, no. 7, pp. 846–853, 2009.

[67] T. Liao, C. Liu, J. Ren, H. Chen, Y. Kuang, B. Jiang, J. Chen, Z. Sun, and C. Li, "A chitosan/mesoporous silica nanoparticle-based anticancer drug delivery system with a "tumor-triggered targeting" property," *International Journal of Biological Macromolecules*, vol. 183, pp. 2017–2029, 2021.

[68] C. Chen, W. Yao, W. Sun, T. Guo, H. Lv, X. Wang, H. Ying, Y. Wang, and P. Wang, "A self-targeting and controllable drug delivery system constituting mesoporous silica nanoparticles fabricated with a multi-stimuli responsive chitosan-based thin film layer," *International Journal of Biological Macromolecules*, vol. 122, pp. 1090–1099, 2019.

[69] F. Garavand, I. Cacciotti, N. Vahedikia, A. Rehman, Özgür Tarhan, S. Akbari-Alavijeh, R. Shaddel, A. Rashidinejad, M. Nejatian, S. Jafarzadeh, M. Azizi-Lalabadi, S. Khoshnoudi-Nia, and S. M. Jafari, "A comprehensive review on the nanocomposites loaded with chitosan nanoparticles for food packaging," *Critical Reviews in Food Science and Nutrition*, vol. 62, no. 5, pp. 1383–1416, 2022. PMID: 33153290.

[70] E. F. Franca, R. D. Lins, L. C. G. Freitas, and T. P. Straatsma, "Characterization of chitin and chitosan molecular structure in aqueous solution," *Journal of chemical theory and computation : JCTC.*, vol. 4, no. 12, pp. 2141–2149, 2008.

[71] E. F. Franca, L. C. G. Freitas, and R. D. Lins, "Chitosan molecular structure as a function of n-acetylation," *Biopolymers.*, vol. 95, no. 7, pp. 448–460, 2011.

[72] V. S. Naumov and S. K. Ignatov, "Modification of 56acarbo force field for molecular dynamic calculations of chitosan and its derivatives," *Journal of molecular modeling*, vol. 23, no. 8, 2017.

[73] V. S. Naumov and S. K. Ignatov, "Dissolution of chitosan nanocrystals in aqueous media of different acidity. molecular dynamic study," *Carbohydrate polymers.*, vol. 207, pp. 619–627, 2019.

[74] S. Mathesan, P. Ghosh, and A. Rath, "Folding behavior and molecular mechanism of cross-linked biopolymer film in response to water," *Soft matter.*, vol. 12, no. 45, pp. 9210–9222, 2016.

[75] J. Cui, Z. Yu, and D. Lau, "Effect of acetyl group on mechanical properties of chitin/chitosan nanocrystal: A molecular dynamics study," *International journal of molecular sciences.*, vol. 17, no. 1, p. 61, 2016.

[76] M. J. Abraham, T. Murtola, R. Schulz, S. Páll, J. C. Smith, B. Hess, and E. Lindahl, "Gromacs: High performance molecular simulations through multi-level parallelism from laptops to supercomputers," *SoftwareX*, vol. 1-2, pp. 19–25, 2015.

[77] J. C. Phillips, D. J. Hardy, J. D. C. Maia, J. E. Stone, J. V. Ribeiro, R. C. Bernardi, R. Buch, G. Fiorin, J. Hénin, W. Jiang, R. McGreevy, M. C. R. Melo, B. K. Radak, R. D. Skeel, A. Singharoy, Y. Wang, B. Roux, A. Aksimentiev, Z. Luthey-Schulten, L. V. Kalé, K. Schulten, C. Chipot, and E. Tajkhorshid, "Scalable molecular dynamics on cpu and gpu architectures with namd," *The Journal of Chemical Physics*, vol. 153, no. 4, p. 044130, 2020.

[78] A. D. Mackerell Jr., "Empirical force fields for biological macromolecules: Overview and issues," *Journal of Computational Chemistry*, vol. 25, no. 13, pp. 1584–1604, 2004.

[79] O. Guvench, S. S. Mallajosyula, E. P. Raman, E. Hatcher, K. Vanommeslaeghe, T. J. Foster, F. W. Jamison, and A. D. MacKerell, "Charmm additive all-atom force field for carbohydrate derivatives and its utility in polysaccharide and carbohydrate–protein modeling," *Journal of Chemical Theory and Computation*, vol. 7, no. 10, pp. 3162–3180, 2011.

[80] O. Guvench, E. Hatcher, R. M. Venable, R. W. Pastor, and A. D. MacKerell, "Charmm additive all-atom force field for glycosidic linkages between hexopyranoses," *Journal of Chemical Theory and Computation*, vol. 5, no. 9, pp. 2353–2370, 2009.

[81] E. P. Raman, O. Guvench, and A. D. MacKerell, "Charmm additive all-atom force field for glycosidic linkages in carbohydrates involving furanoses," *The Journal of Physical Chemistry B*, vol. 114, no. 40, pp. 12981–12994, 2010.

[82] K. Vanommeslaeghe, E. Hatcher, C. Acharya, S. Kundu, S. Zhong, J. Shim, E. Darian, O. Guvench, P. Lopes, I. Vorobyov, and A. D. Mackerell Jr., "Charmm general force field: A force field for drug-like molecules compatible with the charmm all-atom additive biological force fields," *Journal of Computational Chemistry*, vol. 31, no. 4, pp. 671–690, 2010.

[83] P. Bjelkmar, P. Larsson, M. A. Cuendet, B. Hess, and E. Lindahl, "Implementation of the charmm force field in gromacs: Analysis of protein stability effects from correction maps, virtual interaction sites, and water models," *Journal of Chemical Theory and Computation*, vol. 6, no. 2, pp. 459–466, 2010. PMID: 26617301.

[84] H. Heinz, T.-J. Lin, R. Kishore Mishra, and F. S. Emami, "Thermodynamically consistent force fields for the assembly of inorganic, organic, and biological nanostructures: The interface force field," *Langmuir*, vol. 29, no. 6, pp. 1754–1765, 2013. PMID: 23276161.

[85] H. A. Lorentz, "Ueber die anwendung des satzes vom virial in der kinetischen theorie der gase," *Annalen der Physik*, vol. 248, no. 1, pp. 127–136, 1881.

[86] D. Berthelot, "Sur le mélange des gaz," *Compt. Rendus*, vol. 126, no. 3, p. 15, 1898.

[87] W. L. Jorgensen, J. Chandrasekhar, J. D. Madura, R. W. Impey, and M. L. Klein, "Comparison of simple potential functions for simulating liquid water," *The Journal of Chemical Physics*, vol. 79, pp. 926–935, 07 1983.

[88] V. Ballenegger, "Communication: On the origin of the surface term in the Ewald formula," *The Journal of Chemical Physics*, vol. 140, p. 161102, 04 2014.

[89] M. Abraham, A. Alekseenko, C. Bergh, C. Blau, E. Briand, M. Doijade, S. Fleischmann, V. Gapsys, G. Garg, S. Gorelov, G. Gouaillardet, A. Gray, M. E. Irrgang, F. Jalalypour, J. Jordan, C. Junghans, P. Kanduri, S. Keller, C. Kutzner, J. A. Lemkul, M. Lundborg, P. Merz, V. Miletić, D. Morozov, S. Páll, R. Schulz, M. Shirts, A. Shvetsov, B. Soproni, D. van der Spoel, P. Turner, C. Uphoff, A. Villa, S. Wingbermühle, A. Zhmurov, P. Bauer, B. Hess, and E. Lindahl, "Gromacs 2023.1 manual," Apr. 2023.

[90] R. Hockney, S. Goel, and J. Eastwood, "Quiet high-resolution computer models of a plasma," *Journal of Computational Physics*, vol. 14, no. 2, pp. 148–158, 1974.

[91] J. C. Phillips, R. Braun, W. Wang, J. Gumbart, E. Tajkhorshid, E. Villa, C. Chipot, R. D. Skeel, L. Kalé, and K. Schulten, "Scalable molecular dynamics with namd," *Journal of Computational Chemistry*, vol. 26, no. 16, pp. 1781–1802, 2005.

[92] H. J. C. Berendsen, J. P. M. Postma, W. F. van Gunsteren, A. DiNola, and J. R. Haak, "Molecular dynamics with coupling to an external bath," *The Journal of Chemical Physics*, vol. 81, pp. 3684–3690, 10 1984.

[93] S. C. Harvey, R. K.-Z. Tan, and T. E. Cheatham III, "The flying ice cube: Velocity rescaling in molecular dynamics leads to violation of energy equipartition," *Journal of Computational Chemistry*, vol. 19, no. 7, pp. 726–740, 1998.

[94] W. G. Hoover, "Canonical dynamics: Equilibrium phase-space distributions," *Phys. Rev. A*, vol. 31, pp. 1695–1697, Mar 1985.

[95] M. Parrinello and A. Rahman, "Polymorphic transitions in single crystals: A new molecular dynamics method," *Journal of Applied Physics*, vol. 52, pp. 7182–7190, 12 1981.

[96] D. Quigley and M. I. J. Probert, "Langevin dynamics in constant pressure extended systems," *The Journal of Chemical Physics*, vol. 120, pp. 11432–11441, 06 2004.

[97] C. Jarzynski, "Nonequilibrium equality for free energy differences," *Phys. Rev. Lett.*, vol. 78, pp. 2690–2693, Apr 1997.

[98] J. Kästner, "Umbrella sampling," *Wiley Interdisciplinary Reviews: Computational Molecular Science*, vol. 1, no. 6, pp. 932–942, 2011.

[99] A. Grossfield, ""wham: the weighted histogram analysis method", version 2.0.11," 2021.

[100] S. Jo, T. Kim, V. G. Iyer, and W. Im, "Charmm-gui: A web-based graphical user interface for charmm," *Journal of Computational Chemistry*, vol. 29, no. 11, pp. 1859–1865, 2008.

[101] Y. K. Choi, N. R. Kern, S. Kim, K. Kanhaiya, Y. Afshar, S. H. Jeon, S. Jo, B. R. Brooks, J. Lee, E. B. Tadmor, H. Heinz, and W. Im, "Charmm-gui nanomaterial modeler for modeling and simulation of nanomaterial systems," *Journal of Chemical Theory and Computation*, vol. 18, no. 1, pp. 479–493, 2022. PMID: 34871001.

[102] F. S. Emami, V. Puddu, R. J. Berry, V. Varshney, S. V. Patwardhan, C. C. Perry, and H. Heinz, "Force field and a surface model database for silica to simulate interfacial properties in atomic resolution," *Chemistry of Materials*, vol. 26, no. 8, pp. 2647–2658, 2014.

[103] V. Bordoni, G. Fittolani, M. A. Chaube, A. Grafmueller, T. Tyrikos-Ergas, M. A. Chaube, A. Grafmüller, P. H. Seeberger, and M. Delbianco, "Systematic structural characterization of chitooligosaccharides enabled by automated glycan assembly," *Chemistry : a European journal.*, vol. 27, no. 7, pp. 2321–2325, 2021.

[104] S. Skovstrup, S. G. Hansen, T. Skrydstrup, and B. Schiøtt, "Conformational flexibility of chitosan: A molecular modeling study," *Biomacromolecules*, vol. 11, pp. 3196–3207, nov 2010.

[105] T. Tyrikos-Ergas, V. Bordoni, G. Fittolani, M. A. Chaube, A. Grafmüller, P. H. Seeberger, and M. Delbianco, "Systematic structural characterization of chi-

tooligosaccharides enabled by automated glycan assembly," *Chemistry – A European Journal*, vol. 27, no. 7, pp. 2321–2325, 2021.

[106] C. Schatz, C. Viton, T. Delair, C. Pichot, and A. Domard, "Typical physicochemical behaviors of chitosan in aqueous solution," *Biomacromolecules*, vol. 4, no. 3, pp. 641–648, 2003. PMID: 12741780.

[107] C.-C. Tsai, B. H. Morrow, W. Chen, G. F. Payne, and J. Shen, "Toward Understanding the Environmental Control of Hydrogel Film Properties: How Salt Modulates the Flexibility of Chitosan Chains," *MACROMOLECULES*, vol. 50, pp. 5946–5952, AUG 8 2017.

[108] D. M. Arvelo, J. Comer, J. Schmit, and R. Garcia, "Interfacial water is separated from a hydrophobic silica surface by a gap of 1.2 nm," *ACS Nano*, vol. 18, no. 28, pp. 18683–18692, 2024. PMID: 38973716.

[109] J. Lyklema, *Fundamentals of interface and colloid science.* Amsterdam ; London: Elsevier Academic Press, 1991.

[110] A. H. Brown, T. R. Walsh, A. H. Brown, and T. R. Walsh, "Elucidating the influence of polymorph-dependent interfacial solvent structuring at chitin surfaces," *Carbohydrate Polymers*, vol. 151, pp. 916–925, 2016.

[111] K. Kubiak-Ossowska and P. A. Mulheran, "Protein diffusion and long-term adsorption states at charged solid surfaces," *Langmuir*, vol. 28, no. 44, pp. 15577–15585, 2012. PMID: 23062108.

[112] L. Qian, K. Zhang, X. Guo, and M. Yu, "What happens when chitin becomes chitosan? a single-molecule study," *RSC Adv.*, vol. 13, pp. 2294–2300, 2023.

[113] M. Garg, M. Linares, and I. Zozoulenko, "Theoretical rationalization of self-assembly of cellulose nanocrystals: Effect of surface modifications and counterions," *Biomacromolecules*, vol. 21, no. 8, pp. 3069–3080, 2020. PMID: 32619090.

[114] M. Aouay, A. Magnin, J.-L. Putaux, and S. Boufi, "Biobased nucleation agents for poly-l-(lactic acid) — effect on crystallization, rheological and mechanical

properties," *International journal of biological macromolecules.*, vol. 218, pp. 588–600, 2022.

[115] X. Qian, "The effect of cooperativity on hydrogen bonding interactions in native cellulose iβ from ab initio molecular dynamics simulations," *Molecular simulation*, vol. 34, no. 2, pp. 183–191, 2008.

[116] Z. Střelcová, P. Kulhánek, M. Friák, H.-O. Fabritius, M. Petrov, J. Neugebauer, and J. Koča, "The structure and dynamics of chitin nanofibrils in an aqueous environment revealed by molecular dynamics simulations," *RSC Adv.*, vol. 6, pp. 30710–30721, 2016.

[117] K. Tokarczyk, K. Kubiak-Ossowska, B. Jachimska, and P. A. Mulheran, "Energy landscape of negatively charged bsa adsorbed on a negatively charged silica surface," *The Journal of Physical Chemistry B*, vol. 122, no. 14, pp. 3744–3753, 2018. PMID: 29536734.

[118] V. E. Yudin, I. P. Dobrovolskaya, I. M. Neelov, E. N. Dresvyanina, P. V. Popryadukhin, E. M. Ivan'kova, V. Y. Elokhovskii, I. A. Kasatkin, B. M. Okrugin, and P. Morganti, "Wet spinning of fibers made of chitosan and chitin nanofibrils," *Carbohydrate Polymers*, vol. 108, pp. 176–182, 2014.

[119] R. El Kurdi, M. Chebl, M. Sillanpää, H. El-Rassy, and D. Patra, "Chitosan oligosaccharide/silica nanoparticles hybrid porous gel for mercury adsorption and detection," *Materials Today Communications*, vol. 28, p. 102707, 2021.

[120] M. Gulfam, B. G. Chung, M. Gulfam, and B. G. Chung, "Development of ph-responsive chitosan-coated mesoporous silica nanoparticles," *Macromolecular research.*, vol. 22, no. 4, pp. 412–417, 2014.

[121] A. Tiraferri, P. Maroni, D. Caro Rodríguez, and M. Borkovec, "Mechanism of chitosan adsorption on silica from aqueous solutions," *Langmuir*, vol. 30, no. 17, pp. 4980–4988, 2014. PMID: 24725003.

[122] J. Matusiak, E. Grzadka, and A. Bastrzyk, "Stability, adsorption and electrokinetic properties of the chitosan/silica system," *Colloids and Surfaces A: Physicochemical and Engineering Aspects*, vol. 554, pp. 245–252, 2018.

[123] A. MacKerell, D. Bashford, M. Bellott, R. Dunbrack, J. Evanseck, M. Field, S. Fischer, J. Gao, H. Guo, S. Ha, D. Joseph-McCarthy, L. Kuchnir, K. Kuczera, F. Lau, C. Mattos, S. Michnick, T. Ngo, D. Nguyen, B. Prodhom, W. Reiher, B. Roux, M. Schlenkrich, J. Smith, R. Stote, J. Straub, M. Watanabe, J. Wiorkiewicz-Kuczera, D. Yin, and M. Karplus, "All-atom empirical potential for molecular modeling and dynamics studies of proteins," *JOURNAL OF PHYSICAL CHEMISTRY B*, vol. 102, pp. 3586–3616, APR 30 1998.

[124] M. Hudek, K. Kubiak-Ossowska, K. Johnston, V. A. Ferro, and P. A. Mulheran, "Chitin and chitosan binding to the α-chitin crystal: A molecular dynamics study," *ACS Omega*, vol. 8, no. 3, pp. 3470–3477, 2023.

[125] W. Humphrey, A. Dalke, and K. Schulten, "VMD – Visual Molecular Dynamics," *Journal of Molecular Graphics*, vol. 14, pp. 33–38, 1996.

[126] W. L. Jorgensen, J. Chandrasekhar, J. D. Madura, R. W. Impey, and M. L. Klein, "Comparison of simple potential functions for simulating liquid water," *The Journal of Chemical Physics*, vol. 79, no. 2, pp. 926–935, 1983.

[127] M. J. Abraham, T. Murtola, R. Schulz, S. Páll, J. C. Smith, B. Hess, and E. Lindahl, "Gromacs: High performance molecular simulations through multi-level parallelism from laptops to supercomputers," *SoftwareX*, vol. 1, 9 2015.

[128] M. R. Shirts, C. Klein, J. M. Swails, J. Yin, M. K. Gilson, D. L. Mobley, D. A. Case, and E. D. Zhong, "Lessons learned from comparing molecular dynamics engines on the sampl5 dataset," *Journal of Computer-Aided Molecular Design*, vol. 31, pp. 147–161, Jan 2017.

[129] Richard J. Gowers, Max Linke, Jonathan Barnoud, Tyler J. E. Reddy, Manuel N. Melo, Sean L. Seyler, Jan Domański, David L. Dotson, Sébastien Buchoux, Ian

M. Kenney, and Oliver Beckstein, "MDAnalysis: A Python Package for the Rapid Analysis of Molecular Dynamics Simulations," in *Proceedings of the 15th Python in Science Conference* (Sebastian Benthall and Scott Rostrup, eds.), pp. 98 – 105, 2016.

[130] T. Williams, C. Kelley, and many others, "Gnuplot 5.4: an interactive plotting program." `http://gnuplot.info/`, July 2022.

[131] J. S. Hub, B. L. de Groot, and D. van der Spoel, "g_wham—a free weighted histogram analysis implementation including robust error and autocorrelation estimates," *Journal of Chemical Theory and Computation*, vol. 6, no. 12, pp. 3713–3720, 2010.

[132] M. Nategholeslam, C. G. Gray, and B. Tomberli, "Stiff spring approximation revisited: Inertial effects in nonequilibrium trajectories," *The Journal of Physical Chemistry B*, vol. 121, no. 2, pp. 391–403, 2017. PMID: 27959538.

[133] S. Prochazkova, K. M. Vårum, and K. Ostgaard, "Quantitative determination of chitosans by ninhydrin," *Carbohydrate polymers*, vol. 38, no. 2, pp. 115–122, 1999.

[134] B. Alberts, *Molecular Biology of the Cell [internet resource]*. Oxford: Taylor and Francis, 6th ed.. ed., 2014.

[135] J. W. Bartholomew and T. Mittwer, "The gram stain," *Bacteriological reviews*, vol. 16, no. 1, pp. 1–29, 1952.

[136] S. Y. C. Tong, J. S. Davis, E. Eichenberger, T. L. Holland, and V. G. Fowler, "Staphylococcus aureus infections: Epidemiology, pathophysiology, clinical manifestations, and management," *Clinical Microbiology Reviews*, vol. 28, no. 3, pp. 603–661, 2015.

[137] R. L. Vogt and L. Dippold, "Escherichia coli o157:h7 outbreak associated with consumption of ground beef, june–july 2002," *Public Health Reports®*, vol. 120, no. 2, pp. 174–178, 2005. PMID: 15842119.

[138] J. Sun, S. T. Rutherford, T. J. Silhavy, and K. C. Huang, "Physical properties of the bacterial outer membrane," *Nature reviews. Microbiology*, vol. 20, p. 236—248, April 2022.

[139] E. L. Wu, X. Cheng, S. Jo, H. Rui, K. C. Song, E. M. Dávila-Contreras, Y. Qi, J. Lee, V. Monje-Galvan, R. M. Venable, J. B. Klauda, and W. Im, "Charmm-gui membrane builder toward realistic biological membrane simulations," *Journal of Computational Chemistry*, vol. 35, no. 27, pp. 1997–2004, 2014.

[140] M. P. Bos, V. Robert, and J. Tommassen, "Biogenesis of the gram-negative bacterial outer membrane," *Annu. Rev. Microbiol.*, vol. 61, no. 1, pp. 191–214, 2007.

[141] A. Boyd and I. Holland, "Regulation of the synthesis of surface protein in the cell cycle of e. coli b/r," *Cell*, vol. 18, no. 2, pp. 287–296, 1979.

[142] R. Koebnik, K. P. Locher, and P. Van Gelder, "Structure and function of bacterial outer membrane proteins: barrels in a nutshell," *Molecular Microbiology*, vol. 37, no. 2, pp. 239–253, 2000.

[143] S. Jarosławski, K. Duquesne, J. N. Sturgis, and S. Scheuring, "High-resolution architecture of the outer membrane of the gram-negative bacteria roseobacter denitrificans," *Molecular Microbiology*, vol. 74, no. 5, pp. 1211–1222, 2009.

[144] M. Yang, A. S. Jalloh, W. Wei, J. Zhao, P. Wu, and P. R. Chen, "Biocompatible click chemistry enabled compartment-specific ph measurement inside ¡i¿e-coli¡/i¿," *NATURE COMMUNICATIONS*, vol. 5, SEP 2014.

[145] J. M. Benarroch and M. Asally, "The microbiologist's guide to membrane potential dynamics.," *Trends in microbiology*, 2020.

[146] J.-y. Zhu, Z.-y. Ma, M. Xiao, L.-s. Wang, and X.-k. Jiang, "Molecular dynamics simulations of the interaction between chitosan and bacterial membranes," *PROGRESS IN BIOCHEMISTRY AND BIOPHYSICS*, vol. 50, no. 8, pp. 1995–2005, 2023.

[147] G. K. Truong and M. Yi, "Molecular dynamics simulation studies of the effects of the protonation state of chitosan in interactions with bacterial membranes," *Korean Journal of Fisheries and Aquatic Sciences*, vol. 49, pp. 815–822, 12 2016.

[148] D. Atila, A. D. Dalgic, A. Krzeminska, J. Pietrasik, E. Gendaszewska-Darmach, D. Bociaga, M. Lipinska, F. Laoutid, J. Passion, V. Kumaravel, D. Atila, A. D. Dalgic, A. Krzemińska, J. Pietrasik, E. Gendaszewska-Darmach, D. Bociaga, M. Lipinska, F. Laoutid, J. Passion, and V. Kumaravel, "Injectable liposome-loaded hydrogel formulations with controlled release of curcumin and α -tocopherol for dental tissue engineering," *Advanced healthcare materials.*, 2024.

[149] S. Jo, T. Kim, V. G. Iyer, and W. Im, "Charmm-gui: A web-based graphical user interface for charmm," *Journal of Computational Chemistry*, vol. 29, no. 11, pp. 1859–1865, 2008.

[150] I. D. Pogozheva, G. A. Armstrong, L. Kong, T. J. Hartnagel, C. A. Carpino, S. E. Gee, D. M. Picarello, A. S. Rubin, J. Lee, S. Park, A. L. Lomize, and W. Im, "Comparative molecular dynamics simulation studies of realistic eukaryotic, prokaryotic, and archaeal membranes," *Journal of Chemical Information and Modeling*, vol. 62, no. 4, pp. 1036–1051, 2022. PMID: 35167752.

[151] H. Liu, Y. Du, X. Wang, and L. Sun, "Chitosan kills bacteria through cell membrane damage," *International Journal of Food Microbiology*, vol. 95, no. 2, pp. 147–155, 2004.

Appendix A

Inputs and Code availability

The data underpinning the research presented in chapters submitted for publication is freely at the University of Strathclyde Knowledgebase at:

- **Chapter 4**: https://doi.org/10.15129/4efcf3ae-4e00-4b66-b27c-407668d8fd01.
- **Chapter 5**: https://doi.org/10.15129/95d72512-3f2b-4b64-8163-d60c5842de89

The scripts developed for the research presented in this thesis are available at a public GitHub repository: https://github.com/mhudek/MD_utilities and the most used ones are listed here (A.1-A.4),

The inputs for **chapters 3** and **4** are given in A.5-A.7, **chapter 5** A.8-A.10 and **chapter 6** A.9-A.17.

Listings

A.1 Tcl Scripts

Listing A.1: h-bonds.tcl

```
#get h-bonds for each frame of the simulation
set outfile [open h_bonds_custom.txt w]
```

```
set n [molinfo top get numframes]
set sel1 [atomselect top {selection]
puts $outfile "FRAME, DONOR, HYDROGEN, ACCEPTOR"
for {set i 1} {$i < $n} {inc i} {
    puts "current frame: $i"
    #set sel1 [atomselect top "fragment 2" frame $i]
    #set sel2 [atomselect top "fragment 36" frame $i]
    $sel1 frame $i
    $sel1 update
    #$sel2 frame $i
    #$sel1 update
    set hb [measure hbonds 3.5 30 $sel1]
    foreach {donor acceptor hydrogen} $hb { break }
    set n_bonds [llength $donor]
    for {set j 1} {$j < $n_bonds} {inc j} {
        set line "$i, [lindex $donor $j], [lindex $hydrogen $j], \
  [lindex $acceptor $j]"
        puts $outfile $line
    }
}
close $outfile
```

Listing A.2: align-membrane.tcl

```
# align_memb.tcl
#
#Usage: vglrun vmd -dispdev text -e align_memb.tcl
#Align the lipid bilayer with respect to z=0 positon
#Warning: always keep original trajectory on tape
#The input trajectory should be wrapped
#i.e. all atoms within unit cell and no bonds accross
#periodic boundary
#Upper and lower leafler selections need to be input manually!
#
#Author: magalena.hudek@strath.ac.uk
#Load required packages
package require pbctools

#Define input names here
set in_psf "step5_input.psf"
set in_dcd "test_out.dcd"
set out_dcd "test_aligned.dcd"

set memb_sel "segname MEMB"

proc align { sel {refframe 0} } {

  #set over estimate of membrane thickness
  #used to detect if membrane is split only
  set memb_thickness 75
  #string selection for lower and upper leaflet
  set low_l "segname MEMB and resid 113 to 212"
```

```
29  set upp_l "segname MEMB and resid 0 to 112"
30
31  set frames [molinfo top get numframes]
32  set all [atomselect top all]
33  set comsel [atomselect top ($sel) frame $refframe]
34
35  ###DEFINE LEAFLETS HERE!
36  set lower_leaflet [atomselect top $low_l]
37  set upper_leaflet [atomselect top $upp_l]
38  #set reference centre-of-mass
39  set ref_com {0 0 0}
40
41  #Loop through all the frames
42  for {set i 0} {$i < $frames} {incr i} {
43
44    #Get pbc
45    set box [pbc get -first $i -last $i]
46        set boxx [split $box]
47        set c [lindex $boxx 2]
48
49    $all frame $i
50    $all update
51    $comsel frame $i
52    $comsel update
53
54    set com [measure center $all]
55        set i_shift [vecsub $ref_com $com]
56        $all moveby $i_shift
57
58    $lower_leaflet frame $i
59    $lower_leaflet update
60
61    $upper_leaflet frame $i
62    $upper_leaflet update
63
64
65    set minmax [measure minmax $comsel]
66    foreach {min max} $minmax { break }
67        foreach {xmin ymin zmin} $min { break }
68        foreach {xmax ymax zmax} $max { break }
69    set t [expr $zmax-$zmin]
70
71    if {[expr $t > $memb_thickness]} {
72        #puts "Split membrane"
73        #check if upper leaflet is split
74        set minmax [measure minmax $upper_leaflet]
75            foreach {min max} $minmax { break }
76            foreach {xmin ymin zmin} $min { break }
77            foreach {xmax ymax zmax} $max { break }
78            set t [expr $zmax-$zmin]
79        if {[expr abs($t) > $memb_thickness]} {
80            #puts "Upper leaflet is split"
81            set split_low [atomselect top "same \
82   fragment as ($upp_l  and z < [expr -$c/2])" frame $i]
```

```
            $split_low moveby [list 0 0 $c]
            }

        #check if lower leaflet is split
        set minmax [measure minmax $lower_leaflet]
                foreach {min max} $minmax { break }
                foreach {xmin ymin zmin} $min { break }
                foreach {xmax ymax zmax} $max { break }
                set t [expr $zmax-$zmin]
        if {[expr abs($t) > $memb_thickness]} {
                        #puts "Lower leaflet is split"
                        set split_low [atomselect \
                        top "same fragment as \
            ($low_l and z > [expr $c/2])" frame $i]
                        $split_low moveby [list 0 0 [expr -1* $c
                           ]]
                        }

        #check if membrane is still split
        set minmax [measure minmax $comsel]
            foreach {min max} $minmax { break }
            foreach {xmin ymin zmin} $min { break }
            foreach {xmax ymax zmax} $max { break }
            set t [expr $zmax-$zmin]
        if {[expr abs($t) > $memb_thickness]} {
            #puts "Membrane is still split,
                        #but leaflets should be whole"
            set lower_box [atomselect top \
  "same fragment as z < 0" frame $i]
                    $lower_box moveby [list 0 0 $c]
        }
    }

    #check for anything thats not water ions or solvent
        #outside of box and put it back if com outside the box
    set etop [atomselect top "same segname as \
((resname SDP) and z > [expr $c/2])" frame $i]
        if { [$etop num] > 0} {
                set com_top [measure center $etop]
                if {[lindex $com_top 2] > [expr $c/2-5] } {
                    puts "Found CHITOSAN on the top"
                    $etop moveby [list 0 0 [expr -1*$c]]
                }
        }

    $all update
    $lower_leaflet update
    $upper_leaflet update

    set upper_com [measure center $upper_leaflet ]
        set lower_com [measure center $lower_leaflet ]
        set leaf_distZ [lindex [vecsub $upper_com $lower_com] 2]

    if {$leaf_distZ > [expr $c*0.66] } {
```

```
        puts "SPLIT MEMBRANE FOUND"
        set lower_box [atomselect top \
  "same fragment as z < 0" frame $i]
        $lower_box moveby [list 0 0 $c]
    }

    $comsel update
    set com [measure center $comsel]
    #align membrane to ref_com
    set shift [vecsub $ref_com $com]
    $all moveby $shift
    $all update
    #center solvent around the membrane
    set over_pbc [atomselect top "same fragment \
 as ((all not $sel) and z > [expr $c/2])" frame $i]
    $over_pbc moveby [list 0 0 [expr -1*$c]]
    set under_pbc [atomselect top "same fragment \
 as ((all not $sel) and z < [expr $c/-2])" frame $i]
        $under_pbc moveby [list 0 0 $c]
    # check for anything thats not water ions
    # or solvent outside of box and put it
    # back if com outside the box
        set etop [atomselect top "same segname \
        as (resname SDP) and z > [expr $c/2]" frame $i]
        if { [$etop num] > 0} {
                set com_top [measure center $etop]
                if {[lindex $com_top 2] > [expr $c/2-5] } {
                        puts "Found CHITOSAN on the top"
                        $etop moveby [list 0 0 [expr -1*$c]]
                }
        }
  }
}

#Main part
mol new $in_psf
mol addfile $in_dcd waitfor all
align $memb_sel
animate write dcd $out_dcd

quit
```

A.2 Python Scripts

Listing A.3: analyse-hbonds.py

```
import pandas as pd
import numpy as np

import matplotlib.pyplot as plt
```

```
import matplotlib as mpl
import matplotlib.colors as colors


#H-bonds array produced by measure_h_bonds.tcl script in VMD
df = pd.read_csv("./h_bonds_custom.txt")
#array with index, atom_name, resname and resid of all
#donors and acceptors
names = pd.read_csv("./names.txt")

#identify unique hydrogen bonds
hbond_types = df.drop_duplicates([' DONOR', ' ACCEPTOR'], \
keep='first')

#get the number of frames for the simulation
num_frames = df['FRAME'].max()

#make dictionary so we can lookup nanes, resnames ...
id2types = names[['ID',' resname']].set_index('ID').T.to_dict('
    list')
id2name = names[['ID',' name']].set_index('ID').T.to_dict('list')
id2resid = names[['ID',' resid']].set_index('ID').T.to_dict('list
    ')

#identify bonds between silica & chitosan
#and create a name for each bond
d = []
for idx, row in hbond_types.iterrows():
    d_index = row[' DONOR']
    a_index = row[' ACCEPTOR']
    d_type = id2types[d_index]
    a_type = id2types[a_index]
    if str(a_type[0]) != str(d_type[0]):
        an = id2name[row[' ACCEPTOR']]
        dn = id2name[row[' DONOR']]
        arid = id2resid[row[' ACCEPTOR']]
        drid = id2resid[row[' DONOR']]
        name = str(str(dn[0])+str("(")+str(drid[0])+str(")")+
        str(an[0]) + str("(")+str(arid[0])+str(")"))
        d.append(( d_index, a_index, name ))

hbonds_cht_si = pd.DataFrame(d, columns=(' DONOR', ' ACCEPTOR', '
    NAME'))

# Create the array for plotting.

#place holder list for map
m = []
#place holder list for bond names
n = []
for idx, row in hbonds_cht_si.iterrows():
    p = df.loc[(df[' DONOR'] == row[' DONOR'])]
    p = p.loc[(df[' ACCEPTOR'] == row[ ' ACCEPTOR'])]
    if p.shape[0] > 1:
```

```
    # show only bonds with more
    #than x number of frames
        temp = np.zeros(num_frames)
        n.append(row['NAME'])
        for idx, row in p.iterrows():
            temp[row['FRAME']] = 1
        m.append(temp)
m = np.array(m)


frame = m
#plotting part
################################################

fig, ax = plt.subplots()
cmap = colors.ListedColormap(['white', 'black'])

plt.yticks(np.arange(0,len(n)), n)

#x = [0, 500, 1000, 1500, 2000, 2500, 3000, 3500, 4000]
#xticks = [0, 1, 2, 3,  4, 5, 6, 7, 8]
#plt.xticks(x, xticks)
#plt.xlabel("Time (ns)")

cax=plt.imshow(frame,origin='lower',filternorm=False,\
aspect='auto', cmap=cmap, interpolation='nearest')

#plot xlines where h-bonds break
#for k in range(len(frame)):
#    x = np.max( np.nonzero(frame[k,:]))
#    plt.plot([ x, x], [-0.5, 9.5], color='red', linewidth=1)
#    print(x*2)

cbar = fig.colorbar(cax, ticks=[0.25, 0.75],shrink=1,aspect=20)
boundaries = [ 0, 1]
norm = colors.BoundaryNorm(boundaries, cmap.N, clip=True)
cbar.ax.set_yticklabels(['no bond', 'bond'])
```

Listing A.4: generate-chain.py

```
#!/usr/bin/env python3

"""
This script creates a chitosan molecule chain compatible with
GROMOS 56Acarbo force field developed by Naumov & Ignatov
Citation: Naumov, V.S. & Ignatov, S.K. Modification of 56ACARBO
force field for molecular dynamic calculations of chitosan and
its derivatives  // J Mol Model (2017) 23: 244.

The script needs to be accompanied with .gro files in the same
directorty which contain residue coordinates with C1 atom
positioned at (0,0,0).

```

```
Output file is 'data.pdb' by default.

Added pdb format
"""

"""
Import basic modules
"""
import sys
import os
import io
import timeit
from timeit import default_timer as timer

start_time = timer()

"""
Try to import numpy; if failed, import a local version mynumpy
which needs to be provided
"""
try:
    import numpy as np
except:
    print("numpy not found. Exiting.")
    sys.exit(1)

gro_to_charm = {'CHT' : 'SDN', 'CHTO' : 'SDN', \
'CHTP' : 'SDP', 'CHTN' : 'SDN', 'ACE' : 'BGL'}

def rotate(n,v):
    '''rotate vector, v around vector n by 180 deg'''
    R = np.array([[2*n[0]**2-1, 2*n[0]*n[1], 2*n[0]*n[2]], \
                  [2*n[0]*n[1], 2*n[1]**2-1, 2*n[1]*n[2]], \
                  [2*n[0]*n[2], 2*n[1]*n[2], 2*n[2]**2-1]])
    out = np.dot(R,v)
    return out

def zrotate_ang(v, theta):
    '''rotate vector, v theta degrees around z-axis'''
    theta = np.deg2rad(theta)

    R = np.array([[np.cos(theta), -np.sin(theta), 0],
    \[np.sin(theta),np.cos(theta), 0],[0, 0, 1]])
    v = np.array(v)
    out = np.dot(R,v)
    return out


def zrotate(v):
    '''rotate vector, v 180 degrees around z-axis'''
    R = np.array([[-1, 0, 0], [0,-1, 0],[0, 0, 1]])
    v = np.array(v)
    out = np.dot(R,v)
    return out
```

```
68
69  def read_monomer(res):
70      '''read individual monomers from the working directory'''
71      res_input = str(res) + ".gro"
72      read_residue = open(res_input,'r')
73      n = 0
74      x, y, z = [], [], []
75      atom_id, atom_name = [], []
76      atom_type, charm_name = [], []
77      lines = read_residue.readlines()
78      for line in lines:
79          list1 = line.split()
80          if len(list1) != 9:
81              continue
82          else:
83              atom_name.append(list1[2])
84              atom_id.append(list1[3])
85              x.append(list1[4])
86              y.append(list1[5])
87              z.append(list1[6])
88              atom_type.append(list1[7])
89              charm_name.append(list1[8])
90
91              n += 1
92
93      return(atom_name, atom_id, x, y, z, atom_type, charm_name, n)
94
95  def create_polymer(res_id, res_name, a_name,\
96  a_id, x, y, z, a_type, charm_n ):
97      '''correct atom postions and residue ids to create a polymer
            '''
98      max_res = int(res_id[-1])
99      n = np.zeros((max_res,3))
100     #from gromos unit to charm units
101     mul = 10.0
102
103     for i in range( len(x)):
104         if res_id[i] == 1:
105
106             x[i], y[i], z[i] = float(x[i]), float(y[i]), float(z[
                    i])
107             x[i] = mul * x[i]
108             y[i] = mul * y[i]
109             z[i] = mul * z[i]
110
111         else:
112             # correct atom_id
113             a_id[i] = str(i+1)
114             u = np.array([ float(x[i]), float(y[i]), float(z[i])
                    ])
115
116             #rotate every second monomer by 180 deg around z-axis
117             if res_id[i]%2 == 0:
118                 u = zrotate(u)
```

```
119             # translation vector - distance O4 - O1
120             t = np.array([ 0, 0, -0.52178])
121 
122             #calculate new coordinates
123             v = (res_id[i]-1)*t
124             v = v + u
125 
126             x[i], y[i], z[i] = v[0], v[1], v[2]
127             x[i] = mul * x[i]
128             y[i] = mul * y[i]
129             z[i] = mul * z[i]
130 
131     return(res_id, res_name, a_name, a_id,\
132     x, y, z, a_type, charm_n)
133 
134 def create_crystal(res_id, res_name, a_name, \
135 a_id, x, y, z, a_type, charm_n):
136     """
137     Create chain by duplicating created polymer
138     """
139     # number of chains in x and y directions
140     a = 6
141     b = 3
142     xs, ys, zs = [], [], []
143 
144 
145     res_ids, res_names = [], []
146     a_names, a_ids = [], []
147     a_types, charm_ns = [], []
148 
149     #tilt of the chain with respect to the z-axis
150     theta = 7.5
151     dx = 4.85
152     dy = 9.26
153     i,j = 0, 0
154     n = 0
155 
156 
157     #duplicate chains to the number of
158     # chains required for the crystal
159     while i < a:
160         j = 0
161         while j < b:
162 
163 
164             k = 0
165             while k <len (x):
166                 u = np.zeros(3)
167                 u[0], u[1], u[2]  = float(x[k]), float(y[k]),
                        float(z[k])
168                 u = zrotate_ang(u, theta)
169                 u[0] = u[0] + dx*i
170                 u[1] = u[1] + dy*j
171 
```

```
172
173                 f, d, c = u[0], u[1], u[2]
174
175                 xs.append(f)
176                 ys.append(d)
177                 zs.append(c)
178
179                 k+= 1
180             for r_id in res_id:
181                 res_ids.append(r_id+n*res_id[-1])
182             for a_i in a_id:
183                 a_ids.append( str (int(a_i)+(n*int(a_id[-1]))))
184             for a_n in a_name:
185                 a_names.append(a_n)
186             for r_n in res_name:
187                 res_names.append(r_n)
188             for a_t in a_type:
189                 a_types.append(a_t)
190             for c_n in charm_n:
191                 charm_ns.append(c_n)
192
193             n +=1
194             j +=1
195         i+=1
196
197
198     return(res_ids, res_names, a_names, \
199     a_ids, xs, ys,zs, a_types, charm_ns)
200
201
202
203
204 def read_structure():
205     """
206     Main function for this script.
207     Reads a text file with the following format:
208     CHT0 CHT CHTP CHTN
209     every line must begin with CHT0 and end with CHTN
210     """
211     try:
212         #infile = open(sys.argv[1],'r')
213         infile = open("input")
214     except:
215         print("Could not open file {:s}. Aborting.".format(infile
            ))
216         sys.exit(2)
217
218     #Read in the monemers and see how many polymers
219     nmonomeres, nchains = 0, 0
220     count = 0
221     strandnum = []
222     restype = []
223     lines = infile.readlines()
224     #read file to polymer length and number of chains
```

```
    for line in lines:
        line = line.upper()
        if len(line) == 0:
            continue
        else:
            line = line.split()
            length = len(line)
            nmonomeres += length
            nchains += 1

    # rewind the sequence input file
    infile.seek(0)

    #generate the data file in GROMACS format
    try:
        #out = open("data.gro", "w+")
        out = open("data.pdb", "w+")
    except:
        print("Could not open data file for writing. Aborting.",\
                file=sys.stderr)
        sys.exit(2)

    lines = infile.readlines()
    nlines = len(lines)

    chainnum = 0

    xs, ys, zs = [], [], []
    counter = 0
    res_id, res_name  = [], []
    a_ids, els, a_names = [], [], []
    a_types, charm_ns = [], []
    for line in lines:
        line = line.upper()

        # skip empty lines
        if len(line) == 0:
            continue

        else:
            res = line.split()
            length = len(res)
            print("Found " + str(length) + " monomers." )

            #loop over residues
            for b in range(length):
                #print("b = " + str(b))
                restype.append(res[b])
                strandnum.append(chainnum)
                a_name, a_id, x, y, z, a_type, \
                charm_n, n = read_monomer(res[b])
                #print( "n = " + str(n))
                #loop over atoms in residues
                for c in range(n):
```

```
                    res_id.append(b+1)
                    res_name.append(res[b])
                    xs.append(x[c])
                    ys.append(y[c])
                    zs.append(z[c])
                    a_ids.append(a_id[c])
                    a_names.append(a_name[c])
                    a_types.append(a_type[c])
                    charm_ns.append(charm_n[c])
                count += n

    size = len(xs)

    #create polymer
    res_id, res_name, a_name, a_id, x, y, z, a_type, charm_n = \
            create_polymer(res_id, res_name, a_names, \
            a_ids, xs, ys, zs, a_types, charm_ns)


    res_id, res_name, a_name, a_id,\
    x, y, z, a_type, charm_n = \
        create_crystal(res_id, res_name, a_name, \
        a_id, x, y, z, a_type, charm_n)

    #test if nested arrays
    print("a_id " + str(a_id[0]) + " type" + str(type(a_id[0]))\
    + "expect str")
    print("charm_n: " + str(charm_n[0]) + "type: " \
    + str(type(charm_n[0])) + "exp str")
    print("fake ACE")
    print("res_name: " + str (res_name[0]) + " type: " \
    + str(type(res_name[0])))
    print("res_id: " + str(res_id[0]) + " type: " \
    + str(type(res_id[0])) + " exp int")

    print("a_name: " + str(a_name[0]) + "t ype: " \
    + str(type(a_name[0])))

    print("x " + str(x[0]) + "type" + str(type(x[0])))
    print("y " + str(y[0]))
    print("z " + str(z[0]))
    print("a_type: " + str(a_type[0]))


    count = count*18
    #sanity check
    if size != count:
        print('Warning! Numbers do not match')
        print("Size should be " + str(size) + ", but I count " +
            str(count))

    """
    gromacs output format
```

```
    out.write('!comment \n')
    out.write( str(count) + '\n')

    for j in range(count):
        # create .gro output format
        # res_num, res_name, atom_name, atom_num, x, y, z
        s = '{:>5d} {:>4s} {:>4s} {:>4s} {:>7.3f} {:>7.3f}\
        {:>7.3f}'.format(res_id[j], res_name[j], \
              a_name[j],a_id[j], x[j], y[j], z[j])
        out.write(s)
        out.write("\n")

    #dummy box size - later corrected with gromacs preprocessing
    out.write("10 10 10 \n")
    out.close()
    """

    #pdb output format
    out.write("REMARK generated using generate_cht.py script \n")
    s1 = 'ATOM   '

    for j in range(count):
        res_name[j] = gro_to_charm[res_name[j]]
        s2 = '{:>4s}  {:<4s}{:>3s} {:1s} {:>3d}    \
        {:>8.3f}{:>8.3f}{:>8.3f}{:>21s}{:>3s}'.\
            format(a_id[j], charm_n[j],res_name[j], 'A',res_id[j
               ],x[j],y[j],z[j],'CHT',a_type[j])
        s = s1 + s2 + '\n'
        out.write(s)

    out.write('END\n')
    out.close()

# call the above main() function, which executes the program
read_structure()

end_time=timer()
runtime = end_time-start_time
hours = runtime/3600
minutes = (runtime-np.rint(hours)*3600)/60
seconds = (runtime-np.rint(hours)*3600-np.rint(minutes)*60)%60
print("## Total runtime %ih:%im:%.2fs" % \
(hours,minutes,seconds), file=sys.stdout)
```

A.3 NAMD Inputs for Chapters 3 and 4

Listing A.5: D0.inp

```
structure       cht_sc.psf
coordinates     cht_sc.pdb
```

```
3
4  paratypecharmm  on
5  parameters      par_all36_carb.prm
6  parameters      par_glucosamine.rtf
7  parameters  par_cht_cgenff.prm
8  parameters      water.prm
9  exclude         scaled1-4
10 1-4scaling      1.0
11
12 switching       on
13 switchdist      8
14 cutoff          12
15 pairlistdist    14
16 margin          4
17 stepspercycle   20
18
19 wrapWater       on
20 rigidBonds      water
21
22 timestep 1.0
23
24 outputenergies  100
25 outputtiming    100
26 binaryoutput    yes
27 outputname      CHT_PME_D0
28 dcdfreq         100
29
30 temperature     300
31
32 langevin            on
33 langevinDamping     5
34 langevinTemp        300
35 langevinHydrogen    no
36
37 useFlexibleCell         yes
38 useGroupPressure        yes
39
40 LangevinPiston          on
41 LangevinPistonTarget    1.01325
42 LangevinPistonPeriod    200
43 LangevinPistonDecay     100
44 LangevinPistonTemp      300
45
46 PME             yes
47 PMEGridSpacing  1.0
48
49 cellBasisVector1     53.34000015258789   0.0     0.0
50 cellBasisVector2     0.0     60.08000183105469   0.0
51 cellBasisVector3     0.0     0.0     100.44900512695313
52 cellOrigin           0.0     0.0     0.0
53
54 fixedAtoms      on
55 fixedAtomsFile  fix_cht.pdb
56 fixedAtomsCol   O
```

```
57
58 minimize 1000
59 run 100000
```

Listing A.6: D1.inp

```
1  structure        cht_sc.psf
2  coordinates      cht_sc.pdb
3  bincoordinates   CHT_PME_D0.coor
4
5  paratypecharmm   on
6  parameters       par_all36_carb.prm
7  parameters       par_glucosamine.rtf
8  parameters   par_cht_cgenff.prm
9  parameters       water.prm
10
11 exclude          scaled1-4
12 1-4scaling       1.0
13
14 switching        on
15 switchdist       8
16 cutoff           12
17 pairlistdist     14
18 margin           0
19 stepspercycle    20
20
21 wrapWater        on
22 wrapAll          on
23 rigidBonds       water
24
25 timestep 1.0
26
27 PME              yes
28 PMEGridSpacing   1.0
29
30 outputenergies   100
31 outputtiming     100
32 binaryoutput     yes
33 outputname       CHT_PME_D1
34 dcdfreq          100
35
36 temperature      300
37
38 useFlexibleCell          yes
39 useGroupPressure         yes
40
41 LangevinPiston           on
42 LangevinPistonTarget     1.01325
43 LangevinPistonPeriod     200
44 LangevinPistonDecay      100
45 LangevinPistonTemp       300
46
47 extendedSystem       CHT_PME_D0.xsc
```

```
48
49 minimize            10000
50 run                 300000
```

Listing A.7: D2.inp

```
1  structure        cht_sc.psf
2  coordinates      cht_sc.pdb
3  bincoordinates   CHT_PME_D1.coor
4
5  paratypecharmm   on
6  parameters       par_all36_carb.prm
7  parameters       par_glucosamine.rtf
8  parameters   par_cht_cgenff.prm
9  parameters       water.prm
10
11 exclude          scaled1-4
12 1-4scaling       1.0
13
14 switching        on
15 switchdist       8
16 cutoff           12
17 pairlistdist     14
18 margin           0
19 stepspercycle    20
20
21 wrapWater        on
22 rigidBonds       water
23
24 timestep 1.0
25
26 PME              yes
27 PMEGridSpacing   1.0
28
29 outputenergies   100
30 outputtiming     100
31 binaryoutput     yes
32 outputname       CHT_PME_D2
33 dcdfreq          400
34 restartfreq      100000
35 restartname      rest_CHT_PME_D2
36
37 binvelocities    CHT_PME_D1.vel
38
39 langevin             on
40 langevinDamping     5
41 langevinTemp        300
42 langevinHydrogen    no
43
44 fixedAtoms       on
45 fixedAtomsFile   fix_cht_middle.pdb
46 fixedAtomsCol    O
47 extendedSystem       CHT_PME_D1.xsc
```

```
48
49 run                     10000000
```

A.4 Gromacs Inputs for Chapter 5

Listing A.8: step1.0-minimisation.mdp

```
1  define                  = -DPOSRES -DPOSRES_CHT
2  integrator              = steep
3  emtol                   = 500.0
4  emstep                  = 0.01
5  nsteps                  = 5000
6  nstlist                 = 1
7  cutoff-scheme           = Verlet
8  rlist                   = 1.2
9  vdwtype                 = Cut-off
10 vdw-modifier            = Force-switch
11 rvdw_switch             = 1.0
12 rvdw                    = 1.2
13 coulombtype             = PME
14 rcoulomb                = 1.2
15 constraints             = h-bonds
16 constraint_algorithm    = LINCS
17 lincs_iter              = 2
18 lincs_order             = 8
19 periodic-molecules      = yes
```

Listing A.9: step1.1-equilibration.mdp

```
1  define                  = -DPOSRES -DPOSRES_CHT
2  ;
3  integrator              = md
4  dt                      = 0.001
5  nsteps                  = 500000
6  ;
7  nstxtcout               = 500
8  nstvout                 = 5000
9  nstfout                 = 5000
10 nstcalcenergy           = 100
11 nstenergy               = 1000
12 nstlog                  = 1000
13 ;
14 cutoff-scheme           = Verlet
15 nstlist                 = 20
16 rlist                   = 1.2
17 vdwtype                 = Cut-off
18 vdw-modifier            = Force-switch
19 rvdw_switch             = 1.0
20 rvdw                    = 1.2
```

```
coulombtype              = PME
rcoulomb                 = 1.2
;
tcoupl                   = berendsen
tc_grps                  = NANO SOLV
tau_t                    = 0.1 0.1
ref_t                    = 300 300
;
; Pressure coupling is on
;pcoupl                   = Berendsen
; Pressure coupling on in NPT -
; berendesen only for intinial pressure coupling
pcoupl                   = Parrinello-Rahman
pcoupltype               = anisotropic
; semiisotropic to avoid vacuum bubble
;formation (with slab/membrane)
tau_p                    = 2.0 ;time constant, in ps
ref_p                    = 1.0 1.0 1.0 0 0 0
compressibility          = 2.5E-6 2.5E-6 4.5e-5 0 0 0  of water,
   bar^-1
refcoord_scaling         = com
;
continuation             = no
constraints              = h-bonds
constraint_algorithm     = LINCS
lincs_iter               = 2
lincs_order              = 8
;
nstcomm                  = 100
comm_mode                = linear
comm_grps                = NANO SOLV
;
gen-vel                  = yes
gen-temp                 = 300
gen-seed                 = -1
;
pbc              = xyz
periodic-molecules       = yes
```

Listing A.10: step2-production.mdp

```
integrator               = md
dt                       = 0.002
nsteps                   = 50000000
nstxtcout                = 5000
nstvout                  = 50000
nstfout                  = 50000
nstcalcenergy            = 100
nstenergy                = 1000
nstlog                   = 1000
;
cutoff-scheme            = Verlet
nstlist                  = 20
```

```
vdwtype                 = Cut-off
vdw-modifier            = Force-switch
rvdw_switch             = 1.0
rvdw                    = 1.2
rcoulomb                = 1.2
rlist                   = 1.2
coulombtype             = PME
;
tcoupl                  = Nose-Hoover
tc_grps                 = NANO SOLV
tau_t                   = 1.0 1.0
ref_t                   = 300 300
;
pcoupl                  = Parrinello-Rahman
pcoupltype              = anisotropic
tau_p                   = 2.0
compressibility         = 2.5E-6 2.5E-6 4.5e-5 0.0 0.0 0.0
ref_p                   = 1.0 1.0 1.0 0 0 0
;
constraints             = h-bonds
constraint_algorithm    = LINCS
continuation            = yes
;
nstcomm                 = 100
comm_mode               = linear
comm_grps               = NANO SOLV
;
periodic-molecules      = yes
```

A.5 NAMD Inputs for Chapter 6

Listing A.11: step6.1-equilibration.inp

```
structure               step5_input.psf
coordinates             step5_input.pdb

set temp                303.15;
set outputname          step6.1_equilibration;

# read system values written by CHARMM
#(need to convert uppercases to lowercases)
exec tr "\[:upper:\]" "\[:lower:\]"  \
< ../step5_assembly.str | sed -e "s/ =//g" > step5_input.str
source                  step5_input.str

temperature             $temp;

outputName              $outputname;

firsttimestep           0;
```

```
restartfreq             1000;
dcdfreq                 5000;
dcdUnitCell             yes;
xstFreq                 5000;
outputEnergies          125;
outputTiming            1000;

# Force-Field Parameters
paraTypeCharmm          on;
parameters  toppar/par_all36m_prot.prm
parameters  toppar/par_all36_na.prm
parameters  toppar/par_all36_carb.prm
parameters  toppar/par_all36_lipid.prm
parameters  toppar/par_all36_cgenff.prm
parameters  toppar/par_interface.prm
parameters  toppar/toppar_all36_moreions.str
parameters  toppar/toppar_all36_nano_lig.str
parameters  toppar/toppar_all36_nano_lig_patch.str
parameters  toppar/toppar_all36_synthetic_polymer.str
parameters  toppar/toppar_all36_synthetic_polymer_patch.str
parameters  toppar/toppar_all36_polymer_solvent.str
parameters  toppar/toppar_water_ions.str
parameters  toppar/toppar_dum_noble_gases.str
parameters  toppar/toppar_ions_won.str
parameters  toppar/cam.str
parameters  toppar/toppar_all36_prot_arg0.str
parameters  toppar/toppar_all36_prot_c36m_d_aminoacids.str
parameters  toppar/toppar_all36_prot_fluoro_alkanes.str
parameters  toppar/toppar_all36_prot_heme.str
parameters  toppar/toppar_all36_prot_na_combined.str
parameters  toppar/toppar_all36_prot_retinol.str
parameters  toppar/toppar_all36_prot_model.str
parameters  toppar/toppar_all36_prot_modify_res.str
parameters  toppar/toppar_all36_na_nad_ppi.str
parameters  toppar/toppar_all36_na_rna_modified.str
parameters  toppar/toppar_all36_lipid_sphingo.str
parameters  toppar/toppar_all36_lipid_archaeal.str
parameters  toppar/toppar_all36_lipid_bacterial.str
parameters  toppar/toppar_all36_lipid_cardiolipin.str
parameters  toppar/toppar_all36_lipid_cholesterol.str
parameters  toppar/toppar_all36_lipid_dag.str
parameters  toppar/toppar_all36_lipid_inositol.str
parameters  toppar/toppar_all36_lipid_lnp.str
parameters  toppar/toppar_all36_lipid_lps.str
parameters  toppar/toppar_all36_lipid_mycobacterial.str
parameters  toppar/toppar_all36_lipid_miscellaneous.str
parameters  toppar/toppar_all36_lipid_model.str
parameters  toppar/toppar_all36_lipid_prot.str
parameters  toppar/toppar_all36_lipid_tag.str
parameters  toppar/toppar_all36_lipid_yeast.str
parameters  toppar/toppar_all36_lipid_hmmm.str
parameters  toppar/toppar_all36_lipid_detergent.str
parameters  toppar/toppar_all36_lipid_ether.str
parameters  toppar/toppar_all36_lipid_oxidized.str
```

```
parameters  toppar/toppar_all36_carb_glycolipid.str
parameters  toppar/toppar_all36_carb_glycopeptide.str
parameters  toppar/toppar_all36_carb_imlab.str
parameters  toppar/toppar_all36_label_spin.str
parameters  toppar/toppar_all36_label_fluorophore.str

# Nonbonded Parameters
exclude                 scaled1-4
1-4scaling              1.0
switching               on
vdwForceSwitching       on;
cutoff                  12.0;
switchdist              10.0;
pairlistdist            16.0;
stepspercycle           20;
pairlistsPerCycle       2;

# Integrator Parameters
timestep                1.0;
rigidBonds              all;
nonbondedFreq           1;
fullElectFrequency      1;

# Constant Temperature Control ONLY DURING EQUILB
reassignFreq            500;
reassignTemp            $temp;

cellBasisVector1     $a   0.0   0.0;
cellBasisVector2     $d    $b   0.0;
cellBasisVector3    0.0   0.0    $c;
cellOrigin          0.0   0.0 $zcen;

wrapWater               on;
wrapAll                 on;
wrapNearest             off;

PME                     yes;
PMEInterpOrder          6;
PMEGridSpacing          1.0;

# Pressure and volume control
useGroupPressure        yes;
useFlexibleCell         yes;
useConstantRatio        yes;

langevin                on
langevinDamping         1.0
langevinTemp            $temp
langevinHydrogen        off

# planar restraint
exec sed -e "s/Constant \$fc/Constant 5/g" \
step5_input.colvar.str > restraints/$outputname.col
colvars                 on
```

```
colvarsConfig           restraints/$outputname.col

# dihedral restraint
exec sed -e "s/\$FC/500/g" restraints/dihe.txt > \
restraints/$outputname.dihe
extraBonds              yes
extraBondsFile          restraints/$outputname.dihe

minimize                10000
numsteps                90000000
run                     125000
```

Listing A.12: step6.2-equilibration.inp

```
structure               step5_input.psf
coordinates             step5_input.pdb

set temp                303.15;
set outputname          step6.2_equilibration;

source                  step5_input.str
set inputname           step6.1_equilibration;
outputname              $outputname;
binCoordinates          $inputname.coor;
binVelocities           $inputname.vel;
extendedSystem          $inputname.xsc;

firsttimestep           135000;
restartfreq             1000;
dcdfreq                 5000;
dcdUnitCell             yes;
xstFreq                 5000;
outputEnergies          125;
outputTiming            1000;
# Force-Field Parameters
paraTypeCharmm          on;
parameters  toppar/par_all36m_prot.prm
parameters  toppar/par_all36_na.prm
parameters  toppar/par_all36_carb.prm
parameters  toppar/par_all36_lipid.prm
parameters  toppar/par_all36_cgenff.prm
parameters  toppar/par_interface.prm
parameters  toppar/toppar_all36_moreions.str
parameters  toppar/toppar_all36_nano_lig.str
parameters  toppar/toppar_all36_nano_lig_patch.str
parameters  toppar/toppar_all36_synthetic_polymer.str
parameters  toppar/toppar_all36_synthetic_polymer_patch.str
parameters  toppar/toppar_all36_polymer_solvent.str
parameters  toppar/toppar_water_ions.str
parameters  toppar/toppar_dum_noble_gases.str
parameters  toppar/toppar_ions_won.str
parameters  toppar/cam.str
parameters  toppar/toppar_all36_prot_arg0.str
```

```
parameters  toppar/toppar_all36_prot_c36m_d_aminoacids.str
parameters  toppar/toppar_all36_prot_fluoro_alkanes.str
parameters  toppar/toppar_all36_prot_heme.str
parameters  toppar/toppar_all36_prot_na_combined.str
parameters  toppar/toppar_all36_prot_retinol.str
parameters  toppar/toppar_all36_prot_model.str
parameters  toppar/toppar_all36_prot_modify_res.str
parameters  toppar/toppar_all36_na_nad_ppi.str
parameters  toppar/toppar_all36_na_rna_modified.str
parameters  toppar/toppar_all36_lipid_sphingo.str
parameters  toppar/toppar_all36_lipid_archaeal.str
parameters  toppar/toppar_all36_lipid_bacterial.str
parameters  toppar/toppar_all36_lipid_cardiolipin.str
parameters  toppar/toppar_all36_lipid_cholesterol.str
parameters  toppar/toppar_all36_lipid_dag.str
parameters  toppar/toppar_all36_lipid_inositol.str
parameters  toppar/toppar_all36_lipid_lnp.str
parameters  toppar/toppar_all36_lipid_lps.str
parameters  toppar/toppar_all36_lipid_mycobacterial.str
parameters  toppar/toppar_all36_lipid_miscellaneous.str
parameters  toppar/toppar_all36_lipid_model.str
parameters  toppar/toppar_all36_lipid_prot.str
parameters  toppar/toppar_all36_lipid_tag.str
parameters  toppar/toppar_all36_lipid_yeast.str
parameters  toppar/toppar_all36_lipid_hmmm.str
parameters  toppar/toppar_all36_lipid_detergent.str
parameters  toppar/toppar_all36_lipid_ether.str
parameters  toppar/toppar_all36_lipid_oxidized.str
parameters  toppar/toppar_all36_carb_glycolipid.str
parameters  toppar/toppar_all36_carb_glycopeptide.str
parameters  toppar/toppar_all36_carb_imlab.str
parameters  toppar/toppar_all36_label_spin.str
parameters  toppar/toppar_all36_label_fluorophore.str

# Nonbonded Parameters
exclude                 scaled1-4
1-4scaling              1.0
switching               on
vdwForceSwitching       on;
cutoff                  12.0;
switchdist              10.0;
pairlistdist            16.0;
stepspercycle           20;
pairlistsPerCycle       2;

# Integrator Parameters
timestep                1.0;
rigidBonds              all;
nonbondedFreq           1;
fullElectFrequency      1;

# Constant Temperature Control ONLY DURING EQUILB
reassignFreq            500;
reassignTemp            $temp;
```

```

if { $boxtype == "hexa" } {
   set wrapnearst on
} else {
   set wrapnearst off
}

wrapWater               on;
wrapAll                 on;
wrapNearest             $wrapnearst;

# PME (for full-system periodic electrostatics)
PME                     yes;
PMEInterpOrder          6;
PMEGridSpacing          1.0;

# Pressure and volume control
useGroupPressure        yes;
useFlexibleCell         yes;
useConstantRatio        yes;

langevin                on
langevinDamping         1.0
langevinTemp            $temp
langevinHydrogen        off

# planar restraint
exec sed -e "s/Constant \$fc/Constant 5/g" \
step5_input.colvar.str > restraints/$outputname.col
colvars                 on
colvarsConfig           restraints/$outputname.col

# dihedral restraint
exec sed -e "s/\$FC/200/g" restraints/dihe.txt > \
restraints/$outputname.dihe
extraBonds              yes
extraBondsFile          restraints/$outputname.dihe

numsteps                90000000
run                     125000
```

Listing A.13: step6.3-equilibration.inp

```
structure               step5_input.psf
coordinates             step5_input.pdb

set temp                303.15;
set outputname          step6.3_equilibration;

source                  step5_input.str
set inputname           step6.2_equilibration;
outputname              $outputname;
binCoordinates          $inputname.coor;
```

```
binVelocities           $inputname.vel;
extendedSystem          $inputname.xsc;

firsttimestep           260000;
restartfreq             1000;
dcdfreq                 5000;
dcdUnitCell             yes;
xstFreq                 5000;
outputEnergies          125;
outputTiming            1000;

# Force-Field Parameters
paraTypeCharmm          on;
parameters  toppar/par_all36m_prot.prm
parameters  toppar/par_all36_na.prm
parameters  toppar/par_all36_carb.prm
parameters  toppar/par_all36_lipid.prm
parameters  toppar/par_all36_cgenff.prm
parameters  toppar/par_interface.prm
parameters  toppar/toppar_all36_moreions.str
parameters  toppar/toppar_all36_nano_lig.str
parameters  toppar/toppar_all36_nano_lig_patch.str
parameters  toppar/toppar_all36_synthetic_polymer.str
parameters  toppar/toppar_all36_synthetic_polymer_patch.str
parameters  toppar/toppar_all36_polymer_solvent.str
parameters  toppar/toppar_water_ions.str
parameters  toppar/toppar_dum_noble_gases.str
parameters  toppar/toppar_ions_won.str
parameters  toppar/cam.str
parameters  toppar/toppar_all36_prot_arg0.str
parameters  toppar/toppar_all36_prot_c36m_d_aminoacids.str
parameters  toppar/toppar_all36_prot_fluoro_alkanes.str
parameters  toppar/toppar_all36_prot_heme.str
parameters  toppar/toppar_all36_prot_na_combined.str
parameters  toppar/toppar_all36_prot_retinol.str
parameters  toppar/toppar_all36_prot_model.str
parameters  toppar/toppar_all36_prot_modify_res.str
parameters  toppar/toppar_all36_na_nad_ppi.str
parameters  toppar/toppar_all36_na_rna_modified.str
parameters  toppar/toppar_all36_lipid_sphingo.str
parameters  toppar/toppar_all36_lipid_archaeal.str
parameters  toppar/toppar_all36_lipid_bacterial.str
parameters  toppar/toppar_all36_lipid_cardiolipin.str
parameters  toppar/toppar_all36_lipid_cholesterol.str
parameters  toppar/toppar_all36_lipid_dag.str
parameters  toppar/toppar_all36_lipid_inositol.str
parameters  toppar/toppar_all36_lipid_lnp.str
parameters  toppar/toppar_all36_lipid_lps.str
parameters  toppar/toppar_all36_lipid_mycobacterial.str
parameters  toppar/toppar_all36_lipid_miscellaneous.str
parameters  toppar/toppar_all36_lipid_model.str
parameters  toppar/toppar_all36_lipid_prot.str
parameters  toppar/toppar_all36_lipid_tag.str
parameters  toppar/toppar_all36_lipid_yeast.str
```

```
parameters  toppar/toppar_all36_lipid_hmmm.str
parameters  toppar/toppar_all36_lipid_detergent.str
parameters  toppar/toppar_all36_lipid_ether.str
parameters  toppar/toppar_all36_lipid_oxidized.str
parameters  toppar/toppar_all36_carb_glycolipid.str
parameters  toppar/toppar_all36_carb_glycopeptide.str
parameters  toppar/toppar_all36_carb_imlab.str
parameters  toppar/toppar_all36_label_spin.str
parameters  toppar/toppar_all36_label_fluorophore.str

# Nonbonded Parameters
exclude                 scaled1-4
1-4scaling              1.0
switching               on
vdwForceSwitching       on;
cutoff                  12.0;
switchdist              10.0;
pairlistdist            16.0;
stepspercycle           20;
pairlistsPerCycle       2;

timestep                1.0;
rigidBonds              all;
nonbondedFreq           1;
fullElectFrequency      1;

# Constant Temperature Control ONLY DURING EQUILB
reassignFreq            500;
reassignTemp            $temp;

if { $boxtype == "hexa" } {
   set wrapnearst on
} else {
   set wrapnearst off
}

wrapWater               on;
wrapAll                 on;
wrapNearest             $wrapnearst;

# PME (for full-system periodic electrostatics)
PME                     yes;
PMEInterpOrder          6;
PMEGridSpacing          1.0;

# Pressure and volume control
useGroupPressure        yes;
useFlexibleCell         yes;
useConstantRatio        yes;

langevin                on
langevinDamping         1.0
langevinTemp            $temp
langevinHydrogen        off
```

```

# constant pressure
langevinPiston          on
langevinPistonTarget    1.01325
langevinPistonPeriod    50.0
langevinPistonDecay     25.0
langevinPistonTemp      $temp

# planar restraint
exec sed -e "s/Constant \$fc/Constant 2/g" \
step5_input.colvar.str > restraints/$outputname.col
colvars                 on
colvarsConfig           restraints/$outputname.col

# dihedral restraint
exec sed -e "s/\$FC/100/g" restraints/dihe.txt \
> restraints/$outputname.dihe
extraBonds              yes
extraBondsFile          restraints/$outputname.dihe

numsteps                90000000
run                     125000
```

Listing A.14: step6.4-equilibration.inp

```
structure               step5_input.psf
coordinates             step5_input.pdb

set temp                303.15;
set outputname          step6.4_equilibration;

source                  step5_input.str
set inputname           step6.3_equilibration;
outputname              $outputname;
binCoordinates          $inputname.coor;
binVelocities           $inputname.vel;
extendedSystem          $inputname.xsc;

firsttimestep           385000;
restartfreq             1000;
dcdfreq                 5000;
dcdUnitCell             yes;
xstFreq                 5000;
outputEnergies          125;
outputTiming            1000;
# Force-Field Parameters
paraTypeCharmm          on;
parameters  toppar/par_all36m_prot.prm
parameters  toppar/par_all36_na.prm
parameters  toppar/par_all36_carb.prm
parameters  toppar/par_all36_lipid.prm
parameters  toppar/par_all36_cgenff.prm
parameters  toppar/par_interface.prm
```

```
parameters  toppar/toppar_all36_moreions.str
parameters  toppar/toppar_all36_nano_lig.str
parameters  toppar/toppar_all36_nano_lig_patch.str
parameters  toppar/toppar_all36_synthetic_polymer.str
parameters  toppar/toppar_all36_synthetic_polymer_patch.str
parameters  toppar/toppar_all36_polymer_solvent.str
parameters  toppar/toppar_water_ions.str
parameters  toppar/toppar_dum_noble_gases.str
parameters  toppar/toppar_ions_won.str
parameters  toppar/cam.str
parameters  toppar/toppar_all36_prot_arg0.str
parameters  toppar/toppar_all36_prot_c36m_d_aminoacids.str
parameters  toppar/toppar_all36_prot_fluoro_alkanes.str
parameters  toppar/toppar_all36_prot_heme.str
parameters  toppar/toppar_all36_prot_na_combined.str
parameters  toppar/toppar_all36_prot_retinol.str
parameters  toppar/toppar_all36_prot_model.str
parameters  toppar/toppar_all36_prot_modify_res.str
parameters  toppar/toppar_all36_na_nad_ppi.str
parameters  toppar/toppar_all36_na_rna_modified.str
parameters  toppar/toppar_all36_lipid_sphingo.str
parameters  toppar/toppar_all36_lipid_archaeal.str
parameters  toppar/toppar_all36_lipid_bacterial.str
parameters  toppar/toppar_all36_lipid_cardiolipin.str
parameters  toppar/toppar_all36_lipid_cholesterol.str
parameters  toppar/toppar_all36_lipid_dag.str
parameters  toppar/toppar_all36_lipid_inositol.str
parameters  toppar/toppar_all36_lipid_lnp.str
parameters  toppar/toppar_all36_lipid_lps.str
parameters  toppar/toppar_all36_lipid_mycobacterial.str
parameters  toppar/toppar_all36_lipid_miscellaneous.str
parameters  toppar/toppar_all36_lipid_model.str
parameters  toppar/toppar_all36_lipid_prot.str
parameters  toppar/toppar_all36_lipid_tag.str
parameters  toppar/toppar_all36_lipid_yeast.str
parameters  toppar/toppar_all36_lipid_hmmm.str
parameters  toppar/toppar_all36_lipid_detergent.str
parameters  toppar/toppar_all36_lipid_ether.str
parameters  toppar/toppar_all36_lipid_oxidized.str
parameters  toppar/toppar_all36_carb_glycolipid.str
parameters  toppar/toppar_all36_carb_glycopeptide.str
parameters  toppar/toppar_all36_carb_imlab.str
parameters  toppar/toppar_all36_label_spin.str
parameters  toppar/toppar_all36_label_fluorophore.str

# Nonbonded Parameters
exclude                 scaled1-4
1-4scaling              1.0
switching               on
vdwForceSwitching       on;

cutoff                  12.0;
switchdist              10.0;
pairlistdist            16.0;
```

```
stepspercycle           20;
pairlistsPerCycle       2;

# Integrator Parameters
timestep                2.0;
rigidBonds              all;
nonbondedFreq           1;
fullElectFrequency      1;

# Constant Temperature Control ONLY DURING EQUILB
reassignFreq            500;
reassignTemp            $temp;

if { $boxtype == "hexa" } {
   set wrapnearst on
} else {
   set wrapnearst off
}

wrapWater               on;
wrapAll                 on;
wrapNearest             $wrapnearst;

# PME (for full-system periodic electrostatics)
PME                     yes;
PMEInterpOrder          6;
PMEGridSpacing          1.0;

# Pressure and volume control
useGroupPressure        yes;
useFlexibleCell         yes;
useConstantRatio        yes;

langevin                on
langevinDamping         1.0
langevinTemp            $temp
langevinHydrogen        off

# constant pressure
langevinPiston          on
langevinPistonTarget    1.01325
langevinPistonPeriod    50.0
langevinPistonDecay     25.0
langevinPistonTemp      $temp

# planar restraint
exec sed -e "s/Constant \$fc/Constant 1/g"
\ step5_input.colvar.str > restraints/$outputname.col
colvars                 on
colvarsConfig           restraints/$outputname.col

# dihedral restraint
exec sed -e "s/\$FC/100/g" restraints/dihe.txt \
> restraints/$outputname.dihe
```

```
extraBonds              yes
extraBondsFile          restraints/$outputname.dihe

numsteps                90000000
run                     250000
```

Listing A.15: step6.5-equilibration.inp

```
structure               step5_input.psf
coordinates             step5_input.pdb

set temp                303.15;
set outputname          step6.5_equilibration;

source                  step5_input.str
set inputname           step6.4_equilibration;
outputname              $outputname;
binCoordinates          $inputname.coor;
binVelocities           $inputname.vel;
extendedSystem          $inputname.xsc;

firsttimestep           635000;
restartfreq             1000;
dcdfreq                 5000;
dcdUnitCell             yes;
xstFreq                 5000;
outputEnergies          125;
outputTiming            1000;
# Force-Field Parameters
paraTypeCharmm          on;
parameters  toppar/par_all36m_prot.prm
parameters  toppar/par_all36_na.prm
parameters  toppar/par_all36_carb.prm
parameters  toppar/par_all36_lipid.prm
parameters  toppar/par_all36_cgenff.prm
parameters  toppar/par_interface.prm
parameters  toppar/toppar_all36_moreions.str
parameters  toppar/toppar_all36_nano_lig.str
parameters  toppar/toppar_all36_nano_lig_patch.str
parameters  toppar/toppar_all36_synthetic_polymer.str
parameters  toppar/toppar_all36_synthetic_polymer_patch.str
parameters  toppar/toppar_all36_polymer_solvent.str
parameters  toppar/toppar_water_ions.str
parameters  toppar/toppar_dum_noble_gases.str
parameters  toppar/toppar_ions_won.str
parameters  toppar/cam.str
parameters  toppar/toppar_all36_prot_arg0.str
parameters  toppar/toppar_all36_prot_c36m_d_aminoacids.str
parameters  toppar/toppar_all36_prot_fluoro_alkanes.str
parameters  toppar/toppar_all36_prot_heme.str
parameters  toppar/toppar_all36_prot_na_combined.str
parameters  toppar/toppar_all36_prot_retinol.str
parameters  toppar/toppar_all36_prot_model.str
```

```
parameters  toppar/toppar_all36_prot_modify_res.str
parameters  toppar/toppar_all36_na_nad_ppi.str
parameters  toppar/toppar_all36_na_rna_modified.str
parameters  toppar/toppar_all36_lipid_sphingo.str
parameters  toppar/toppar_all36_lipid_archaeal.str
parameters  toppar/toppar_all36_lipid_bacterial.str
parameters  toppar/toppar_all36_lipid_cardiolipin.str
parameters  toppar/toppar_all36_lipid_cholesterol.str
parameters  toppar/toppar_all36_lipid_dag.str
parameters  toppar/toppar_all36_lipid_inositol.str
parameters  toppar/toppar_all36_lipid_lnp.str
parameters  toppar/toppar_all36_lipid_lps.str
parameters  toppar/toppar_all36_lipid_mycobacterial.str
parameters  toppar/toppar_all36_lipid_miscellaneous.str
parameters  toppar/toppar_all36_lipid_model.str
parameters  toppar/toppar_all36_lipid_prot.str
parameters  toppar/toppar_all36_lipid_tag.str
parameters  toppar/toppar_all36_lipid_yeast.str
parameters  toppar/toppar_all36_lipid_hmmm.str
parameters  toppar/toppar_all36_lipid_detergent.str
parameters  toppar/toppar_all36_lipid_ether.str
parameters  toppar/toppar_all36_lipid_oxidized.str
parameters  toppar/toppar_all36_carb_glycolipid.str
parameters  toppar/toppar_all36_carb_glycopeptide.str
parameters  toppar/toppar_all36_carb_imlab.str
parameters  toppar/toppar_all36_label_spin.str
parameters  toppar/toppar_all36_label_fluorophore.str
# Nonbonded Parameters
exclude                 scaled1-4
1-4scaling              1.0
switching               on
vdwForceSwitching       on;
# You have some freedom choosing the cutoff
cutoff                  12.0;
switchdist              10.0;
pairlistdist            16.0;
stepspercycle           20;
pairlistsPerCycle       2;

# Integrator Parameters
timestep                2.0;
rigidBonds              all;
nonbondedFreq           1;
fullElectFrequency      1;

# Constant Temperature Control ONLY DURING EQUILB
reassignFreq            500;
reassignTemp            $temp;

if { $boxtype == "hexa" } {
   set wrapnearst on
} else {
   set wrapnearst off
}
```

```
100
101 wrapWater                on;
102 wrapAll                  on;
103 wrapNearest              $wrapnearst;
104
105 # PME (for full-system periodic electrostatics)
106 PME                      yes;
107 PMEInterpOrder           6;
108 PMEGridSpacing           1.0;
109
110 # Pressure and volume control
111 useGroupPressure         yes;
112 useFlexibleCell          yes;
113 useConstantRatio         yes;
114
115 langevin                 on
116 langevinDamping          1.0
117 langevinTemp             $temp
118 langevinHydrogen         off
119
120 # constant pressure
121 langevinPiston           on
122 langevinPistonTarget     1.01325
123 langevinPistonPeriod     50.0
124 langevinPistonDecay      25.0
125 langevinPistonTemp       $temp
126
127 # planar restraint
128 exec sed -e "s/Constant \$fc/Constant 0.2/g" \
129 step5_input.colvar.str > restraints/$outputname.col
130 colvars                  on
131 colvarsConfig            restraints/$outputname.col
132
133 # dihedral restraint
134 exec sed -e "s/\$FC/50/g" restraints/dihe.txt >\
135 restraints/$outputname.dihe
136 extraBonds               yes
137 extraBondsFile           restraints/$outputname.dihe
138
139 numsteps                 90000000
140 run                      250000
```

Listing A.16: step6.6-equilibration.inp

```
1 structure                 step5_input.psf
2 coordinates               step5_input.pdb
3
4 set temp                  303.15;
5 set outputname            step6.6_equilibration;
6
7 source                    step5_input.str
8 set inputname             step6.5_equilibration;
9 outputname                $outputname;
```

```
binCoordinates          $inputname.coor;
binVelocities           $inputname.vel;
extendedSystem          $inputname.xsc;

firsttimestep           885000;
restartfreq             1000;
dcdfreq                 5000;
dcdUnitCell             yes;
xstFreq                 5000;
outputEnergies          125;
outputTiming            1000;
# Force-Field Parameters
paraTypeCharmm          on;
parameters  toppar/par_all36m_prot.prm
parameters  toppar/par_all36_na.prm
parameters  toppar/par_all36_carb.prm
parameters  toppar/par_all36_lipid.prm
parameters  toppar/par_all36_cgenff.prm
parameters  toppar/par_interface.prm
parameters  toppar/toppar_all36_moreions.str
parameters  toppar/toppar_all36_nano_lig.str
parameters  toppar/toppar_all36_nano_lig_patch.str
parameters  toppar/toppar_all36_synthetic_polymer.str
parameters  toppar/toppar_all36_synthetic_polymer_patch.str
parameters  toppar/toppar_all36_polymer_solvent.str
parameters  toppar/toppar_water_ions.str
parameters  toppar/toppar_dum_noble_gases.str
parameters  toppar/toppar_ions_won.str
parameters  toppar/cam.str
parameters  toppar/toppar_all36_prot_arg0.str
parameters  toppar/toppar_all36_prot_c36m_d_aminoacids.str
parameters  toppar/toppar_all36_prot_fluoro_alkanes.str
parameters  toppar/toppar_all36_prot_heme.str
parameters  toppar/toppar_all36_prot_na_combined.str
parameters  toppar/toppar_all36_prot_retinol.str
parameters  toppar/toppar_all36_prot_model.str
parameters  toppar/toppar_all36_prot_modify_res.str
parameters  toppar/toppar_all36_na_nad_ppi.str
parameters  toppar/toppar_all36_na_rna_modified.str
parameters  toppar/toppar_all36_lipid_sphingo.str
parameters  toppar/toppar_all36_lipid_archaeal.str
parameters  toppar/toppar_all36_lipid_bacterial.str
parameters  toppar/toppar_all36_lipid_cardiolipin.str
parameters  toppar/toppar_all36_lipid_cholesterol.str
parameters  toppar/toppar_all36_lipid_dag.str
parameters  toppar/toppar_all36_lipid_inositol.str
parameters  toppar/toppar_all36_lipid_lnp.str
parameters  toppar/toppar_all36_lipid_lps.str
parameters  toppar/toppar_all36_lipid_mycobacterial.str
parameters  toppar/toppar_all36_lipid_miscellaneous.str
parameters  toppar/toppar_all36_lipid_model.str
parameters  toppar/toppar_all36_lipid_prot.str
parameters  toppar/toppar_all36_lipid_tag.str
parameters  toppar/toppar_all36_lipid_yeast.str
```

```
parameters  toppar/toppar_all36_lipid_hmmm.str
parameters  toppar/toppar_all36_lipid_detergent.str
parameters  toppar/toppar_all36_lipid_ether.str
parameters  toppar/toppar_all36_lipid_oxidized.str
parameters  toppar/toppar_all36_carb_glycolipid.str
parameters  toppar/toppar_all36_carb_glycopeptide.str
parameters  toppar/toppar_all36_carb_imlab.str
parameters  toppar/toppar_all36_label_spin.str
parameters  toppar/toppar_all36_label_fluorophore.str
# Nonbonded Parameters
exclude                 scaled1-4
1-4scaling              1.0
switching               on
vdwForceSwitching       on;
cutoff                  12.0;
switchdist              10.0;
pairlistdist            16.0;
stepspercycle           20;
pairlistsPerCycle       2;
# Integrator Parameters
timestep                2.0;
rigidBonds              all;
nonbondedFreq           1;
fullElectFrequency      1;

# Constant Temperature Control ONLY DURING EQUILB
reassignFreq            500;
reassignTemp            $temp;

if { $boxtype == "hexa" } {
   set wrapnearst on
} else {
   set wrapnearst off
}

wrapWater               on;
wrapAll                 on;
wrapNearest             $wrapnearst;

# PME (for full-system periodic electrostatics)
PME                     yes;
PMEInterpOrder          6;
PMEGridSpacing          1.0;
# Pressure and volume control
useGroupPressure        yes;
useFlexibleCell         yes;
useConstantRatio        yes;

langevin                on
langevinDamping         1.0
langevinTemp            $temp
langevinHydrogen        off

# constant pressure
```

```
langevinPiston          on
langevinPistonTarget    1.01325
langevinPistonPeriod    50.0
langevinPistonDecay     25.0
langevinPistonTemp      $temp

# planar restraint
exec sed -e "s/Constant \$fc/Constant 0/g" \
step5_input.colvar.str > restraints/$outputname.col
colvars                 on
colvarsConfig           restraints/$outputname.col

# dihedral restraint
exec sed -e "s/\$FC/0/g" restraints/dihe.txt\
> restraints/$outputname.dihe
extraBonds              yes
extraBondsFile          restraints/$outputname.dihe

numsteps                90000000
run                     250000
```

Listing A.17: step7.0-production.inp

```
structure               step5_input.psf
coordinates             step5_input.pdb

set temp                303.15;
outputName              step7_production;
set inputname           step6.6_equilibration;
binCoordinates          $inputname.coor;
binVelocities           $inputname.vel;
extendedSystem          $inputname.xsc;

dcdfreq                 5000;
dcdUnitCell             yes;
xstFreq                 5000;
outputEnergies          5000;
outputTiming            5000;
restartfreq             5000;

# Force-Field Parameters
paraTypeCharmm          on;
parameters  toppar/par_all36m_prot.prm
parameters  toppar/par_all36_na.prm
parameters  toppar/par_all36_carb.prm
parameters  toppar/par_all36_lipid.prm
parameters  toppar/par_all36_cgenff.prm
parameters  toppar/par_interface.prm
parameters  toppar/toppar_all36_moreions.str
parameters  toppar/toppar_all36_nano_lig.str
parameters  toppar/toppar_all36_nano_lig_patch.str
parameters  toppar/toppar_all36_synthetic_polymer.str
parameters  toppar/toppar_all36_synthetic_polymer_patch.str
```

```
parameters  toppar/toppar_all36_polymer_solvent.str
parameters  toppar/toppar_water_ions.str
parameters  toppar/toppar_dum_noble_gases.str
parameters  toppar/toppar_ions_won.str
parameters  toppar/cam.str
parameters  toppar/toppar_all36_prot_arg0.str
parameters  toppar/toppar_all36_prot_c36m_d_aminoacids.str
parameters  toppar/toppar_all36_prot_fluoro_alkanes.str
parameters  toppar/toppar_all36_prot_heme.str
parameters  toppar/toppar_all36_prot_na_combined.str
parameters  toppar/toppar_all36_prot_retinol.str
parameters  toppar/toppar_all36_prot_model.str
parameters  toppar/toppar_all36_prot_modify_res.str
parameters  toppar/toppar_all36_na_nad_ppi.str
parameters  toppar/toppar_all36_na_rna_modified.str
parameters  toppar/toppar_all36_lipid_sphingo.str
parameters  toppar/toppar_all36_lipid_archaeal.str
parameters  toppar/toppar_all36_lipid_bacterial.str
parameters  toppar/toppar_all36_lipid_cardiolipin.str
parameters  toppar/toppar_all36_lipid_cholesterol.str
parameters  toppar/toppar_all36_lipid_dag.str
parameters  toppar/toppar_all36_lipid_inositol.str
parameters  toppar/toppar_all36_lipid_lnp.str
parameters  toppar/toppar_all36_lipid_lps.str
parameters  toppar/toppar_all36_lipid_mycobacterial.str
parameters  toppar/toppar_all36_lipid_miscellaneous.str
parameters  toppar/toppar_all36_lipid_model.str
parameters  toppar/toppar_all36_lipid_prot.str
parameters  toppar/toppar_all36_lipid_tag.str
parameters  toppar/toppar_all36_lipid_yeast.str
parameters  toppar/toppar_all36_lipid_hmmm.str
parameters  toppar/toppar_all36_lipid_detergent.str
parameters  toppar/toppar_all36_lipid_ether.str
parameters  toppar/toppar_all36_lipid_oxidized.str
parameters  toppar/toppar_all36_carb_glycolipid.str
parameters  toppar/toppar_all36_carb_glycopeptide.str
parameters  toppar/toppar_all36_carb_imlab.str
parameters  toppar/toppar_all36_label_spin.str
parameters  toppar/toppar_all36_label_fluorophore.str
source      step5_input.str

# Nonbonded Parameters
exclude                 scaled1-4
1-4scaling              1.0
switching               on
vdwForceSwitching       on;
cutoff                  12.0;
switchdist              10.0;
pairlistdist            16.0;
stepspercycle           20;
pairlistsPerCycle       2;
# Integrator Parameters
timestep                2.0;
rigidBonds              all;
```

```
nonbondedFreq           1;
fullElectFrequency      1;

wrapWater               on;
wrapAll                 on;
if { $boxtype == "hexa" } {
wrapNearest             on;
} else {
wrapNearest             off;
}

# PME (for full-system periodic electrostatics)
PME                     yes;
PMEInterpOrder          6;
PMEGridSpacing          1.0;

# Constant Pressure Control (variable volume)
useGroupPressure        yes;
useFlexibleCell         yes;
useConstantRatio        yes;
langevinPiston          on;
langevinPistonTarget    1.01325;
langevinPistonPeriod    50.0;
langevinPistonDecay     25.0;
langevinPistonTemp      $temp;

# Constant Temperature Control
langevin                on;
langevinDamping         1.0;
langevinTemp            $temp;
langevinHydrogen        off;
# run
numsteps                50000000;
run                     50000000;
```

Appendix A